Characterization of III-V nanowires for photovoltaic devices using advanced electron microscopy techniques

Persson, Johan Mikael

Publication date:
2012

Document Version
Publisher's PDF, also known as Version of record

PhD-thesis

Characterization of III-V nanowires for photovoltaic devices using advanced electron microscopy techniques

Johan M. Persson

July 2012

Center for Electron Nanoscopy
Technical University of Denmark

Contents

Abstract

In this work, the crystal structure of epitaxially grown semiconductor nanowires has been analysed using electron microscopy and to some extent X-ray diffractometry. The goal of the EU project which this work was a part of was to build multi-junction solar cells with nanowires as the main building blocks. Higher efficiency solar cells today tend to need rare elements and be very costly. Using nanowires should reduce the amount of material used and also reduce the cost. The geometry of nanowires allow epitaxially grown materials with a greater level of lattice mismatch, without introducing large amounts of defects due to strain. This increases the selection of possible materials to build the photo diodes. However, the strain will not be lower in the region of the junction and can change material properties, such as the bandgap. The substrate the wires are grown on was used as back contact of the solar cells. The interface between this layer and each nanowire is of course also a very sensitive area of the device. In order to examine these two interfaces a sample preparation method was further developed and adapted these types of samples. With this sample preparation method it was also possible to examine the very same nanowire sample using both X-ray diffraction and transmission electron microscopy. The examined structures were probed for their relative tilt to the substrate.

Nanobeam electron diffraction was used in order to probe the local crystal structure of a nanowire, especially across the junction. The strain across the junction measured by the difference in crystal lattice distance extends over a larger volume than the gradual change in composition found for the same sample. Measurements of other nanowires showed a continuously changing tilt along the wires and a local distortion of the crystal structure at the junction.

This thesis also comments on some unusual properties and findings of the examined nanowires:

Some nanowires sported a droplet-like protrusion of the catalyst gold particle reaching into the solid center of the nanowire. This feature can be discussed in terms of nanowire growth process and might influence device performance.

Several samples of nanowires grown in the [1 1 1]-direction were found to host unusual twin-defects in the $(\bar{1}\,1\,1)$-plane. The advent of [1 1 1] rotational twins are common during the growth of nanowires in the zincblende structure, however, twins in the diagonal $[\bar{1}\,1\,1]$ direction are not. Energy dispersive X-ray spectroscopy showed that these defects influence the local composition of the wire.

A thick contamination layer on top of the InP substrate of a sample with GaP nanowires was discovered and reported. This clearly showed the necessity of proper sample analysis post growth and device preparation.

The results of this work hopefully contributes to the understanding of the properties and growth mechanics of the nanowires. The methods developed should help improve the nanowire and device manufacturing through better characterization steps and ultimately lead to more efficient solar cells.

Resume

Krystalstrukturen i epitaxielt fremstillede halvleder nanowires er analyseret med hjælp af elektronmikroskopi og røntgendiffraktion i denne afhandling. Det EU projekt som denne afhandling har været en del af har som mål at fremstille en multi-junction solcelle ved hjælp af disse nanowires. De mest effektive solceller som fremstilles i dag bruger sjældne grundstoffer og er meget dyre. Ved at basere solcellerne på nanowireteknologi kan mængden af materiale formindskes og omkostningerne dermed reduceres.

Den specielle geometri og lille størrelse som nanowirerne har, tillader større fleksibilitet i krystalstrukturen mellem de forskellige materialer som bruges i heterostrukturene. Dette bevirker at flere forskellige materialer kan anvendes når funktionelle enheder såsom fotodioder skal opbygges, da færre ødelæggende defekter introduceres i krystalstrukturen. Den deformation der fremkommer i grænsefladen mellem materialerne er dog stadig stor nok til at kunne ændre f.eks. det elektriske båndgab i materialet. Substratet som nanowirerne er groet på bliver brugt til at kontaktere solcellen. Grænsefladen mellem substratet og nanowirerne er selvsagt en meget følsom del af enheden. For at undersøge grænsefladerne er en prøvetilberedningsteknik blevet udviklet som gør det muligt at undersøge den selvsamme nanowire ved hjælp af både røntgendiffraktion og tranmissionselektronmikroskopi. Wirernes orientering i forhold til substratet er blevet undersøgt ved hjælp af denne metode.

Elektrondiffraktion ved brug af en meget lille elektronstråle er brugt for at undersøge den lokale struktur af en nanowire henover en grænseflade mellem to materialer. Deformationen, udtrykt ved ændringen af afstanden mellem krystalplanerne breder sig over et større område end den graduelle ændring i kompositionen. Målinger på andre wirer viser en kontinuerlig ændring af orienteringen langs wiren og en lokal skævvridning af krystalstrukturen ved grænsefladen.

Ydermere kommenteres der i afhandlingen på nogle usædvanlige egenskaber fundet på de studerede nanowirer:

I nogle nanowirer viser der sig dråbelignende fremspring af katalysator guldpartiklen som rækker ind i midten/kernen af nanowiren. Denne detalje diskuteres i forbindelse med væksten af nanowirerne og vil muligvis indvirke på virkningen af den funktionelle enhed. Adskillelige nanowirer som er groet i [1 1 1] retningen havde usædvanlige tvilling-defekter i $(\overline{1}\,1\,1)$ planerne. Tvillingeplaner i (1 1 1) planerne er almindelige i zincblende strukturen, men det er de diagonale defekter i $(\overline{1}\,1\,1)$ planerne ikke. EDX viste at disse defekter påvirker den lokale komposition af wirerne.

Et tykt kontamineringslag ovenpå InP substratet i prøven med GaP nanowirer blev fundet og viser tydeligt nødvendigheden af en gennemgående analyse efter vækst og komponentfremstilling.

Resultaterne præsenteret i denne afhandling kan forhåbentligt medvirke til forståelsen af nanowirernes egenskaber og vækstmekanismer. Metoderne, som er blevet udviklet burde hjælpe fremstillingen af nanowirer og nanowire baserede komponenter gennem bedre karakterisering og ultimativt til bedre solceller.

Acknowledgements

I would like to thank everyone who supported me through this project. My family and friends of course, and also all my colleagues and co-workers. A special thank you goes out to my supervisors during this time, Jakob B. Wagner and Rafal E. Dunin-Borkowski.

I would also like to thank the awesome people at the Institute of semiconductor and solid state physics at Johannes Kepler Universität, Linz, for working with me on the X-ray diffraction parts of this project, and to the amazing people at Solid state physics Lund University and Sol Voltaics AB who provided the samples. And to everyone else within the AMON-RA project who helped make this PhD what it was.

This work was carried out within the Center for Electron Nanoscopy at the Technical University of Denmark and granted through the European Commission 7^{th} Framework Programme project AMON-RA (Architecture Materials, and One-dimensional Nanowires for Photovoltaics - Research and Applications), contract number 214814.

Part I

Introduction

Chapter 1

AMON-RA

1.1 The AMON-RA project

This thesis is a summary of work done on sample preparation and characterization of semiconductor nanowires and solar cell devices. The PhD was performed at the Technical University of Denmark (DTU) within the AMON-RA[1] framework. AMON-RA is an EU funded consortium five universities and one company, spread out over northern Europe. The goal has been to construct a new type of multi-junction solar cell using nanowires as photovoltaic cells. By doing this less material can be used and higher efficiencies are expected. In nanowire structures it is also possible to combine semiconductor materials where the lattice mismatch otherwise would be too large, hence allowing for more freedom engineering the device.

The main collaboration partners within the scope of this PhD have been the University of Lund (Sweden), the Johannes Kepler University of Linz (Austria) and the Lund based company SOL Voltaics AB (Sweden).

1.2 The AMON-RA solar cell device

Throughout the project the design of the device developed. While the main idea still persist, parts of the design were changed on the way. For example the nanowires grew thicker over time as theoretical advances showed the optimal thickness to be closer to 180 nm [1]. The material combinations also changed as well as the device manufacturing procedure. Some of these changes have been due to feedback possible by the work presented in this thesis.

A schematic of the device as seen in the beginning of the project can be seen in figure 1.1. The AMON-RA framework will continue after this thesis is published and only an intermittent device will be presented here.

[1] Architecture Materials, and One-dimensional Nanowires for Photovoltaics - Research and Applications, contract number 214814 in the 7th Framework Programme.

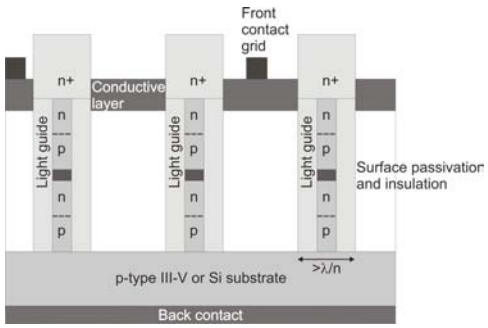

Figure 1.1: A schematic of the device as it was envisioned before the start of the project. It consist of several multi-junction nanowires with a translucent non-conductive layer in between.

Nevertheless the design presented in figure 1.2 come from a working "record device" measured at Fraunhofer institute ISI to 3.8 % efficiency (not yet published). The very same device was also characterized using TEM during the course of this work.

The device consist of several nanowires standing on the substrate they were grown on and with isolating material between them. The substrate is supposed to work as one contact and a thin gold layer on top is supposed to work as the other contact. As sunlight is shone on the sample the semiconductor junctions in the nanowires are going to work as photovoltaic cells and produce an electric current. Some background for this can be found in the section about photovoltaics, section 2.2. By combining several different junctions in the ideal case, and as envisioned in the beginning of the project, a larger part of the solar spectrum can be used. The result is a more efficient solar cell than for a single junction equivalent.

In between the nanowires there is an ITO (Indium Tin Oxide) layer that is transparent to most of the light emitted by the sun. This layer work as a light guide and at the same time as a conductor. The ITO and the nanowires are separated by a thin silicon oxide isolating layer.

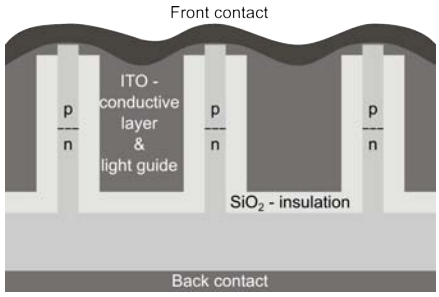

(a) Schematic of the new device structure.

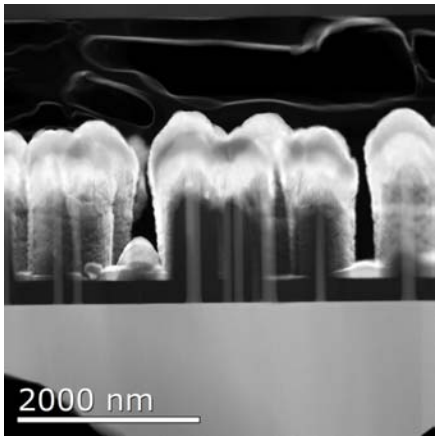

(b) STEM image of actual device

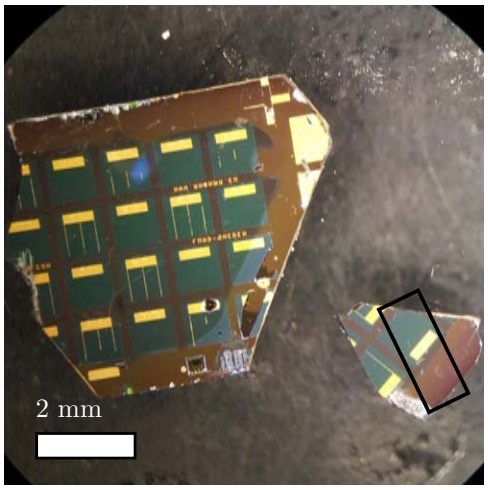

(c) Photography of the device from above.

Figure 1.2: (a) A schematic of the current record device withing the AMON-RA project. (b) A scanning transmission electron microscopy (STEM) image showing the true cross-section of this device. (c) A top view photograph of a working the same device. Each green square are ca 1×1 mm. The black rectangle denotes the area from which the cross-section above was acquired.

Chapter 2

Background

2.1 Motivation

No science can be done blind – there is always a need for evaluating the results of any experiment. This holds true especially when the end result is a working semiconductor device, or indeed any other human manufactured substance. As time have progressed and the subject matter have gotten to smaller sizes and demanding higher accuracy, the characterization process have gotten more complicated. Electron microscopy and X-ray diffractometry are two complementary methods for analysing these materials.

To use these techniques the samples have to be suitable with regards to the constrictions of the technique, both material wise and geometry wise. The typical sample for the X-ray diffractometer (XRD) would be a crystalline powder or a large single crystal. Analysing anything of a too small size would be hard with XRD, especially if what is interesting is a specific small area in a larger sample. Typical electron microscopy samples differ between types of microscopes. For the scanning electron microscope (SEM) the sample can either be a large piece of material where the morphology of the surface is important, or a flat polished sample if accurate chemical analysis is needed. For the transmission electron microscopes (TEM) the samples need to be very thin. Here a typical sample would be a ground powder or an extremely thinned down piece of a crystal.

To gain more information it is often important to prepare the samples in different ways. A large part of the work for this thesis have been in finding other ways to prepare different types of samples. In chapter 3 the methods that have been used are presented. Whilst the conclusions of this part of the thesis could have been: "sample preparation is hard!", several advances have been made that certainly will be useful for future characterization of nanostructured devices.

In one of the result chapters we talk about experiments trying to combine X-ray diffraction measurements with TEM measurements. As men-

tioned above the X-ray diffractometer is limited in its spatial resolution. Set-ups using standard X-ray sources typically have a size of it's probe in the order of millimeters. Even at a synchrotron facility with the state of the art equipment used in this work, the size of the beam is in the order of hundreds of nanometer [2]. At the same time the modern TEM have no problem analysing materials at a resolution one thousandth of that. The problem with TEM though, is the general inability to look at the bigger picture. Doing TEM of large areas is extremely time consuming [3]. To do ensemble measurements over larger areas and in the end get an average you certainly want to use XRD. Because of this, these methods are seen as complementary to each other.

Throughout this thesis there is a lot of talk about strain. Strain is a very important issue in the semiconductor industry [4], as it indeed is in the entire material science world [5]. If the layers of a semiconductor device is strained this will lead to a change in the electric conductivity and the so called band structure of those layers. This can be beneficial and can be introduced on purpose for example to change the band structure of a material [6], but unwanted strain can mean a non-working device. In chapter 6 the strain of some semiconductor nanowires are examined using electron microscopy techniques.

2.2 Photovoltaics

As pointed out by Nelson in her excellent primer on the subject [7], solar cells have gone through a massive evolution since the photovoltaic effect first was shown in the 1830s. In the beginning of the 20th century small inefficient Schottky barrier type cells were produced, but for other purposes than harvesting photons to produce electricity. In the 1950s the innovation of crystalline silicon p-n junctions made it possible to make photovoltaic cells with an efficiency of up to 6%, which meant that it started to be feasible to use the technique for light harvest. As interest for this energy source increased, especially with the oil crisis during the 70's, new and more efficient strategies were employed. During the 90's a second generation solar cells had come about with the goal of being cheaper, albeit with lower efficiency. Today efficiency are even higher and there are solar cells in a large price range. [7]

One of the ways of realizing higher efficiency and ultimately a lower price per watt ratio is by making so called multi-junction solar cells, which as pointed to in chapter 1 as one of the goals of the AMON-RA project. The highest efficiency of solar cells as reported by the 2011 Solar Cell Efficiency Tables [8] was by a multi-junction solar cell. It was a GaInP/GaInAs/Ge solar cell from AZUR showing an efficiency of 34.1%. This result should be compared with the best performing Si device, at 25.0% (UNSW PERL).

Another way of getting higher efficiency is to concentrate the sun light using optics. Since glass usually is both cheaper and exists in abundance, this is a much sought after solution. A disadvantage is for example that the sunlight always have to be focused at the cell, and hence either optics or the entire setup will have to move throughout the day. For concentrator cells the record is 43.5% for a GaInP/GaAs/GaInAs two-terminal device tested at NREL. For single cell Si at concentrated sunlight this number is 27.6%. [8]

In this perspective, the record device from AMON-RA that have been examined throughout the work on this thesis show a pretty meager result of 3.8% at concentrated sunlight. However – later iterations (not yet published results) show results several times higher.

2.2.1 Semiconductor theory

For a more thorough review of semiconductor theory, see [9, 10]. In a single atom the electrons can only exist in specific allowed energy levels – two electrons per level since the electrons also can have two different spin. These levels are traditionally called orbitals. Only the electrons in the outermost orbital are free to conduct a current in a material, the others need additional energy to get out of their orbit around the atom. The electrons in this outer orbital are called valence electrons.

If energy is added to the atom it might just happen that one of the electrons gain this energy and be excited from a lower energy level to a higher level. This energy can be delivered for example via an absorbed photon that aimed at the atom. Following the general rule in nature about energy minimization, the empty level in the electron should be filled. An electron from a higher energy level might therefore decrease it's energy by in turn sending out a photon with an energy corresponding to the difference between the levels. This can be utilized as a fingerprint of the particular atom and is used in Energy Dispersive X-ray spectroscopy (EDX) – a chemical analysis method explained in section 2.4. The exited electron can also be used to create a current, which is the principle behind photovoltaic cells.

When two atoms are placed close enough together they are able to share electrons. But since no more than two electrons can hold the exact same energy (with different spins) a splitting of the allowed energy levels occurs, figure 2.1(a). When many atoms are put together in this way the allowed energy levels form so called bands. The highest band having electrons is called the valence band, E_V. Above this is the conduction band, E_C, where electrons have the opportunity of moving freely, figure 2.1(b). The bandgap (E_g), is defined as the difference in energy between the conduction band and the valence band.

If the valence band and the conduction band overlap and the bandgap is zero the material is a metal, see figure 2.2. In metals electrons can move more or less freely all the time. If bandgap is non-zero, the electrons have to

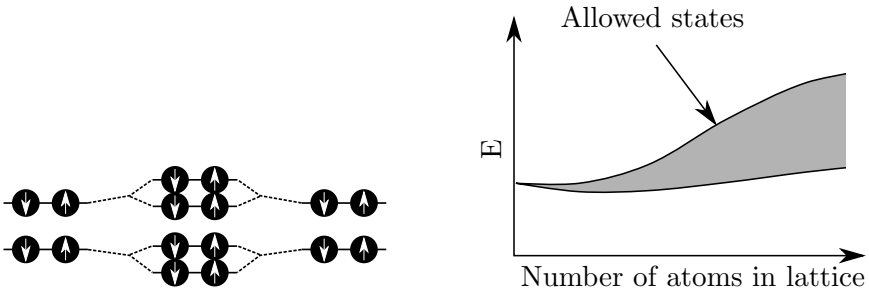

(a) Splitting of degenerate energy levels for two atoms.

(b) Splitting of energy levels of n atoms into a band.

Figure 2.1: As atoms bond to eachother and organize into crystals, they start sharing electron states. As this happen the energy levels are split and eventually form continuous bands of allowed states.

gain energy in order to first transcend to the conduction band to be able to move around. Hence no current can pass through the material. For a very large bandgap the material is said to be an isolator but if it is somewhere in between it is called a semiconductor. Smaller amounts of extra energy, such as thermal energy or photons, are often enough to make the semiconductor conduct a current. Typical semiconductors include group IV elements such as Silicon and Germanium, binary III-V materials such as GaAs and InP examined in this thesis, and binary II-VI materials such as ZnO.

The difference between a semiconductor and an insulator is mostly artificial, since it only is a question about the amount of energy it takes to excite the electron. More real is the notion of direct versus indirect bandgaps. If the bandgap is indirect, as for Si and Ge, electrons that change band need a higher energy to do so, or alternatively change momentum at the same time as the change in energy. For a direct bandgap material such as InP and GaAs an electron can be directly excited using a photon and upon re-combining with a hole, a photon will be irradiated.

Bandgap energies and the crystal lattice distance for some of the most common semiconductors can be seen in figure 2.3. Silicon has a bandgap of 1.12 eV and in comparison SiO_2 – an often used insulator – has been calculated to have a bandgap of 8.4eV [11]

In semiconductor devices the material is often doped. The dopants will either have one more or one less electron in their valence shell, making the semiconductor deficient of electrons (p-doped) or having a surplus of electrons (n-doped). By doing this, additional "steps" are introduced in the gap between the two bands, and the Fermi level moves closer to these steps. If the material is n-doped the extra energy level is just below the conduction band energy and is called a donor. If it is p-doped the step is just above the valence band and is called an acceptor, see figure 2.4. As can be guessed by

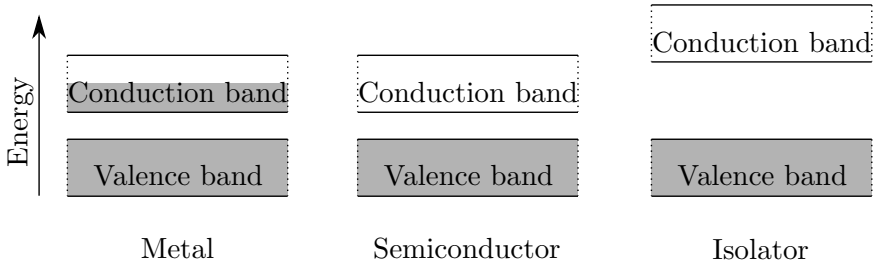

Figure 2.2: The top two bands that are crated from energy level splitting are called the valence and the conduction bands. Electrons can only flow as a current if they have free energy levels that they can move through. For a metal the valence electrons are in the conduction band, meaning that there are many free states for the electrons. For an isolator on the other hand there are no free states for the electrons. Only if these electrons gain enough energy to shift state from the valence band to the conduction band there will be a possibility for a current. A semiconductor is an isolator where the gap between the valence and the conduction bands is so small that almost the thermal energy at room temperature will facilitate a current.

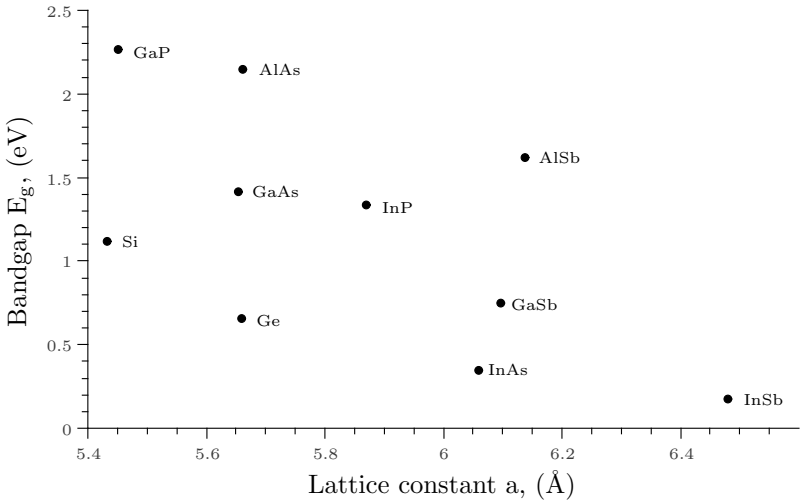

Figure 2.3: The bandgaps and the lattice distance for several of the more common semiconductors. Data from [12].

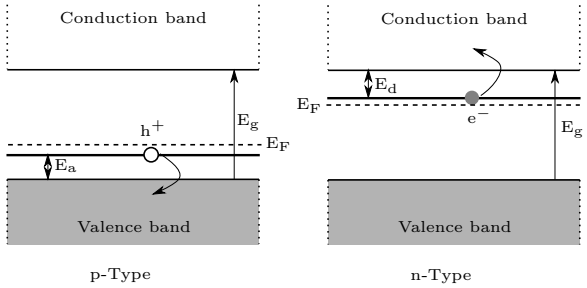

Figure 2.4: When semiconductors are doped with a material with more or fewer electrons in it's outer shell, there will be lone electrons or holes in the crystal. The additional energy levels of these electrons are in between the valence and the conduction band and hence they are easy to excite/make recombine.

the names, a donor level will donate an electron to the material. By exciting the electron from the donor-level to the conduction band a current can start flowing. In a parallel fashion the acceptor level can accept an electron into it, leaving a hole in the valence band by which a current also can flow. The Fermi-level (E_F) is the energy at which the probability of occupation by an electron is 0.5. For a non-doped (intrinsic) material this will be very close to the middle of the bandgap. For a doped material the Fermi level moves closer to the acceptor/donor level.

By combining different materials and different doping this will control the flow of electrons in an electric circuit. If a p-doped material is next to an n-doped material you will have a so called p-n junction, see figure 2.5. When this happen the Fermi level on both sides align and the bandstructure will have a slope in potential between the n and the p side. This is a diode, restricting the movement of electrons in one direction at a bias, but not in the other as the potential (energy difference) increase or decrease.

Different semiconductors with different materials put together make up a so called heterojunction. This gives even more advanced behaviour of the electronic device, since it is possible to engineer the electron flow.

Many different things influence the electric properties of materials. For example the lattice distance (the interatomic distance). Hence a strained lattice will have a different bandstructure than an unstrained lattice. Defects of the crystal will also influence the bandstructure. Because of this characterization of these materials on a atomic scale is important.

2.2.2 Solar cells

For more on solar cell devices J. Nelson have written an excellent book on the topic [7]. A solar cell device is in essence a diode that can lead a current when irradiated by light. When a photon arrive at the material it is possible that

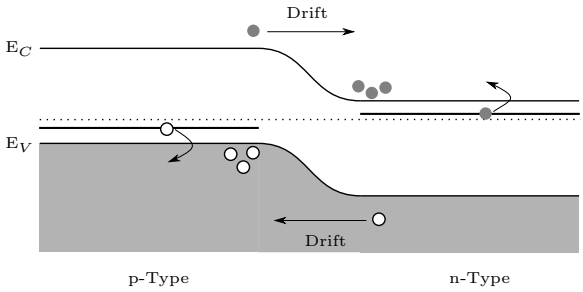

Figure 2.5: As a p- and an n-doped semiconductor are put together, the Fermi-level of the two will align and there will be a slope in the energy levels. In this slope electrons and holes will minimize their potential energy and move down to the bottom. The end result is a region in between with fewer electron/hole pairs than usual – the depletion region – and an electric field over this region.

it is absorbed in the shape of an electron excited over the bandgap from the valence band to the conduction band. If this happens in the junction there will be a local current since the electron will drift to lower energies. As the electrons start building up on one side of the junction (and the holes on the other) it will be possible to extract a current from the device.

The wavelengths of the sunlight that reach the earth is mainly limited to the range that human beings are also able to detect, see figure 2.6. This is still a broad range of energies. As previously mentioned the electrons in a semiconductor use the photon energy to cross the bandgap. This mean that it needs a photon that has at least the same energy as that of the bandgap. Any extra energy that the photon bring to the electron will however only be translated into kinetic and, in the end, thermal energy. This is of course a waste. This mean that for certain parts of the spectrum a lot of energy is lost.

The solution is multi-junction solar cells. These can be realized in different ways. One way is to split the spectrum into different parts by dichroic mirrors and let each part irradiate semiconductors with different bandgap. Another way is the so called tandem cell, where the pn-junctions are stacked on top of each other. If the larger bandgap junctions are on the top, it is possible to have the photons selectively excite electrons in the different materials.

The theoretical limit of multi-junction solar cells have been calculated. A two junction cell would maximally show an efficiency of 55% [7] whilst a four junction cell would have a theoretical limit of 71.7% [14].

Other issues to increase the efficiency of solar cells include optimizing absorption of light in the solar cell and increasing charge separation. The first is important since reflected light is not going to contribute to the current and can be addressed by adding a texture to the front surface. This is done

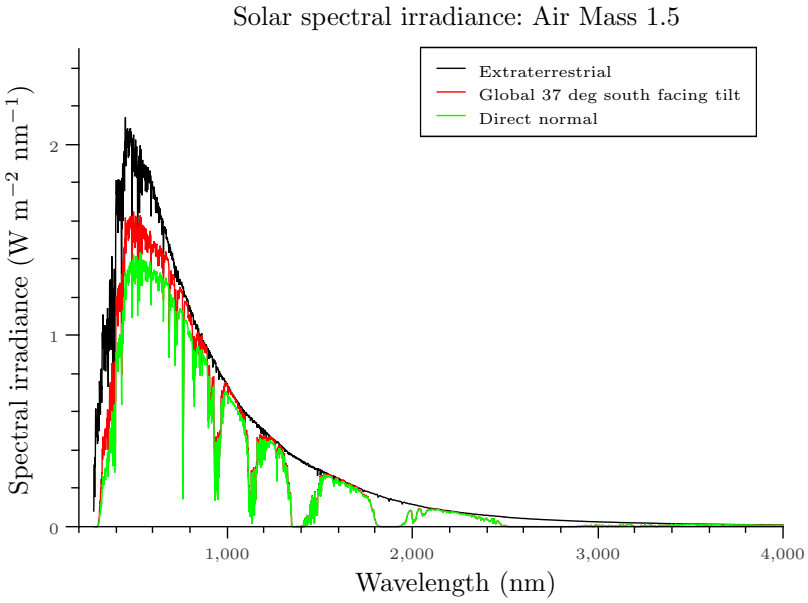

Figure 2.6: The extraterrestrial irradiance is larger than for the light hitting the earth surface, especially for certain wavelengths where the air molecules will absorb large amounts of photons. Most of the available energy is in the visual regime of the spectrum. Data from [13].

in such a way that the light is trapped inside the material, getting multiple chances of absorption. Carrier separation is important for the electrons and the holes not to recombine. [7]

2.3 Semiconductor nanowires

Nanowires can be defined as structures with two dimensions in the range of tens of nanometres and the third dimension usually much longer – often in the micrometer range [15]. These structures can be produced both top-down and bottom-up, i.e. both by shaping a larger piece of material into a wire, or by crystal growth processes. The wires used throughout this work were epitaxially grown semiconductor nanowires, usually grown from InP and/or GaAs. In figure 2.7 a SEM image of an InP nanowire sample can be seen as grown, still standing on the InP substrate where it was grown. This image show several typical features of these nanowires – there is some tapering and the surface do have a structure but generally the wires are straight, thin and precisely grown. Figure 2.8 show an example of nanowire morphology and TEM micrographs of the crystal structure. This figure introduce several concepts that will be dealt with in the coming sections (Crystallography, section 2.3.1, TEM and diffraction, section 2.4.5).

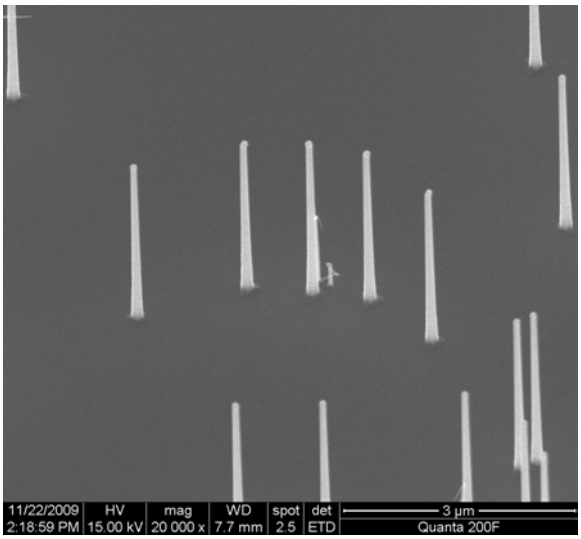

Figure 2.7: InP Nanowires grown on a InP substrate. These wires are ca 80 nm wide in the top and tapered so that the bottom is 110 nm wide. They stand about 2.3 µm tall. The image was aquired using a SEM as described in section 2.4.3

Growth of these types of structures started by Wagner and Ellis in the 60's [16], followed by Soviet researcher Givargizov in the 70's [17]. In the early 90's the topic became interesting again as Japanese researcher Hiruma managed to grow thinner structures and using III-V semiconductors [18]. Since then knowledge about the growth of nanowire systems and the effects of the quantum confinement in these systems have progressed quickly. A good review on nanowires can be found in [15].

Nanowires have several uses and have been foreseen to even more in areas such as electronics [19], photonics [20] and life sciences [21].

2.3.1 Crystallography

For a more thorough introduction to crystallography a good reference is [22]. There are many important phenomena within the nanowires that are dependent on the crystal structure. A fault or a change in the way the crystal is stacked can lead to a large change in the electronic properties. By using a TEM it is possible to directly see the positions of the atom columns in a crystal. Using diffraction techniques it is possible to tell what structure a material have and in what direction it is oriented.

Nanowires occur in a variety of crystal structures. For example CdO nanowires exhibit a rock-salt structure [23] and among the III-V semiconductor nanowires most show the zincblende (Zb) or the wurtzite (Wz) structures, see figure 2.9. It is also possible to get polytypism in nanowires and in

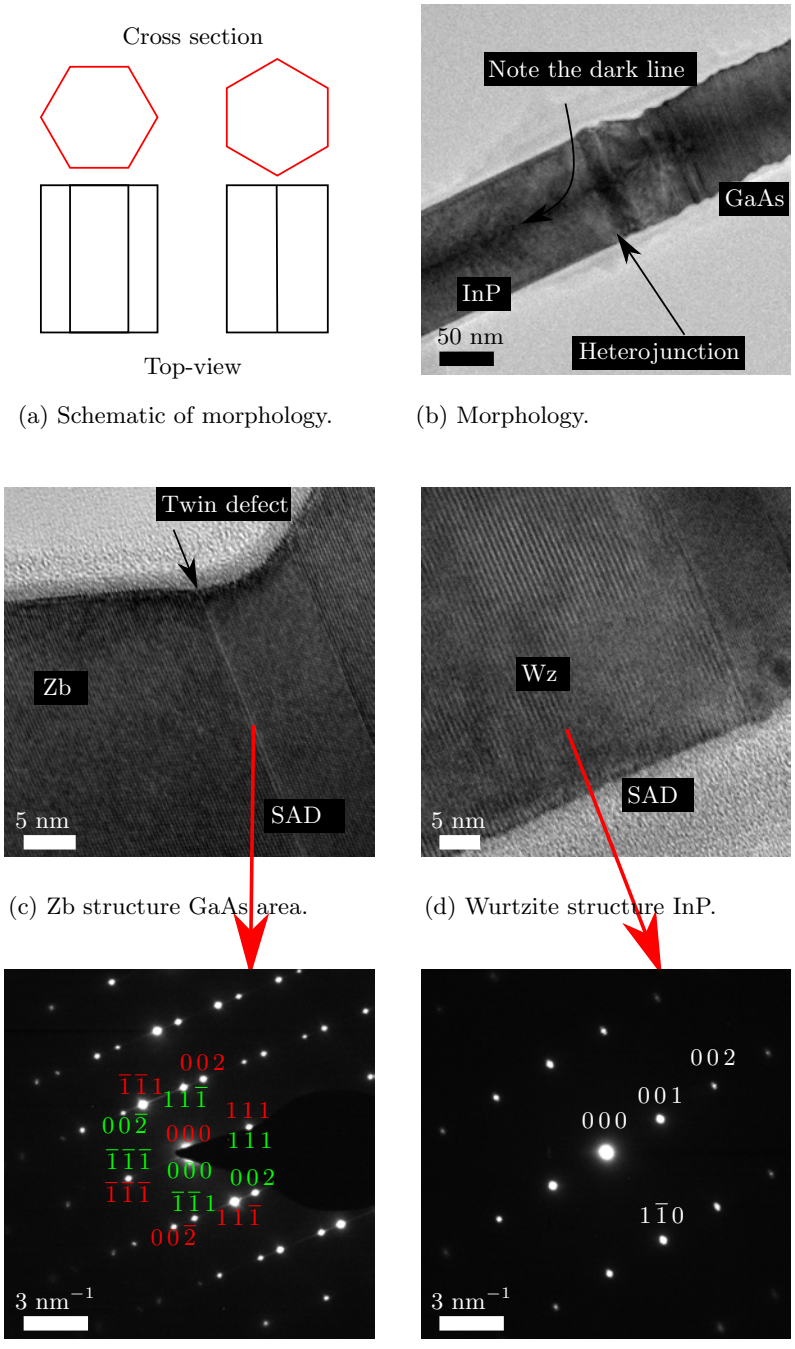

(a) Schematic of morphology.

(b) Morphology.

(c) Zb structure GaAs area.

(d) Wurtzite structure InP.

(e) Zb twin diffraction.

(f) Wz diffraction.

Figure 2.8: Hexagonal nanowires can be looked at in two different perspectives as shown in (a). In the overview image in (b) the dark line in the center of the InP indicate that we look at the wire in the direction shown to the right in (a). (b-f) Are all bright field TEM micrographs from the same hetero-junction nanowire. (c-d) Show the crystal structure of the GaAs and the InP and (e-f) the corresponding diffraction patters.

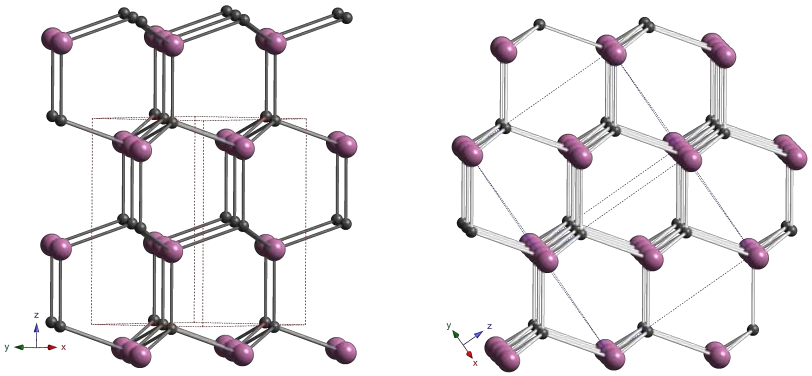

(a) Wutzite structure. (b) Zb structure.

Figure 2.9: Ball-and-stick models of the Zb and the Wz structures, tilted slightly off the [1 1 0] viewing direction.

some cases crystal structures that do not occur in bulk versions of the material. InP has been examined in this work and is one of the materials which can occur in Wz form in nanowires but normally would be Zb in bulk [24].

Both Zb and Wz are close-packed structures, i.e. given the premise that the atoms are spherical, they fill as much of the available space as possible. Only the packing sequence is different. The Zb structure is a face centered cubic structure and the packing is done in a ABCABC manner. The Wz on the other hand is a hexagonal structure with an ABABAB type packing.

The packing sequence is important because of what happens if something goes wrong. A Zb structure can often sport a so called twin defect, where the structure changes in one layer to it's [1 1 1] rotational twin. The packing sequence then end up ABCBA resulting in a small part of the crystal essentially being Wz. Since the electronic structure of Zb and Wz are different this is important to keep in mind. The band structure and the conductivity will change.

The crystallography is also important for interfaces. A mismatch between the lattice distances would induce a strain in the crystal. This will lead to differences in the band structure. If the strain is too large the resulting crystal will have defects in the interface area.

2.3.2 Epitaxial growth

Epitaxy is a crystallographic growth process where the substrate influences the film being grown to result in a matching of the structure in the interface. Neither the elements nor the structure of the two materials need to be the same. If the grown material differ from that of the substrate it is a so called heteroepitaxial growth, which is necessary in order to create the bandgap

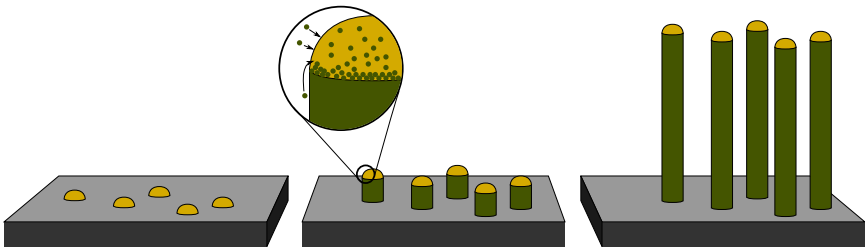

Figure 2.10: A schematic showing the nanowire growth MOCVD process. Gold particles are deposited on the surface using aerosol techniques making them an exact size. The gas precursors are let into the chamber and enter the gold particles. As the gold particle start to saturate, the semiconductor atoms can minimize energy by adhering to the surface in the bottom and letting go of the organic part. The organic molecule is transported away and slowly but surely a new crystal layer is built.

structures needed for solar cells.

There are several ways to accomplish this type of crystal growth. Here the process used was the metal organic chemical vapour deposition (MOCVD). In this process a precursor gas is flowing over the surface where the epitaxial growth is wanted. The gas is a metal-organic compound (or in this case it is more correctly a semiconductor-organic compound) consisting of the base material that should be grown. For elevated temperatures a gas molecule finding a preferred spot on the surface will tend to stick harder to the atoms in the surrounding crystal than to it's organic group. The bond to this group is broken and that part will go away with the flow.

For growing nanowires catalyst particles are used, see figure 2.10. The catalysts in this case are gold particles. The particles are placed on the surface of a single crystalline wafer using an aerosol technique described in [25]. This method ensures an exact size distribution. As the precursor gas is let into the chamber, it flows over the surface. With the temperature increased the gas will prefer entering the gold particle rather than adsorbing to the surface. For some materials the gold particle need to be heated until liquid or near liquid, but in other cases the temperature does not need to be that high for growth to occur. These two variants of growth processes are called VLS (vapor liquid sold) [16] or VSS (vapor solid solid) [15, 26] respectively.

As the gold particle get saturated, the system will minimize it's energy by letting the semiconductor atoms bind to the surface below the gold and letting the organic molecule evaporate. The end result is that of an epitaxial growth where the precursor gas is turned into layer by layer of a semiconductor nanowire.

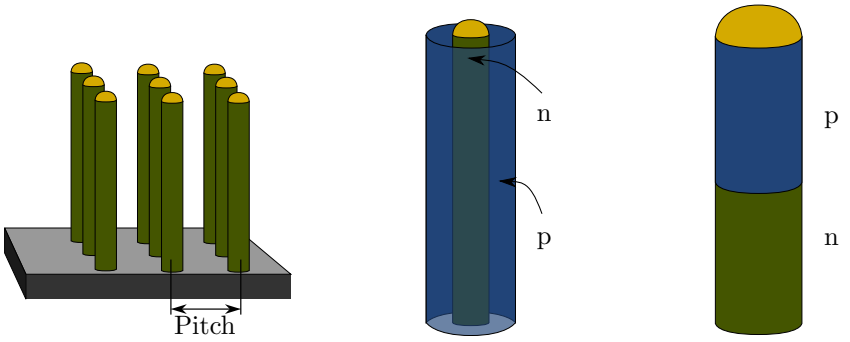

(a) Periodic array of nanowires.

(b) Radially grown (core/shell) nanowire p-n junction.

(c) Axially grown nanowire p-n junction.

Figure 2.11: Schematic over some different issues to consider when producing semiconductor nanowire solar cells. Ordered arrays of nanowires have different absorption characteristics than randomly distributed wires.

2.3.3 III-V semiconductor nanowires for solar cells

As stated in section 2.2.2 there are several issues with solar cells as they are made today. Utilizing as large parts of the spectrum as possible, enhancing absorption, minimizing recombination and the high cost of the material used all pose scientific challenges [7]. One way of potentially solving these issues is by going down in scale to nanometer sized structures such as nanowires. Even though this work has been on III-V semiconductor nanowires, there is and has been much advance using other material systems as well. For a good overview of this topic in its entirety a nice review on compound semiconductor nanowire solar cells has been written by Sun *et al.* [27].

Nanowire photovoltaic cells can be realized either using radial or axial heterostructures, see figures 2.11(b) and (c). These cells can then be used together as a solar cell, usually using the substrate they were grown on as a back contact [28–30].The nanowires are usually arranged in periodic arrays as in figure 2.11(a). Thanks to the one-dimensional structure of the nanowires there is a relaxation of the built in strain that accommodate for larger changes in lattice parameters than in thin films or in bulk. This make it possible to choose optimum materials and engineer the composition of the nanowires, giving very good control over the band gap structure and permits growing and contacting multi-junction structures [31].

The use of nanowires rather than conventional structures for solar cells results in low filling factors, hence using less material. It has been shown that the absorption, thanks to an optical micro-concentration effect, is comparable to conventional thin-film solar cell designs [32]. It is even possible to use the geometry of the nanowires and of the arrays in order to tune the

absorption of different wavelengths [33]. The lower filling factor saves material and bring down costs of the solar cells. The fact that nanowires can be grown on relatively cheap Si substrates also reduces the costs [34]. Kupec *et al.* found a theoretical optimal geometry to be periodically arranged nanowires with a pitch of 360nm and a thickness of 180nm [1]. For such a sample the theoretical efficiency limit would be 29.4%.

Another advantage for nanowires is good carrier separation. This is an important factor to minimize recombination in the photoactive region. Reasons include the electrostatic force being higher between the n- and the p-doped regions in a nanowire solar cell than in a thin film solar cell and the possibility of more advanced bandgap engineering in a nanowire. The latter is due to the higher lattice mismatch possible in nanostructures than in bulk or thin films [27]. There has also been work done on controlling the internal strain in Si nanowires, in order to optimize the charge separation [35].

One downside of using nanowires is charge transportation since the high surface to volume ratio increase surface recombination. Radial heterojunction nanowires are less affected than axial heterojunction nanowires. [31]

Some examples of materials used for III-V nanowire solar cells are GaAs, $Ga_xIn_{1-x}N$ and InP. A n-GaN/$Ga_xIn_{1-x}N$/p-GaN core/shell/shell system has been tested on a single nanowires test device and show a maximum efficiency of 0.19% [28]. A GaAs core/shell p-n junction [29] and a GaAs core/shell p-i-n junction [30] have also been realized, with 0.83% and 4.5% efficiency respectively. In both of these cases the measurements were done on single nanowires devices. For InP a core shell p-n junction with a efficiency of 3.37% has been implemented [36].

These values can be compared with the best device produced throughout the AMON-RA project. This was an InP axial single junction nanowire solar cell, that under one sun showed an efficiency of 12.98% (measured at the Fraunhofer ISE CalLab under AM1.5d, ASTM G173-03 spectrum at 1000W/m^2). This could be increased to 13.43% at 2.595 suns concentration. At higher concentrations the efficiency started to decrease again. [37]

To the best of my knowledge, at the time of writing no publications had yet been made showing the efficiency of the material systems that were used during this project, that is InP/GaAs axial heterostructures, $Ga_xIn_{1-x}P$ axial p-n junctions and InP axial p-n junctions. The theoretically ultimate efficiency of a two-junction III-V nanowire solar cell has been calculated to be 42,3% under 500 times concentrated sunlight [38]. This shows that there still is a lot of room for improvements.

2.3.4 On strain

Since strain is an important feature of semiconductors and since the measurement thereof has been discussed in this thesis this section will briefly introduce the topic. Strain is a well defined property that is easy to measure

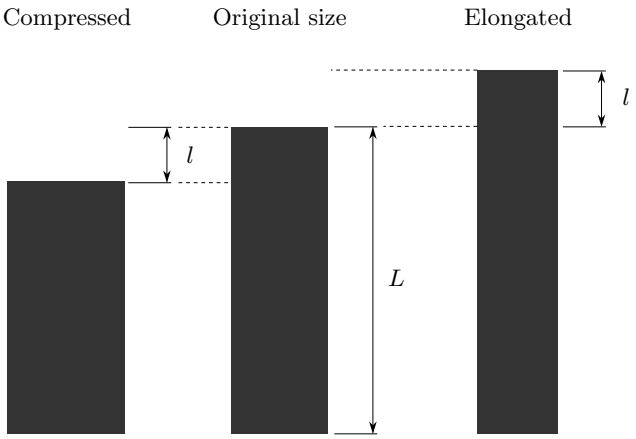

(a) Schematic of strain in bulk.

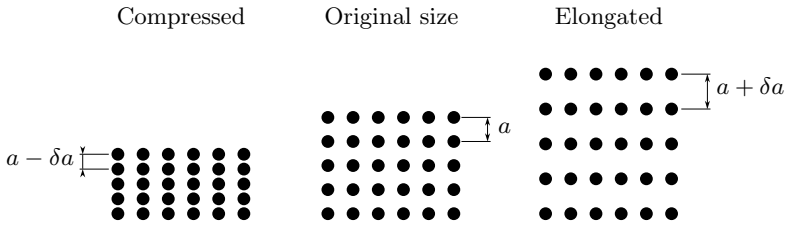

(b) Schematic of strain in a crystal lattice.

Figure 2.12: Schematics explaining the notion of strain in bulk and on an atomic scale.

in bulk, see figure 2.12(a). Simply measure the length of a uniform piece of a material before and after applying a pressure or pulling on it. The ratio of the deformation to the original size, i.e. $\frac{d(l-L)}{dL}$ where L is the original length and l is the new length, is the value of the strain. A positive strain signifies a pull on the material and is called a tensile strain while a negative value signify a compressive strain. [5]

Strain on the atomic level is defined in the same way, only here the distance between the atoms – the lattice distance – is the normal way of measuring strain, see figure 2.12(b). The importance of this figure is grave, with strain influencing the properties of the material on a fundamental level. Strain on this level changes the bandstructure [6] and thereby influence the behaviour of the material when used as an electronic device. In some electronics components strain is purposefully introduced, utilizing the changed behaviour [39, 40].

Nanometer scale measurements of the local strain can be obtained us-

ing different TEM based methods. Convergent beam electron diffraction (CBED) [41,42], geometric phase analysis (GPA) [43,44] and holography [45] has all been used for this purpose as well as direct analysis of the apparent distortion in HRTEM micrographs [46, 47]. Nanobeam electron diffraction (NBED) is also a method that has been used by several groups [48–50], and in chapter 6 in this thesis NBED has been further used to analyse the strain of a series of freestanding nanowires. It is also worth mentioning that using a TEM no longer is the only way to do this measurement – X-ray Bragg projection ptychography has recently been employed for this type of study [51].

2.4 Instrumentation and methods

2.4.1 Electron microscopy

Visible-light microscopes have a resolution limit of about half the wavelength of the light that is used according to the Rayleigh criterion. If two particles are illuminated with a wavelength of 500 nanometers, this means that they will be seen as one particle if they are closer to each other than ca 250 nm due to diffraction. Louis de Broglie suggested that also the electron would possess wavelike properties in the same way as visible light, only much shorter. As he was proven right, it is possible to create a microscope using electrons instead of photons as information carriers. The first electron microscope was proposed by Knoll and Ruska in 1932, a feat for which Ruska received a Nobel price in 1986. The evolution in technology of electron microscopes have been rapid and today it is an indispensable tool in material science and life science alike. [3]

For all types of electron microscope the basic principle is the same:

1. Electrons are accelerated from a gun down towards the sample.
2. Electromagnetic lenses interact with the electrons to shape the imaging beam.
3. The electrons interact with the sample, by loosing energy and/or changing direction.
4. Again electromagnetic lenses are changing the course of the electrons, this time in order to create the image on the detector.
5. Detectors record the relative change of the state of the electrons and present this to the operator.

Electron guns

There are two kinds of electron guns - those using thermionic electron sources and those using field-emission sources (field emission gun, FEG).

Thermionic emission of electrons occur when material is heated to a point where electrons in the material are close to or above the vacuum level (cf. the discussion about semiconductor bands in section 2.2.1). Depending on material properties different amounts of electrons can be assumed to be leaking out, with more electrons giving a brighter source. Thin filaments of tungsten and sharp LaB_6 crystals are the most common materials.

Field emission sources use a very sharp tip instead. Due to the small size of the tip it is relatively easy to accelerate electrons using an applied electric field; The electric field scale with the radius of the tip. Since it is essential that the tip stay sharp there can be no contamination. This mean that the FEG microscope have higher demands in for vacuum than thermionic microscopes, and whilst they do give a higher brightness, they are also more complicated in use and service.

The electrons are accelerated from the gun towards a circular anode with an aperture in the middle. The electrons that end up coming through the aperture have been accelerated with a tension of tens of kV for a scanning electron microscope and in the order of hundreds of kV for a transmission electron microscope.

Electron lenses and aberrations

Whilst electrons can be diverged and converged in a controlled manner by placing a physical object in their way, lenses in the microscopes are not like glass lenses in the visible-light microscopes. Any physical optics would make the electrons loose too much energy resulting in a lower brightness, and the lenses would be damaged from long term irradiation. Instead an electron microscope uses electromagnetic fields in order to converge the electron beam. There is no way to diverge electrons using normal centrosymetric magnetic lenses, which have led to specially engineered solutions being developed to compensate. Electromagnetic lenses use charged electric coils to create the fields. A simple change of the bias over the magnet will result in changed strength of the field and the lens.

Electron optics have all the same aberrations as visible light optics. Chromatic aberration is a result of the path of electrons with different wavelength being changes by different amounts in a lens. This can be averted somewhat by making sure that the light is monochromatic; Minimizing the source energy spread or introducing a monochromator goes a long way, but energy loss in the sample will still introduce an energy spread. Astigmatism occur when a lens imperfection give different optimum foci for different directions – an astigmatic lens would image a cross with one line in focus and the other out of focus. Since the strength of the electron optical lenses easily can be changed a set of complementary lenses can together compensate for any astigmatism in the imaging system. Coma is an aberration that refer to the image not being on the axis of the optical system, meaning that only

one plane of the image will be in focus at a time. As with astigmatism a set of lenses can remove the coma.

Until recently there was no way of correcting the spherical aberration of electron optics. Spherical aberration arise as the path of electrons further from the optical axis (closer to the magnetic coils of the lenses) is unproportionately more bent than a that of an electron closer to the center – a point in reality will look like a disk in the image. For visible-light optics it has been possible to correct for this by using divergent lenses – something that doesn't exist for electrons. The solution for this is to use a complex series of different lenses to imitate a divergent lens. This was proposed in the 40's by Scherzer and worked out in the 70's by Rose, but was not practically feasible until modern computers came along to measure the aberration and to control the lenses in the correction unit [52].

Sample-Electron interaction

When negatively charged electrons interact with the sample they will scatter in the field of the positively charged atom cores, or by collisions with the particles in the atom. The nature of this scattering can be either elastic or inelastic. In the case of elastic scattering the electron will change the direction, but maintains its energy. An inelastically scattered electron however, changes both its energy and direction. The energy lost will be transfered to the sample where it will be turned into heat, move atoms around (damage of the sample is common at higher energy beams) and/or result in secondary electrons and x-rays being irradiated from the sample.

An elastically scattered electron can go onwards into the material and scatter again, or it can do a more than 90 degree turn and return out the way it came. The latter electrons are called backscattered electrons. The likelihood of getting backscattered electrons will increase with the atomic number of the material. Roughly following Rutherford scattering principles, an element with a larger positive core and hence a larger atomic number will scatter the electron more.

For a thin enough specimen, elastically scattered electrons will go on through to the other side. If these are scattered to a low angle they are still coherent with the primary (non scattered) beam and can as a result interfere with the primary beam.

Electron detectors

The human eye cannot detect electrons – and putting our eyes in the direct beam of electrons would indeed hurt – so the effect the sample had on the electrons will have to be detected and presented indirectly. For an electron microscope working in transmission, section 2.4.5, the most straightforward way is to place a fluorescent screen in the beams way. The electrons will

excite the material in the screen and this will send out photons that can be seen by the naked eye. If the information needs to be saved the fluorescent screen can be exchanged for a photographic film or a CCD (charge-coupled device – the image sensor that is also used in digital cameras) using a scintillator where a fluorescent screen converts an electron to a photon that can be subsequently multiplied and detected.

Direct electron detectors are also used, especially in modes when the electron beam is focused to a probe on the sample surface as opposed to the direct image mode. Here it makes sense not to detect individual pixels and instead have a detector with a very high sensitivity and a quicker readout. These detectors can either be direct semiconductor detectors, using a process similar to that of a photovoltaic cell as described in section 2.2.1, or it can use a scintillator like the CCD.

Electron diffraction

In diffraction coherent beams escaping the sample are caught with a detector in the back focal plane instead of the image plane. This plane, also called the Fourier plane, contains the diffraction pattern from the sample. Diffraction is the result of the electron waves interfering constructively and destructively due to ordered scattering, cf. diffraction of light in a periodic lattice as can be found in any physics primer. A schematic of the process for Bragg diffraction can be seen in figure 2.13. The resulting pattern is a reciprocal image of the crystal and can be used for determining the crystal structure, lattice parameters and morphologic parameters such as tilt and rotation.

In section 2.4.5 several ways of extending the information obtainable by diffraction are presented. These include using a convergent beam on the sample to get a convergent beam electron diffraction (CBED) pattern. This can be used for thickness and strain measurements. Diffraction techniques for materials characterization is especially important for chapter 6.

2.4.2 Spectroscopic techniques in electron microscopes

In spectroscopy a measurement a response is probed as a function of energy and the resulting spectrum is used in order to study material properties. Two spectroscopy methods frequently built into electron microscopes are energy dispersive X-ray spectroscopy (EDX[1]) and electron energy loss spectroscopy (EELS).

EDX is a much used spectroscopic method sensitive to heavier elements. As can be seen in the schematic in figure 2.14, electrons that scatter inelastically within the sample might make a secondary electron leave the atom,

[1]There are several acronyms for energy dispersive X-ray spectroscopy: EDX, XEDS, EDXS, EDS and EDAX. EDAX is actually a brand name and is fortunately not used much today.

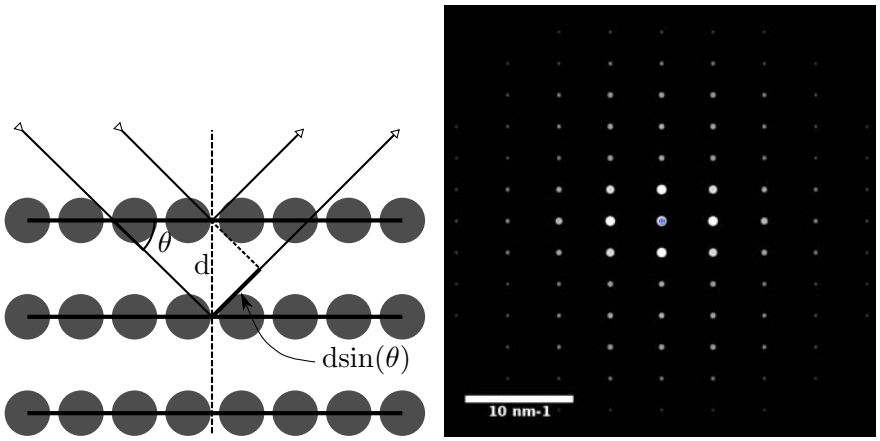

(a) Bragg diffraction.

(b) Simulated InP diffraction pattern in the [1 1 2]-direction.

Figure 2.13: (a) Bragg diffraction in the planes of a crystal. If the difference in path length for the wave reflected in the first atom plane and in the second is a whole wavelength, the result is constructive interference. If this difference is half a wavelength they will interfere destructively. The resulting pattern projected onto a CCD in the back focal plane will be a pattern such as that in (b).

or at least excite it to a higher energy level inside the atom. As that electron state in the atom is again filled, the electron filling it will lose its potential energy which in turn will be released in the form of a photon with an energy in the X-ray range. This photon can be detected by a scintillator and its energy can be measured and positioned on the spectrum. The energies of the extracted X-rays are called characteristic X-rays and are unique to each element and hence it is possible to know what the sample consist of and even quantify the relative amounts. The full set of possible x-ray emissions can be seen with their traditional names in figure 2.15. Another type of X-rays from the electrons interaction with a sample is the Bremsstrahlung that occurs as the electron looses energy in a velocity change, for example when being pulled into a new path by the positive core of an atom. Detection of this is inevitable and this give a background to the spectra.

A typical EDX spectrum can be seen in figure 2.16. This example is from an GaInP nanowire. The inset shows the In_L-peaks more clearly.

Whilst qualitative EDX is very straightforward it is often more interesting to make a quantitative study of a sample, something that is less easy. As the electron beam pass through the sample an element with a certain weight will emit a certain flux of X-rays. The X-ray flux is proportional to the amount of a certain element in the probed sample. This can be used to figure out relative amounts of elements in a material. The composition can

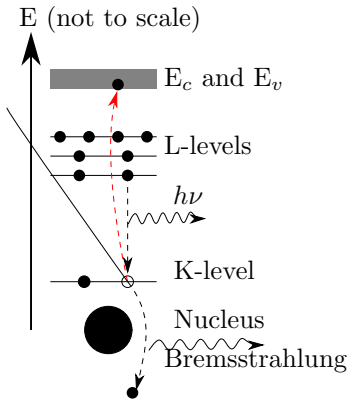

Figure 2.14: A schematic showing the process in the microscope responsible for creating the X-rays analysed through EDX. A K-level electron hit by the incoming electron gain eneough energy to be excited to the conduction band. An electron from the L-level loose energy and recombine with the hole left in the K-level. In the process it emits out a photon of energy $h\nu$, where h is the Planck constant and ν is the spatial frequency. In due time also the hole in the L-level will be filled by another electron emitting a second photon in the process. As the impacting electron move closer to the possitively charged nucleus it bends towards it. In this process it changes it's momentum and send out so called Bremsstrahlung X-rays. Figure inspired by [3]

be calculated by integrating the element peaks and using the Cliff-Lorimer factor which essentially is the relative proportionality of the emitted X-rays and the number of atoms of a certain element. Commercial software exists to deal with this analysis. This software is not necessarily reliable and will often need a human eye to correct erroneous behavior. This is especially true for measurements with a low count of X-rays which might be necessary if the sample is beam sensitive.

There are several different steps where things can go wrong in the quantitative analysis of a EDX spectra. There will always be a background of X-rays arriving to the detector from the Bremstrahlung as can be seen in figure 2.14. This background needs to be subtracted from the spectra in order to get an accurate integrated count for each peak. There are several algorithms that can be used for this, but if the count is low this is likely to be wrong. A second thing that is necessary is having a good calibration since even a slight shift can cause the software to wrongly identify a material to be present.

Atomic resolution EDX was first presented in [53]. The method is not yet quantitative, but a good agreement between theory and experiments indicate that this might be possible in the future [54]. Under normal circumstances the spatial resolution of the EDX method is not that good. The basic parameters it depends on are the size of the probe onto the sample

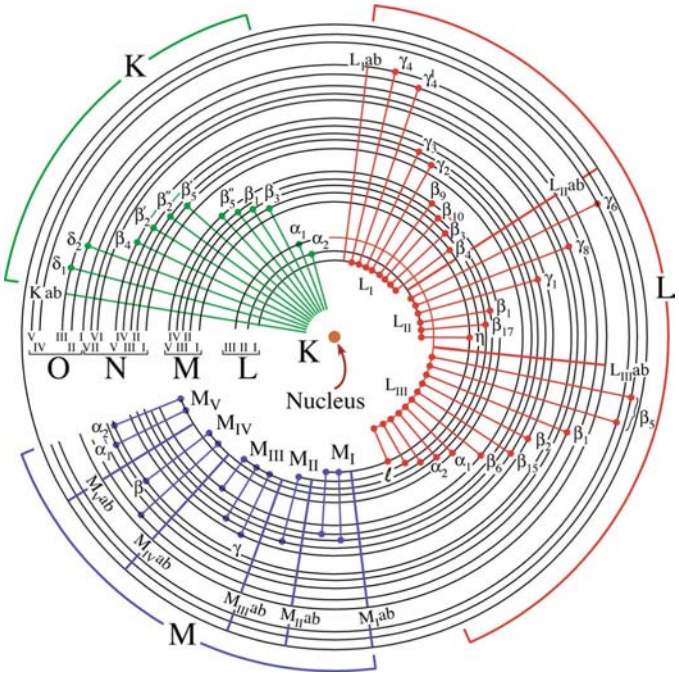

Figure 2.15: Possible x-ray emissions. K, L, M, N and O denote the different energy levels in which the electrons can subside, cf. section 2.2.1. Each level, save K, are divided into sublevels. Electrons reducing their potential energy by moving to occupy a hole in a lower energy shell, will emit photons of the corresponding energy. Whilst the names of these emissions, such as "K_{α_1}", are systematic they are set out of tradition. Together the energies that can be found emitted from a material work as a unique fingerprint for that material. Image copied from [3].

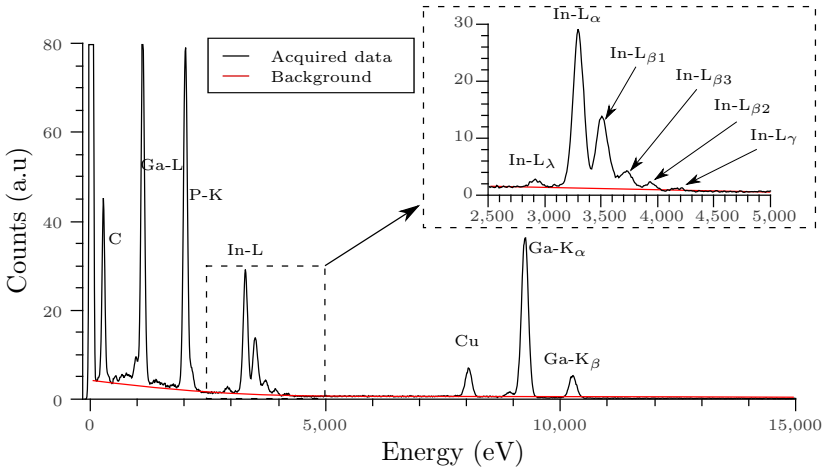

Figure 2.16: Typical EDX spectrum. The inset shows the In-L peaks in more detail. The red line corresponds to an approximated background fit. This will be subtracted before any quantification can be done. The C peak is probably partially contamination and partially from the lacey carbon grid. The Cu stem from stray electrons entering the Cu-mesh grid-bars around the wire.

and the spread of the beam inside the sample. The former depend on the convergence angle of the beam, and the latter on the thickness of the sample and the atomic weight of the material.

The thickness is an issue since the electrons spread in a material as they bounce around among the atoms. The resulting interaction volume from the sample will look like in figure 2.17. The characteristic X-rays can exit the sample and enter the detector from anywhere in this volume.

The detection limit depends on the count-rate of X-rays above the background, i.e. peak to background ratio, and on the acquisition time. What can be detected is also determined on there being no overlapping peaks of

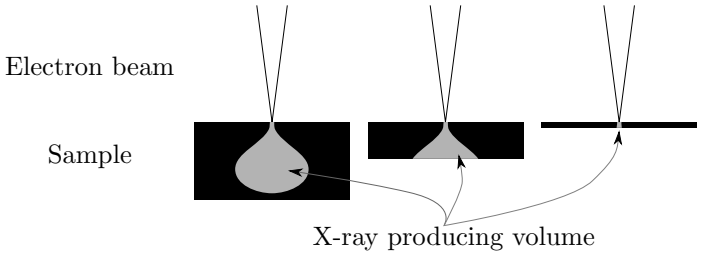

Figure 2.17: A schematic showing the X-ray producing volume of the sample, upon it's interaction with the electron beam. A thicker sample has a larger interaction volume, and as such the spatial resolution is worse.

the characteristic X-rays.

Another spectroscopy method often used in electron microscopy, albeit not in this project, is EELS. Here the energy lost by the transmitted electrons is measured. For a thin enough sample it is assumed that the electrons undergo only one scattering event. The energy transferred from the electron to the sample is well defined and again specific for each element. EELS have a higher sensitivity for lower atomic mass elements than EDX, is faster and have a higher spatial resolution. There are however several element combinations that are very tricky to examine in EELS due to edge (peak) overlap. Furthermore EELS require very thin samples and the spectra are less straightforward to process than EDX spectra.

The same optical elements that are used for EELS, a series of lenses used for spectrum splitting and a slit for choosing a particular energy, can also be used for energy filtered imaging. This is very useful in cases where inelastically scattered electrons might overshadow the signal from elastically scattered information carrying electrons. One example where this is necessary is in CBED.

2.4.3 The scanning electron microscope

The scanning electron microscope (SEM) is a versatile instrument with a shallow learning curve. An excellent introduction can be found in the book by Hawks and Spence [55]. A schematic can be seen in figure 2.18. Electrons are accelerated from the gun with energies usually in a range from 1-30keV, down through the lens system creating a tiny probe on the sample. This probe is scanned across the surface using a set of scan coils.

As discussed earlier an electron entering the sample will interact with it by scattering. In SEMs the sample is bulk, so there will be no transmitted electrons[2]. Secondary electrons (SE) have a low velocity (energy) and can be attracted towards the SE detector using an applied positive bias between the sample and the detector. Backscattered electrons (BSE) are detected with an annular detector around the pole piece of the electron column - BSEs are so high in energy that they travel in any direction even when the SE detector is on, so both detectors can be used simultaneous. Whilst the BSE signal give good Z-contrast (atom number) due to increased scattering from larger atoms, the SE signal show the morphology and, due to the positioning of the detector, give the user a sense of depth in the produced micrograph.

It is also possible to measure electrical properties of the sample using so called electron beam induced current (EBIC) and to measure optical and electrical properties using cathodoluminescence (CL). Diffraction in SEMs is possible using the incoherently scattered electrons with a technique called

[2]There are special transmission holders and detectors available for SEMs as extra optional equipment.

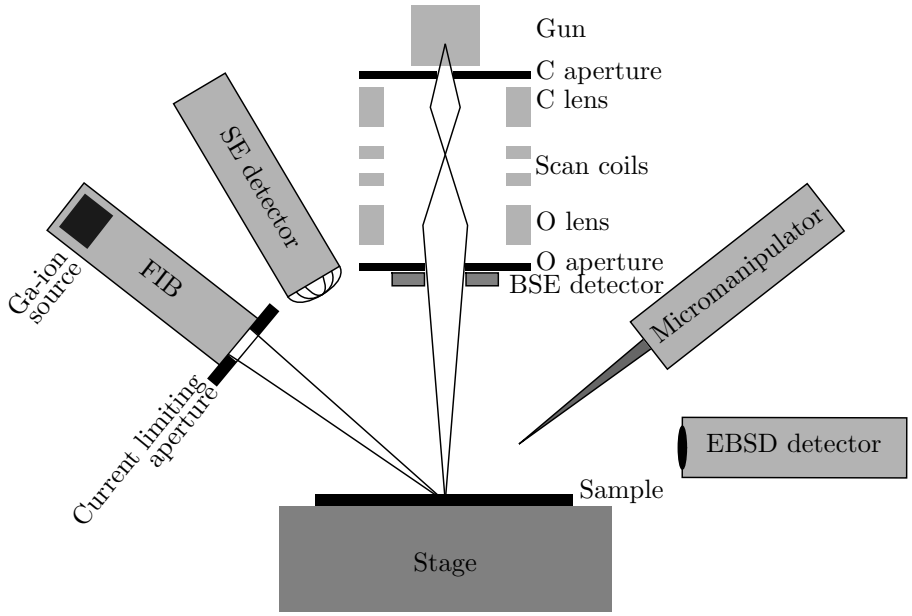

Figure 2.18: A schematic of an SEM equipped with a focused ion beam (FIB) and a micromanipulator. The electrons from the gun are focused onto the sample using one condensor (C) lens and one objective (O) lens. In between these lenses are the scan coils that scan the probe along the sample. Electrons are scattered from the surface and detected by one of three detectors, the secondary electron detector, the backscatter electron detector or the CCD that is the electron backscatter detector.

electron backscatter diffraction (EBSD), and SEMs are often equipped with X-ray detectors for EDX analysis.

2.4.4 The focused ion beam microscope

In a focused ion beam (FIB) microscope an ion beam is directed towards the sample instead of the electron beam of the SEM. The ion beam can be a complement to an electron beam, as in figure 2.18 or be the only beam in the microscope. If both types of irradiation possibilities exist in the same machine, it is often talked of as a dual beam machine (though a dual beam machine can also refer to a machine with two ion beams or two electron beams). The ions, often gallium, are focused onto the sample in a similar way to the electron beam. As the ions hit the atoms of the surface, these get excited and send out secondary electrons that can be detected with the same SE detector used for an SEM. Due to its size each ion will generate more secondary electrons than an electron would, and with a smaller penetration depth. This can be used to gain a higher resolution, since the resulting probe will be small and so will the interaction volume.

Ions radiated with a high enough current and voltage can also be used to manipulate the sample in various ways. By simply focusing the beam onto the surface, it is possible to use it as a negative lithography tool, removing material by thermal or knock-out effects. By introducing small amounts of various gasses, usually a metal attached to a hydrocarbon group, it is possible to use the ion beam to deposit material onto the substrate surface (cf. section 2.3.2 on epitaxial growth). The ion beam breaks the bond of the metal-hydrocarbon molecule, the hydrocarbon radical fly away and the metal adhere to the surface as a positive lithography.

In this work the FIB instruments were used mainly as a sample preparation tool, and less as an instrument for analysis. A micromanipulator was used to interact with the sample *in-situ*. This was a long needle made from tungsten with a set of precise motors connected to move it with micrometer precision inside the chamber. See chapter 3 for a description of how the sample preparation was done.

2.4.5 The transmission electron microscope

In transmission electron microscopy (TEM), the electrons interact with a thin specimen and pass through to the other side. A schematic of the TEM can be seen in 2.19. The resulting image is a projection of the material situated in the way of the beam.

Electrons are extracted from the tip of a gun as in the SEM, but are generally accelerated to much higher energies; TEMs often work in the range between 80 and 300keV, but there are those using 1MeV and more. A series of lenses are used to project the beam towards the sample, either as

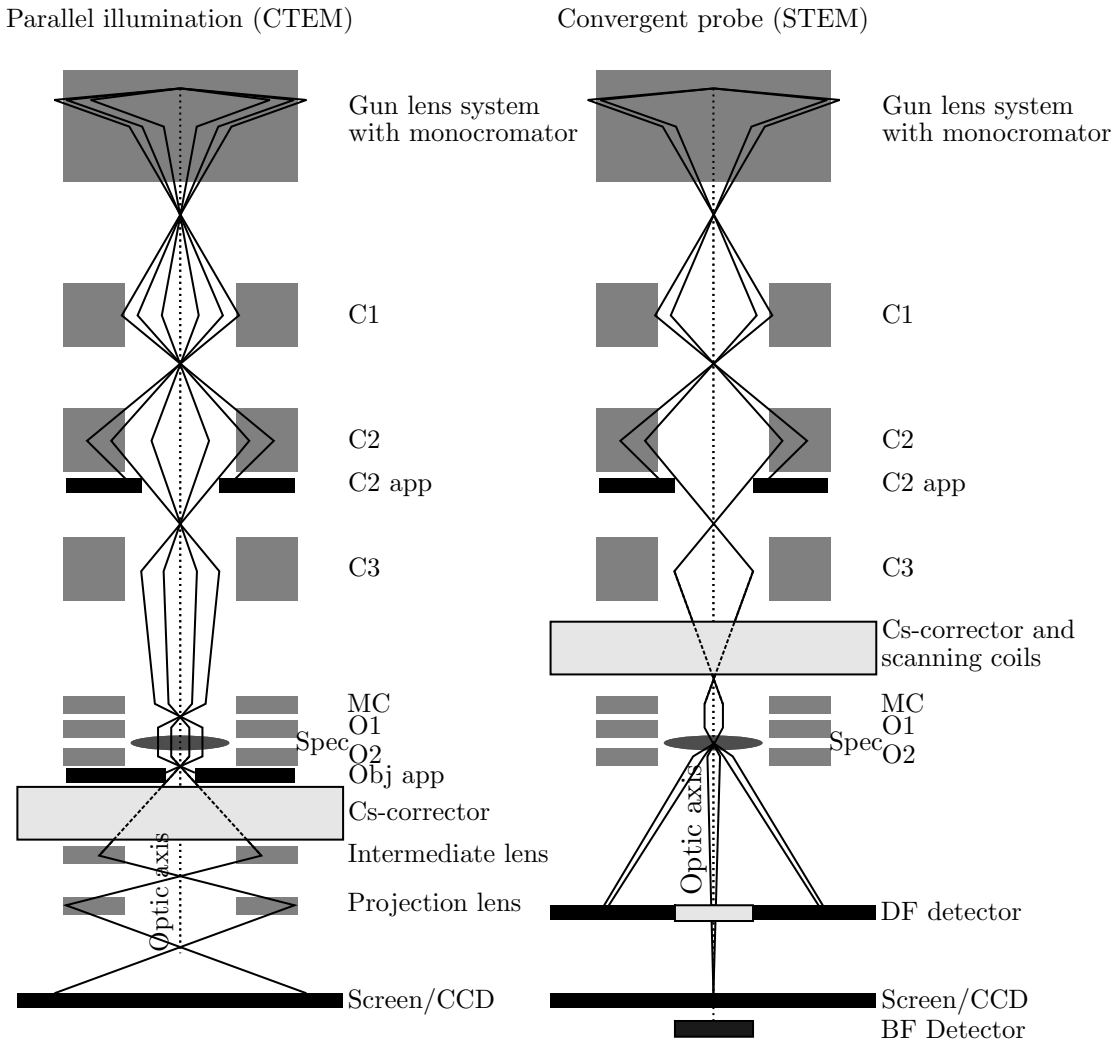

Figure 2.19: A schematic of a TEM in CTEM mode and in STEM mode respectively. The beam go from the gun/monocromator unit through the condenser (C) system, with the C2 aperture holding special significance for STEM mode. In HRTEM mode one wish to have the C_S-corrector below the objective lens system, in order to correct the image. In STEM mode the C_S-corrector is instead above the sample in order to make the probe as small and exact as possible onto the sample.

a scanning probe like in the SEM called scanning TEM (STEM), or as a parallel wavefront projecting the sample down to a detector. The latter is often called conventional TEM (CTEM).

The lens system used is similar to that of an SEM, only more complex. Figure 2.19 show a schematic of the two operation modes of the two FEI Titans available at the Center for Electron Nanoscopy. These are more complicated than the smaller instument, the FEI Tecnai, and boast monochromators, C_S-correctors and one extra condenser lens. The higher resolution and versatility of these instruments come with the downside of being harder to operate, with a steeper learning curve.

The electrons arriving at the sample will scatter both elastically and inelastically, but if the sample is very thin it will nominally only scatter once. In CTEM mode the end result is a shadow of the sample – a CCD placed below the sample will see vacuum as bright and the sample as a dark area. If the sample is thin enough there will be structure in the projected image with thicker parts being darker and elastically scattered electrons giving raise to so called diffraction contrast.

High resolution transmission electron microscopy

By minimizing all the lens aberrations it is possible to get the point to point resolution of a TEM very high. If the sample is crystalline and aligned in such a way that the atoms can be seen in columns with vacuum in between (cf. figure 2.9), it is possible to resolve these atom columns. Techniques for acquiring and analysing such data is called high resolution electron microscopy (HRTEM).

Scanning transmission electron microscopy

To the right in figure 2.19 is the basic principle of a C_S-corrected Scanning TEM (STEM). As in a SEM, the electron beam is focused to a tiny probe on the sample. The resulting scattered electrons go through and are detected by electron detectors. As the beam is scanned across the sample the micrograph is built up pixel by pixel.

If the electrons go straight through the sample and is detected either using the bright field detector or the CCD, the micrograph will look very much like that of the TEM – vacuum is bright and material is dark. The image is also distorted by diffraction contrast in the same way as in the TEM. If the electrons scattered further out is detected instead, ignoring those in the central beam, the image is instead an annular dark field (ADF) image with vacuum black and the sample bright. The higher angle the electrons are scattered to, the more similar to Rutherford scattering it is, and less of the signal will come from diffraction contrast. The high angle ADF (HAADF) signal is to a good approximation only dependent on thickness of the sample

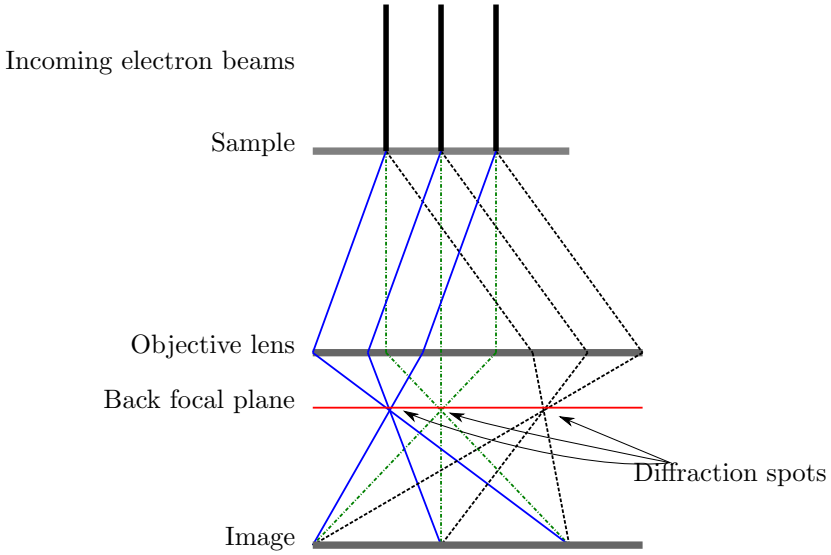

Figure 2.20: A schematic showing the origin of the diffraction spots in TEM. Beams diffracted in the same direction will go through the same point in the back focal plane, resulting in spots or discs of higher intesity. In this way the entire illuminated part of the sample will essentially contribute to every part of the diffraction pattern.

and of Z, the atomic number of the atoms.

Diffraction in a transmission electron microscope

During CTEM or high resolution imaging, diffraction patterns are obtained by changing the objective lens system so that the back focal plane rather than the image plane of the projection system is focused on the detector. The result for a crystalline sample is an intense central spot and less intensive side spots, all with contributions from the whole irradiated part of the sample. A general schematic of this can be seen in figure 2.20. The electrons entering the sample will have an energy in the order of 100 keV and hence a (non-relativistic) wavelength of about 0.00386 nm which is much smaller than the lattice plane distance of any crystal. Electrons are mainly scattered by the positively charged nuclei of the atoms and will scatter more in a sample with heavier atoms. This large scattering give rise to many dynamic scattering effects [3].

It is often interesting to look at only a small area of the sample to investigate local crystal structures. This can be done either by making the illuminated area small and hence get a convergent beam on the sample, or by inserting an aperture in the image plane of the objective lens. The former

lead to a convergent beam electron diffraction (CBED) pattern and the latter to a selective area diffraction (SAD) pattern. Whilst CBED contain much more information than SAD patterns, SAD is easier to acquire and to analyse and is therefore more common. In this work nanobeam electron diffraction (NBED) have also been explored, where the third condenser lens of an FEI Titan 80-300 was used to keep the beam parallel but get the probe as small as possible. More on this in chapter 6.

Kikuchi diffraction is the name of a special type of diffraction also used in this work. It occurs when incoherently scattered electrons are diffracted in the planes of the sample. Kikuchi diffraction appears on the detector as two parallel lines, one bright with an excess of electrons and one dark due to deficiency of electrons. In fact, these lines are electron beam cones stemming from each plane of the crystal due to Bragg diffraction, but the projection to the flat detector surface and the small field of view in the TEM make them look like lines.

The pair of lines are often referred to as a Kikuchi band and when in a zone axis containing several diffracting planes these bands will seem to cross in a so called Kikuchi node. The nodes are connected to other zone axes containing the same diffracting planes making it possible to utilize the Kikuchi diffraction pattern as a map in order to move from one zone axis to another.

2.4.6 X-ray Diffraction

Coherent X-rays can be produced in the lab using a rotating anode setup where electrons are accelerated from a cathode in vacuum to an anode made out of W, Cu or similar heavy materials. As the electron impact on the anode the same thing happen as in the EM – X-rays exit the anode. From the photons emitted a monochromator is tuned such that the utilized X-rays correspond to a sharp and high-intensity peak, cf. section 2.4.2 on X-ray emission in EDX. These depend on the material used as a cathode but is in the order of a few kV, which in turn correspond to a wavelength in the order of 0.1nm. Unlike in electron diffraction most of the scattering of X-rays stem from interaction with the negatively charged electrons in the material. These electrons are effectively working as antennas, inductively gaining the energy from the impinging X-rays electromagnetic field and in the next instant emitting an identical photon **??**.

These types of setups do not provide very bright or perfectly monochrome sources of X-rays but are still useful for many applications. In X-ray diffraction (XRD) the X-rays are directed towards a crystalline sample and diffraction such as described previously for the electron will occur. The resulting diffraction can be detected using a photodetector scanning the surrounding space. With a rotating anode setup in the order of a square millimeter of the sample will be irradiated at the same time, making this ideal for ensemble

measurements or bulk measurements, but not so good for local information.

Increased monochromaticity and much higher brightness of the source can be found in a synchrotron facility. There the X-rays are produced by undulating electrons and can be tuned to an exact energy. In the experiment in chapter 5 an energy of 8.9keV was used. The result is a highly monochromatic, coherent wavefront of X-rays. The high intensity make it useful also to use different types of X-ray lenses to focus the beam to a probe. Using these lenses probes as small as a few hundred nm are available at many synchrotrons, with the record probe being smaller than 10 nm. This of course giving a more local information and in conjunction with increasingly better stages make it possible to do X-ray diffraction of small individual crystallites or particularly interesting regions of a sample. [56, 57]

Part II

Results

Chapter 3

Sample preparation

3.1 The samples used

Even though a very large number of samples have been analysed during this PhD-thesis, only a few are featured in this work. An overview of the samples used can be seen in 3.1.

The samples were prepared using methods described in chapter 3 from specimens grown by and provided from researchers at Lund University and the Lund based company Sol Voltaics AB. Due to the commercial interests of the latter, their specimens will not be discussed in detail. All samples were grown in a MOVPE system, as described in section 2.3.2. Precursor gases for all these wires were for In trimethylindium (TMI), for P phosphine (PH_3), for Ga trimethylgallium (TMG) and for As arsine (AsH_3).

Lund University specimens

Samples S76a, L76a and L76b all come from the same specimen. This specimen consists of nanowires grown on an InP (1 1 1)B substrate. The Au aerosol particles used were 80 nm in diameter, and they were dispersed over the surface at a density of 0.2 μm^{-2}. The nanowires were heterostructure nanowires, where the first section was InP and the second was InAsP. Finally the whole wire was covered with a shell of InP, in an attempt to strain the InAsP core. The core InP section was grown at a temperature of 400 °C for 10 min, and the InAsP section for 5 min. The radial shell was grown at 550 °C for 2 min. The resulting wires were on an average 150 nm thick and stood ca 3.1 µm tall on the substrate. Wires from an identical sample have previously been presented in [58].

W65a, b and c are from the same specimen. This was grown on an InP (1 1 1)B substrate using Au particles of 80 nm in diameter at a density of 0.2 μm^{-2}. The nanowires were heterostructure nanowires with the first section InP (420 °C, 10 min) and the second GaAs (420 °C, 10 min). In between the

sections was a 4 s period with no precursor gas, in order to empty the Au particle of In. HCl was used to prevent radial growth, as presented in [59].

W45a, b and c are from a specimen grown in the same way as W65, but with no waiting time between the sections. A sample from the same specimen was presented in [60] including details of the growth process. HCl was used to prevent radial growth.

W74a and b as well as W865a, b, c and d are from two specimen presented in [61]. These were part of a larger series of nanowires studying growth of the ternary $In_xGa_{x-1}P$ system with regards to temperature and value of x. They were grown from 80 nm Au particles randomly dispersed with a density of 4 μm^{-2}. Nucleation was initiated with a InP segment at 420 °C and then raised to 460 °C. A GaP section was grown (1 min) before TMI was again added for the W865 specimen. Growth continued for 15 min, before all precursor gasses were switched of simultaneously. For W865 the TMI:TMG flow ratio was 2:1. HCl was used to prevent radial growth.

Sol Voltaics specimens

Samples C49a and b are from a specimen featuring InP wires grown on a Si (1 1 1)B substrate. The Au particle was 80 nm in diameter and randomly dispersed on the substrate surface.

Sample L02a is also from a specimen of InP wires grown on Si (1 1 1)B. However, in this case the gold particles were not randomly dispersed over the surface. Instead they were ordered in a hexagonal pattern upon the substrate. On top of the wires ITO, SiO_2 and an Au layer were applied in order to make the sample into a photovoltaic cell.

Table 3.1: The samples that were used throughout this work have been described here. Samples from the same batch are separated from other batches with horizontal lines. The value in the "Diam."-column signifies the diameter of the gold particle or the gold particle and added thickness of a shell as given by the scientist performing the growth.

Name	Description	Diam.	Experiment	Section	Ref.
S76a	InP-InAsP heterojunction on InP substrate, with a grown InP shell	150 nm	FIB damage	3.3	[58]
L76a	InP-InAsP heterojunction on InP substrate, with a grown InP shell	150 nm	FIB damage & Single nanowire lift-out	3.3	[58]
L76b	InP-InAsP heterojunction on InP substrate, with a grown InP shell	150 nm	Single nanowire lift-out with minimized milling	3.3	[58]
L02a	InP wires grown on Si substrate, with a thin ITO layer and gold on top	100 nm	Single nanowire lift-out	3.3	
W45a	InP-GaAs heterojunction nanowire	80 nm	Gold particle analysis STEM	4.1	[60]
W45b	InP-GaAs heterojunction nanowire	80 nm	Gold particle analysis tomography	4.1	[60]
W45c	InP-GaAs heterojunction nanowire	10 nm	Gold particle analysis EDX	4.1	[60]
W74a	GaP nanowire	40 nm	Gold particle analysis STEM	4.1	[61]
W74b	GaP nanowire on InP substrate	80 nm	Substrate surface contamination & CBED & GPA	4.3 & 6.3	[61]
C49a	InP on Si substrate	80 nm	Gold particle analysis HRSTEM	4.1	
C49b	InP on Si substrate	80 nm	XRD and TEM comparative study	5	
W865a	InGaP nanowire	80 nm	$[\bar{1}\,1\,1]$ rotational twin HRTEM	4.2	[61]
W865b	InGaP nanowire	80 nm	$[\bar{1}\,1\,1]$ rotational twin TEM	4.2	[61]
W865c	InGaP nanowire	80 nm	$[\bar{1}\,1\,1]$ rotational twin EDX	4.2	[61]
W865a	InGaP nanowire	80 nm	$[\bar{1}\,1\,1]$ rotational twin HRTEM	4.2	[61]
W65a	InP-GaAs heterojunction nanowire	80 nm	NBED analysis	6.2	
W65b	InP-GaAs heterojunction nanowire	80 nm	NBED analysis	6.2	
W65c	InP-GaAs heterojunction nanowire	80 nm	NBED analysis	6.2	

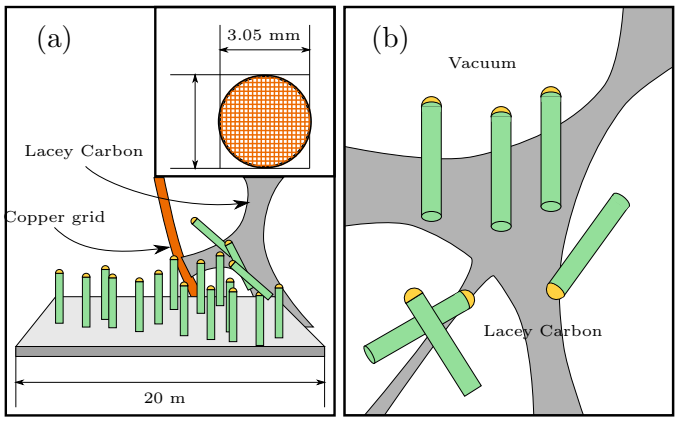

Figure 3.1: Scraping wires of a substrate and onto a carbon coated Cu grid. (a) Schematic of carbon film scraping over a surface. The insert show a typical lacey carbon coated coper grid used for TEM. (b) Schematic showing the end result.

3.2 Harvesting of the nanowire forest

The most common way of preparing a TEM sample from a substrate with nanowires is certainly also the simplest. By merely rubbing a carbon coated TEM grid against the substrate wires will break off and some of them will end up on the grid. This procedure is illustrated in figure 3.1. This is easy and introduces very few defects in the wires. However, it is not possible to control the point where the wires would break and hence it is possible that all we see is the top part of the wires or even that some types of wires are not broken off at all [62].

3.3 Preparation of a single nanowire on a tip

Originally intended for tomography, the idea of placing nanowires on the very tip of a sharp needle was also deemed useful for the combined experiments of TEM and XRD as described in chapter 5. Several different approaches were tried with varying resulting quality. All of the methods used a FIB instrument, as described in chapter 2.4.4.

The first naïve approach was to lift out a section of the substrate using the much used lamella lift out approach as in [63]. The damage to the surrounding nanowires were large and damage could be seen up to 50 µm away from the drilled hole. A more thorough examination showed the damage to consist of two types of damage: redeposition and bending of the nanowires. The damage would occur even for low voltages and low currents, seemingly depending on the amount of milled away material or the total ion irradi-

ation. Micrographs from this experiment can be seen in figure 3.2. For a sample with limited tilt possibilities also a small bending of the nanowires would be detrimental to the characterization process. For the FIB used it was not practical to go to very low voltages, since the possible milling area would be reduced greatly.

The experiment was performed on an FEI Quanta 3D. The sample used was a piece from the sample made for the XRD-TEM experiment. This is a InP substrate with gold catalysed InP nanowires, ca 100 nm in diameter and 2-3 µm tall. The energies used were 30 kV and 15 kV, with the currents from 0.1 nA to 7 nA. For 15 kV the lowest usable current for the sought after geometry was 1 nA. The cut method used was the cross section trench (one side 90°, the other a 45° slope) often recommended for these situations in order to force the milled out material to flow in one direction. Cut sizes were 15 µm × 10 µm × 10 µm for 1 nA and higher currents, and 7 µm × 5 µm × 10 µm below 1 nA. The milling time was automatically calculated by the FIB software using the "InP milling" material choice. Even for the mildest doses, 30 kV 0.1 nA and 15 kV 1 nA the damage was equally sever. The only difference was that for currents higher than 3 nA the redeposition problem seemed more prominent.

3.3.1 Protecting the wires

At an early stage it was obvious that the FIB treatment was damaging the structures even at a distance. One solution would be to protect the wires using some layer that later could be removed. It was decided to try a polymer for protection. The polymer would need to be viscous, dry quickly and be vacuum safe and it must also be possible to remove thoroughly using a method that would not affect the nanowires. A polymer called crystal bond 509(Aremco Products, Inc. New York, USA) was chosen. The polymer was diluted with acetone and applied using spin coating, as suggested in the technical paper [64].

Whilst being a good candidate for vacuum purposes this glue turned out to not be stable under the electron beam beam. There were also concerns that the polymer layer by itself would be insufficient to protect the wires from the Ga-ions, as the Ga-polymer interaction is relatively small. The solution was applying a thin layer of Pt *ex-situ* using a sputter coater (Sputter Coater 208HR, Cressington Scientific Instruments Ltd. Watford, UK). The sputter coater was turned on for circa two seconds, which resulted in a thin but homogeneous layer of Pt. This thin layer helped against the charging but introduced its own problems as shown later.

The very first test sample using this protective layer followed a design based on the work by Cherns *et al.* [65], where pillars were milled out from a material to be used for tomography. This process required additional platinum to be deposited in the FIB, above the area of interest. A lamella was

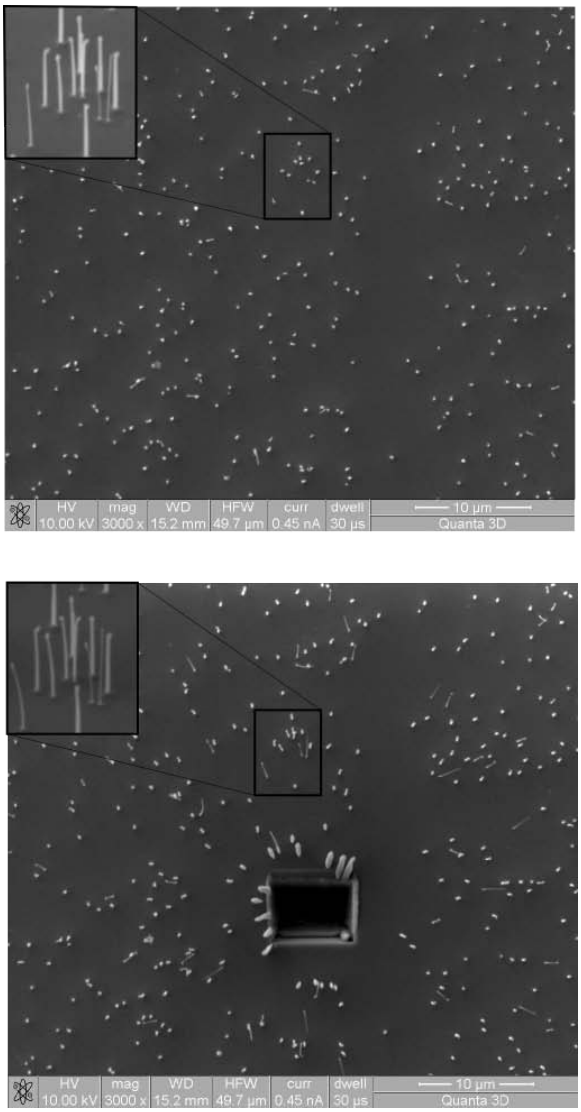

Figure 3.2: Even far from the irradiated area, nanowires are damaged by the ion beam. Both micrographs were acquired in 0° tilt angle and the bright dots are wires sticking up. The insets show the marked area at 52° tilt and double magnification. In this example the cut was done using 30 kV energy and 0.1 nA current and in such a way that the top part has a 90° cliff and the bottom a 45° slope. These settings are the most gentle feasible with the equipment at hand, and was expected to yield damage only below the cut in the image. The most obvious damage is the thick redeposition close to the milled hole, but more interesting is that wires several tens of microns away can be seen bending away from the beam also above the cut. The scalebar is 10 µm in both micrographs.

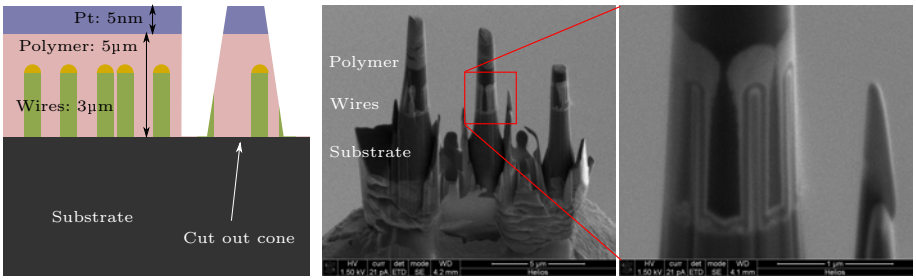

Figure 3.3: The first idea on how to prepare a sample for combined TEM and XRD measurements.

lifted out using the standard method [63], placed onto a tomography needle using a built-in Omniprobe micromanipulator, as described in section 2.4.4, and milled into three tower-like pillars as seen in figure 3.3. It turned out that there was too little material left of the substrate to align this sample for XRD, so this design had to be abandoned.

In order to get more substrate for the XRD and have the sample still being electron transparent for the TEM, a nanowire sample was specifically grown for this experiment. This sample, described in section 3.1 and mentioned above for the FIB damage experiment, had a low density of nanowires ($< 0.5\ \mu m^{-2}$) so that they would not shadow each other in transmission.

The sample was covered with the acetone thinned crystal bond and covered with a very thin layer of platinum *ex-situ*. A ten by ten micrometer large piece was lifted out as per the schematics in figure 3.4. The liftout was performed by first milling a 10 µm wide trench straight down into the substrate, 10 µm deep (8 kV, 0.66 nA). Since the polymer layer was around 5 µm this mean a depth into the substrate of about 5 µm. After this the resulting cube was cut from two sides at 38° (8 kV, 0.21 nA), the last cut whilst the sample was attached to the micromanipulator using FIB deposited Pt. Attaching the micromanipulator and removing it was done at 8 kV, 6.4 pA)

After attaching the cube to a beryllium:copper-alloy tomography needle, the polymer was removed. Several times this was tried by submersion into a solvent (Acetone), however the FIB-deposited platinum was not enough to keep the sample during the submersion. The sample kept breaking off from the needle. On possible explanation is a possible bad homogeneity of the deposited Pt, leading to structural weakness [66] such that the surface tensions would be enough to remove the sample.

Instead the polymer was removed using plasma etching *ex-situ* in a Fishione model 1020 (E.A. Fischione Instruments Inc., Export, PA, USA). The sample was checked every 30 minutes. Between the 120 minute and the 180 minute mark no further material removal was be found to occur and the process was halted.

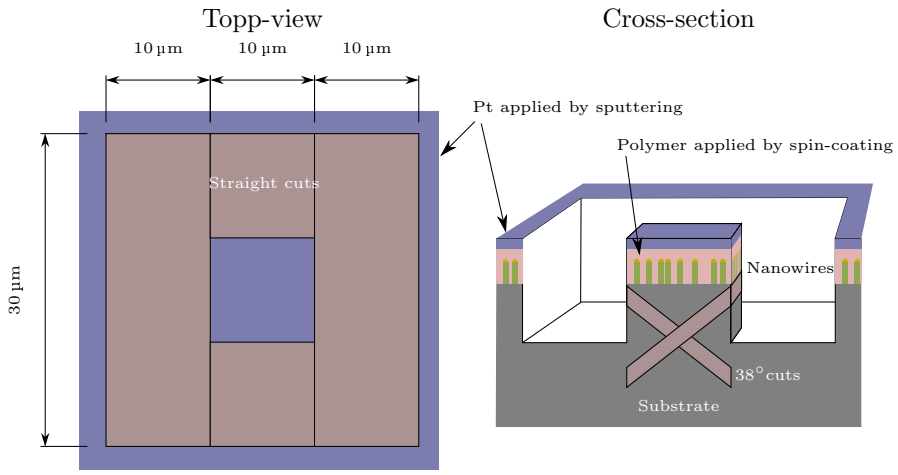

Figure 3.4: A new liftout design, lifting out a ten by ten micrometer large substrate with nanowires protected by a polymer.

Unfortunately, as can be seen in figure 3.5, the nanowires of the resulting sample were all disfigured. It is not yet clear what step of the sample preparation method that led to this. Speculations include strain in the polymer during liftout or nanowire bending during ion irradiation as in the case of unprotected wires above. This effect was not found on a dummy sample that was treated with polymer and plasma cleaning, but no ion beam. This indicate that the plasma cleaning of the sample could be ruled out as a reason and so can the polymer application and hardening process.

3.3.2 Liftout with minimized milling

In order to circumvent the problem with the bent wires a third approach was tried, see schematic in figure 3.6. The InP substrate is very thin and fragile and is easy to cleave. By cleaving of tiny pieces under a light microscope, some would be small enough to put onto a tomography needle. In the edges wires would also be alone over a large cross sectional area and be observable in the TEM. This method would expose the wires to a minimum of stress and a minimum of Ga ions.

Samples produced using this method had unfortunately not been used in XRD experiments when this report was submitted.

3.4 Nanowire/Substrate cross section

Using a standard TEM sample preparation technique it was possible to make samples for studying the nanowire/growth substrate interface. A combination of grinding and argon ion milling was used to thin the sample in the

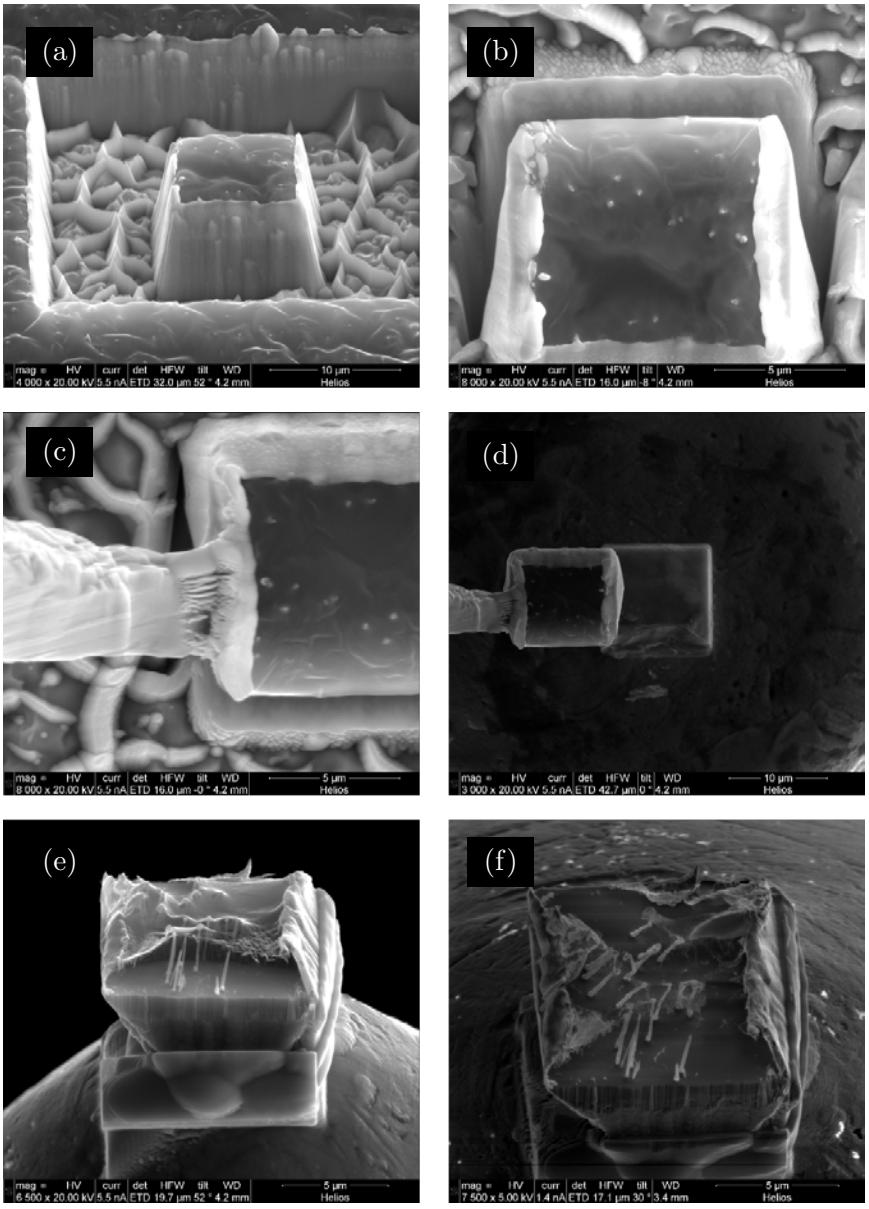

Figure 3.5: The results from the liftout design in figure 3.4. (a) and (b) are the cuts as seen in 3.4. In (c) and (d) the block is lifted out using the micromanipulator and attached to the beryllium:copper needle. (e) show the sample after 60 minutes and (f) after 90 minutes of plasma cleaning – the wires turned out to be severely bent.

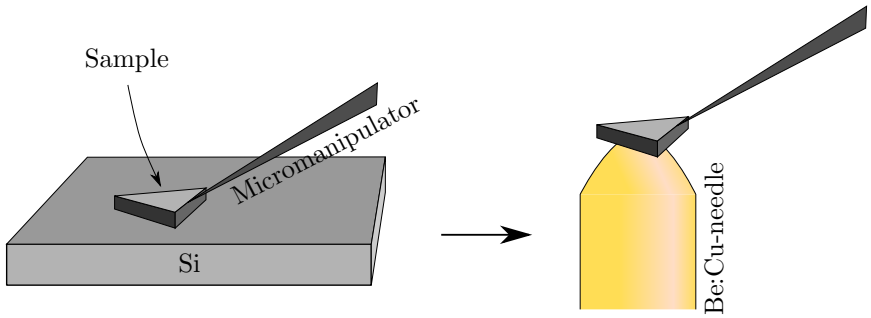

Figure 3.6: A third liftout design. The sample is cleaved under a light microscope. Pieces with a favourable shape and size are chosen and placed loosely on a silicon wafer in the FIB. The ion beam is used only for attaching the piece to the Omniprobe micromanipulator and the subsequent attaching of the piece to the needle and removal of the micromanipulator from the piece.

area where the nanowires come out of the substrate. The method has been described for other types of samples [3]. It was suggested by Gustafsson et al for use in the case of nanowires [62], and have successfully been deployed by other groups, e.g. Taraci *et al.* [43]. The method was used primarily for acquiring chemical information or determining strain in the interface, see sections 4.3 and 6.3.1.

The sample was cut, covered in a polymer and sandwiched between similarly cut Si-Wafer pieces, see figure 3.7. Two polymers were tested, the M-bond 610 (Vishay Precision Group, Inc, Raleigh, NC, USA) and the G1 (Epoxy Technologies, Billerica, MA, USA). The difference mainly being post-hardening mechanical stability it was decided to use the M-bond 610 polymer since the application process is much easier.

The sample was polished on one side and glued to a molybdenum washer. Molebdynum was chosen over Copper because of the benefits it has when doing chemical analysis using X-ray spectroscopy [3]. The other side was then polished until the Si was transparent red. This is a sign of the sample being below five µm thick [67]. Further thinning was done in an argon ion milling system Fischione model 1010 (E.A. Fischione Instruments, ltd., Export, PA, USA) in a rocking cradle at 6-12° angle.

A typical example figure was presented already in section 1.2, figure 1.2(b).

As samples for use in the TEM need to be thin enough to be electron transparent the process of ion milling is not stopped until a hole can be seen in the center of the sample. This guarantees that the sample is thin enough in the vicinity of the whole. For the nanowire samples it is however important also not to get a too thin sample since this might cleave the wires or make them very scarce along the line of polymers, especially for a low

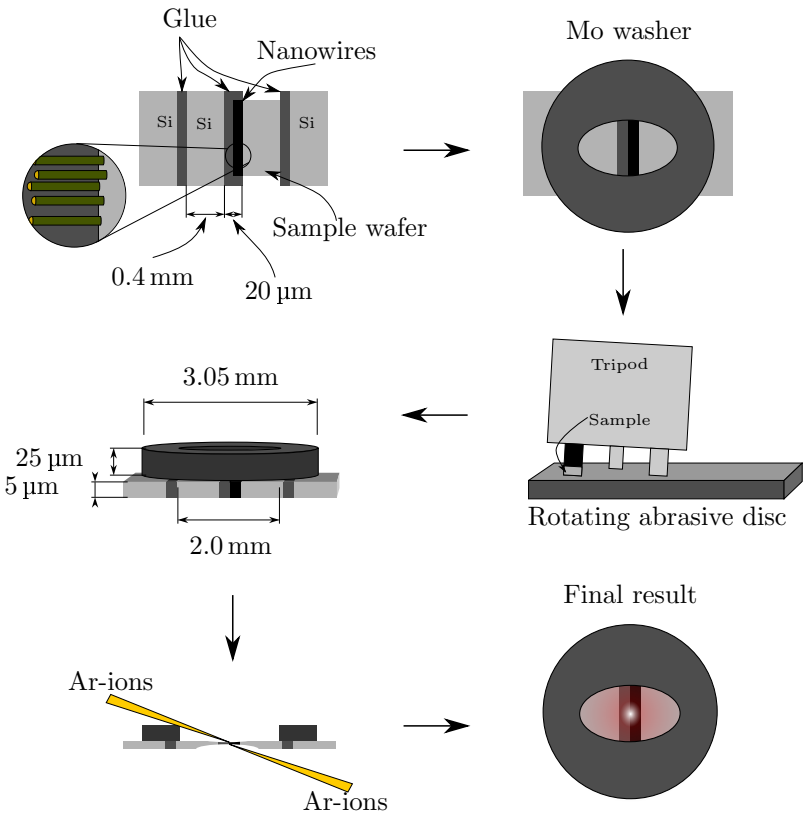

Figure 3.7: Schematic describing the cross-section method. After gluing the sample toghether, the sample is thinned down and polished. Once the silicon pieces are thin enough to transmit red light, the sample is transferred to the argon ion miller for further thinning in the centre. This continues until a small hole has appeared in the very centre.

density sample. Because of this a low angle on the ion miller is appropriate.

A sample like this was also used for the comparative study of TEM and XRD in chapter 5. Using a tiny amount of silver glue the sample was attached to the tip of a TEM tomography needle for use in the synchrotron. For examination in the TEM it was simply removed from the needle using a very careful scraping with a scalpel. When removed it was possible to image it using a regular dual tilt TEM holder. Originally samples were to be made using the method in section 3.3. This, however requires a single tilt tomography holder. For some applications where the *in-situ* two-directional tilt is required this cross-section might actually be a prefered choice.

Chapter 4

Uncovering several peculiarities of epitaxially grown nanowires

Throughout the work with this thesis several interesting features have been uncovered in the samples used. Whilst a full investigation of these were outside the scope of this work, it it is nonetheless experiments of interest for the community and will therefore be discussed, if not in detail. All of the following would be worth looking into in more detail since mentions of them in the literature are sparse.

4.1 An unusual shape of Au catalyst particle

Au nanoparticles used for catalysing the growth of nanowires as per section 2.3.2 are normally seen as growing the nanowire layer by layer yielding a flat bottom of the Au particle [68]. There are examples in the litterature of Au particles with uneven sides and surface faceting [69, 70]. Throughout this work it has become obvious that there is a third possibility, at least in the very end stage of the growth process. The nanowires seen in figure 4.1 are InP-GaAs nanowires and in figure 4.2 a GaP nanowire. For these systems the Au particle frequently was found sporting a droplet like feature underneath the Au particle, most obvious when using ADF STEM.

This feature of the Au particle was analysed using HAADF STEM (figures 4.1(a) and 4.2) and EDX spectroscopy (figure 4.1(c)), as well as tomographic reconstruction of the morphology (figure 4.1(b)). The perturbation of the Au particle into the wire (henceforth called the "Au droplet") indicates a critical change in parameters during the last part of the growth. In figure 4.1(c), GaAsP forms a characteristic neck region of the wire [26]. The Au droplet does not reach all the way down to the GaAs but stop in the GaAsP layer.For thinner wires such as the one used in the EDX in fig-

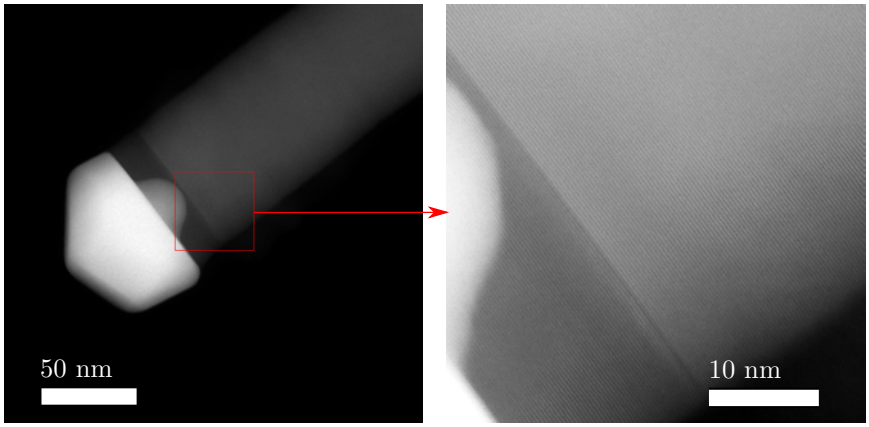

(a) HRSTEM of Au particle of an 80 nm thick GaAs-InP wire.

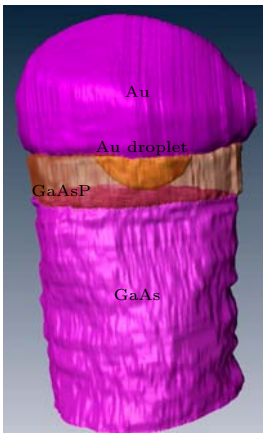

(b) Tomographic reconstruction. A video of this is available at [71].

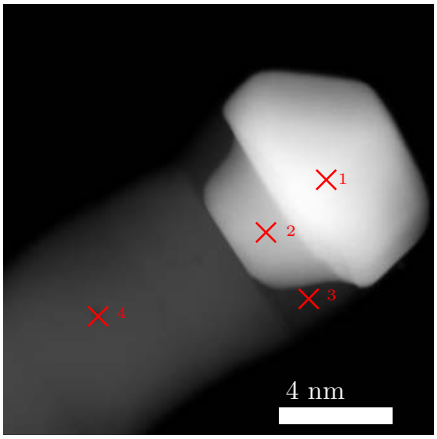

(c) A 10 nm thick GaAs-InP wire. At the positions of the numbered points EDS spectra were acquired, see results below.

	P	Ga	As	In	Au
1	5.38	3.54	0.00	1.81	89.25
2	18.74	18.45	4.47	0.89	57.42
3	33.03	54.88	12.08	0.00	0.00
4	0.00	46.93	53.06	0.00	0.00

(d) EDS results, relative composition, at%

Figure 4.1: For a certain set of growth parameters, the Au particle does not keep its bottom flat, but rather form a Au droplet hanging down underneath.

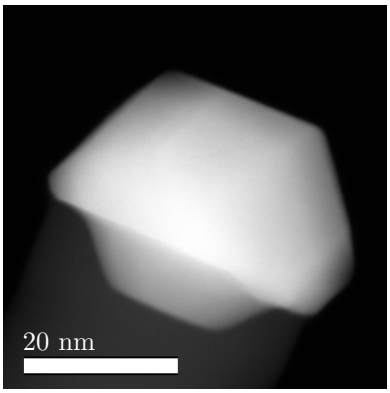

Figure 4.2: HAADF STEM of Au particle in a 40 nm thick GaP wire, with no obvious neck region.

ure 4.1(c) the Au droplet is in contact with the GaAs area. This wire is actually a heterojunction wire with the lower region grown as InP and the top part GaAs. It is plausible that some phosphorus stay in the Au particle at it's saturation limit after the precursor gas has been turned off. When the temperature decrease the saturation limit of the Au get lower and the P start to precipitate out. To the best of our knowledge this Au droplet has not been reported previously in the literature.

That the Au droplet also formed in the pure GaP nanowire shown in figure 4.2 indicates that this indeed is a temperature effect, rather than a material dependent effect. Two hypothesi have been formulated to explain the emergence of the droplet.

The first possibility is a dissolution in the late stages of the growth. A thermal difference could potentially be the cause of this, where the core of the wire would keep warm and dissolvable longer than the surrounding shell. Whilst this would work on a macro-scale the temperature gradients would be very small on the nanoscale, and even out quickly. Hence this is not a very plausible explanation.

The second explanation is that the rate of the growth in the end proceed quicker laterally than medially, i.e. the growth in height occur quick, with the nucleation center being in the three phase region (liquid Au – gaseous surroundings/vacuum – sold wire material) but growth within the layer is slow. As the Au particle run out of material the growth in both directions stop. That nucleation occurs preferentially at the three phase region is well known, see for example [68].

Previous studies of the Au particles have found that its shape is very important for the resulting quality of the grown wire. Joyce et al. in an article about optimizing parameters to get pure phases of Zb and Wz InAs nanowires [72], also present a nucleation model where the nucleus will start

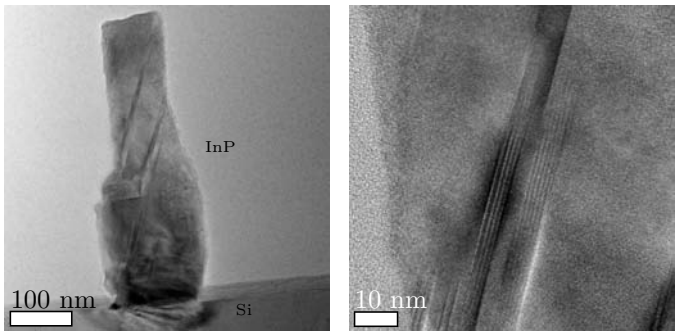

Figure 4.3: The (1 1 1) twin-defects were first encountered in these InP nanowires close to the substrate. Due to the general quality of the wire it was assumed not to be an issue in well behaving, straight wires.

at the three phase region and will influence the shape of the Au particle. They also calculate the energetically favourable conditions for different nucleation variants, pointing out that the growth temperature make a big difference. Similar discussions have also been done by e.g. Algra et al [73]. Since the temperature is indeed changed in the end of the growth process this is a plausible explanation.

Further examination of the Au droplet phonemenon is needed. The effects on electric properties are unknown, but it is easy to imagine this both as beneficial and as detrimental for a device using the nanowire. Perhaps the increased surface contact would give a more Ohmic connection between the Au and the rest of the wire. Or, alternatively, the sharp tip of the droplet might mean a thinner path and therefor increased resistance.

4.2 $(\bar{1}\,1\,1)$-twin defects diagonally to the growth direction, and the impact on chemical composition

One set of InP nanowires (figure 4.3) and a series of GaP nanowires (figure 4.4) were examined using HRTEM and HRSTEM and found to boast an unusual version of the (1 1 1)-plane twin defect common in Zb structure nanowires.

For Zb wires grown in the $\langle 1\,1\,1\rangle$-directions the (1 1 1)-plane twin defects are very common [74]. Every now and then a stacking fault make sure that atoms that normally would order in a ABCABC-type fashion instead order in ABCBA and in essence make one or a few layers of Wz. The wires examined so far show that the defect come in and even number such as the pair in figure 4.4(a) (red arrows) or more in figure 4.3. A similar effect has been noted in [75], where multiple consecutive twins were shown to lead to

a number of differently oriented kinks. There however the twin defects did not come in pairs.

The direction of the defect plane is in the diagonal of the wire – if the normal defects are {1 1 1}-planes these would be {$\bar{1}$ 1 1}-planes. As can be seen in the micrographs in figure 4.4 the standard {1 1 1}-defects are not present where the diagonal ones are. However, in the wires examined so far each set of ($\bar{1}$ 1 1)-defects always ended with a (1 1 1)-defect.

The defects in figure 4.3 seem to be started by a specific nucleation point – a small black spot believed to be Au in the bottom of the wire, and the edge of a shell-like structure for the defects starting halfway up. There are however no directly corresponding features in the micrographs in 4.4. For wires such as the GaP ones it was often found that one defect was followed by another, but never more than two. All of this combined make it very hard to pin down the possible reasons for this phenomena.

More research is indeed needed since these defects seem to influence the wire greatly. Figure 4.4(c) shows EDX data from a nanowire sporting these defects. This same data has previously been reported in [61]. Even tough the data is not exact – the phosphorus have a tendency to dissolve under the beam quicker than other material and hence give a too low number – the two points where the {$\bar{1}$ 1 1}-defects end show clear changes in the material composition towards higher Ga to In ratio. A change in composition might change the electrical properties of the nanowire as well as induce a change in lattice parameter that lead to a strain in the wire.

Similar diagonal twin defects has been seen before and presented in the literature [43, 76], however it has to the best of our knowledge never been discussed in detail in the literature.

4.3 Contamination layer on top of substrate during growth of GaP nanowires

Figure 4.5 depicts one particular use of the cross-section sample preparation method shown in section 3.4. This particular sample was shown to have a 150 nm thick two dimensional layer of material grown on top of the substrate. The sample was Au catalysed GaP nanowires grown on an InP substrate with a GaInP intermediate step. The layer was examined using TEM and STEM imaging and EDX. CBED was also investigated as a potential analysis method, however as can be seen in 6.3.1, this was not a fruitful experiment, due mainly to the sample thickness.

The sample had a few crawling nanowires along the surface as can be seen in figure 4.5(a), but most of the wires were standing fairly straight and looking stable. The thickness of the two-dimensional layer was varying somewhat throughout the sample and the interface between the original substrate and the surface layer seemed more abrupt in some areas than in

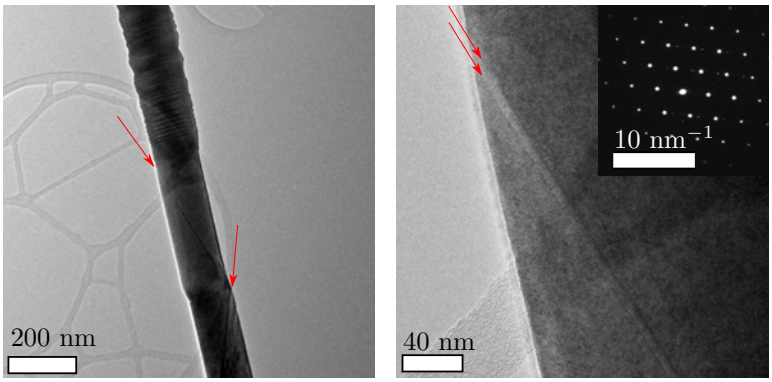

(a) HRTEM of an 80 nm thick InGaP nanowire viewed in a [1 1 0]-direction as seen by the diffraction pattern in the inset acquired close to the top of the defect. To the right is a higher magnification. The red arrows point to the endpoint of the diagonal twin defects.

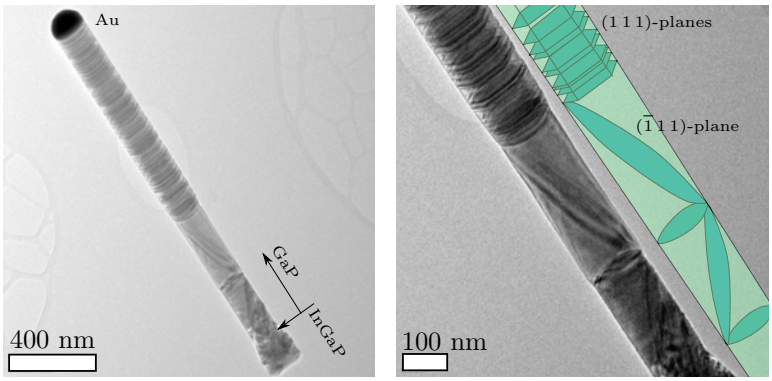

(b) TEM of a GaP nanowire with a InGaP base, shown at an angle. To the right is a micrograph acquired at a higher magnification. Next to it is a schematic to help the eye.

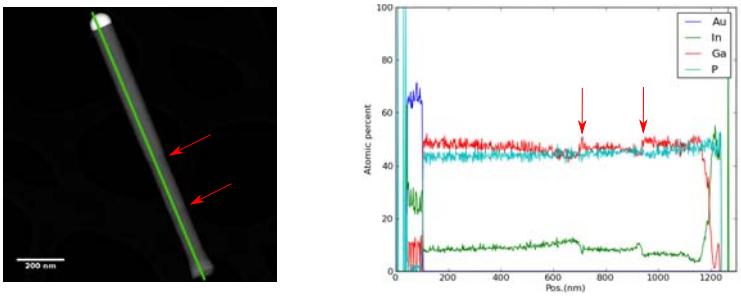

(c) EDX of a GaInP nanowire with two diagonal twin defects. The red arrows indicate the position of the ending of the defects and the corresponding position in the EDX line profile.

Figure 4.4: The (1 1 1) twin-defects have been most prevalent in GaP and InGaP nanowires. Especially in InGaP the defect seem to alter the growth conditions as evident from the EDX line profile above.

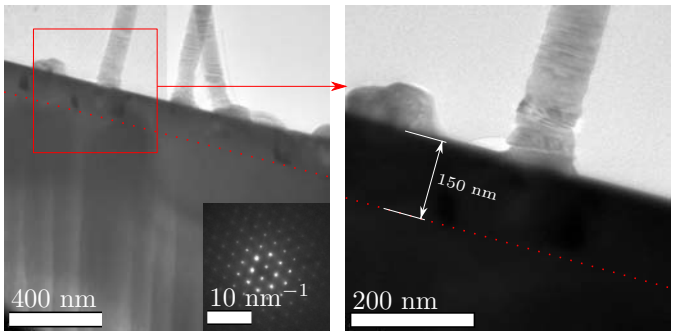

(a) TEM of the top part of a cross-section sample of GaP nanowires on a InP substrate in the [1 1 0] viewing direction. The inset shows a diffraction pattern from the substrate.

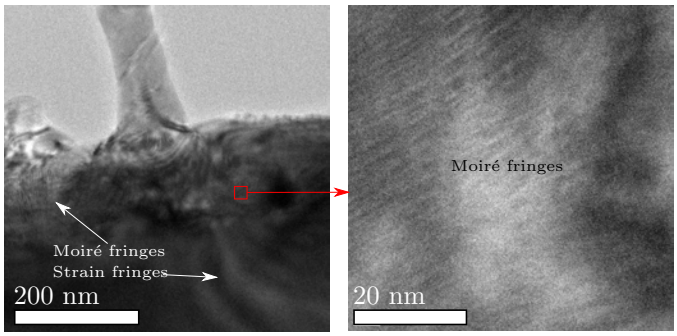

(b) HRTEM in the [1 1 4] viewing direction shows high amounts of moiré fringing in the top layer. It also shows what appears to be fringing due to strain.

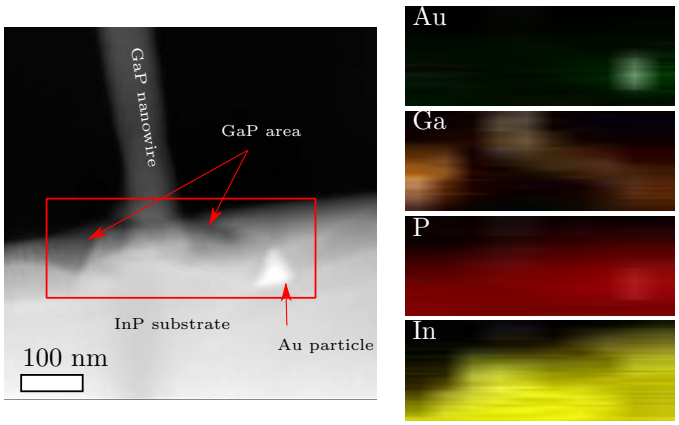

(c) EDX of the surface below the nanowire in the same sample as above shows the contamination to be a combination of Au particles and GaP overgrowth on the InP substrate.

Figure 4.5: The sample surface is covered in a 150 nm thick layer, hiding the original InP surface. This cross-section shows the properties of the layer. The base of the wires are actually inside the layer and there are several instances of noncatalysed Au nanoparticles below the surface.

others.

HRTEM showed the surface layer to be made of different crystallites, possibly with different lattice parameter. This was deduced from the moiré fringes in figure 4.5(b). EDX, figure 4.5(c), shows a growth of GaP on top of the InP layer. From this it seems reasonable to assume that the GaP from the nanowire growth either got incorporated into the InP substrate or made a layer on top. The position of the Au particles (dark spots in figure 4.5(a)) seems consistent with the latter hypothesis. Au particles that for some reason did not manage to start growing wires got buried under a layer of the grown material.

Boulanger and LaPierre [77] found similar layer growth for GaP grown on a Si substrate. The nanowire growth was facilitated by electron beam lithography (EBL) deposited Au particles, however the particles found on top of the wires were found to be substantially smaller in volume than the original. In a TEM examination of this sample they found that most of the Au was still at the substrate interface and that the substrate was embedded in a thick GaP layer. Many of their wires were also not growing in any preferred direction with regards to the substrate and multiple wires were grown from all Au deposit-sites. Boulanger and LaPierre correlates this unusual nanowire growth to a SiO capping layer formed on the Au particle at low temperature. They do not however, address the reason for the GaP layer growth. Since the substrate in our sample was InP and the wires were behaving like expected, an oxide layer forming on the Au particle is also an unlikely explanation.

A more thorough examination of this could be valuable in order to avoid this surface layer in the future. Whilst the cross-section sample preparation method is excellent for in depth analysis of the phenomenon it is too cumbersome to be used for regular screening of samples. This shows however that it can be useful in order to analyse these kinds of issues.

Chapter 5

Combining XRD and TEM measurements

Transmission electron microscopy (TEM) is great for acquiring data from small areas of a sample. Because of its small probe it is however not a good tool for analysis of a large amount of structures or to get the average properties of a bulk type sample, simply because this would take too long a time.

X-ray diffraction (XRD) on the other hand is excellent for finding the average structure from a large volume but is not normally known as a useful tool for analysis of small individual structures. However, with modern state-of-the-art equipment at synchrotron facilities, the focused spot of the X-ray beam can be less than 100 nm and in the record case even less than 10 nm [57]. Whilst this is still large compared to the electron beam in a TEM this development mean larger possibilities in the field of XRD.

Because of this these two methods often are used in conjunction, giving complementary information about the structures at hand. TEM for local information and XRD for an average over an ensemble of structures. It is not clear how comparable these methods are. Several studies have been attempted to find this, such as Morgan and Gilman [78] compairing TEM and XRD on polymer-layered silicate and Borchert et al. [79] whose study on determination of particle sizes showed that the size distribution results were in good agreement. These are however still measurements on similar areas and using different probesizes. To the best of our knowledge no one so far have reported any experiment probing the exact same nanosized feature using both methods. In this section the two methods are used on the very same nanowire sample to find out the relative tilt of the nanowire to the substrate. The difference in accuracy and the usefulness of the two methods are discussed.

This experiment was done as a collaboration between the Technical University of Denmark and Johannes Kepler Universität Linz, Austria [80], with

support from the people at the ID01 beamline for anomalous scattering, European Synchrotron Research Facility (ESRF), Grenoble [81].

5.1 Methods

For this experiment the same nanowire structures were examined using both TEM and XRD. Two goals were specified – to find a sample geometry that would allow comparative studies between XRD and TEM and to find and compare the reliability and compatibility of the measurements. Specifically the possible difference between large probe home-laboratory XRD equipments versus the tiny probe used in a TEM is not well explored. The experiment focused on measuring the relative tilt of the nanowire to the substrate since this is a simple measurement to analyse with both methods. Specifically the "on axis tilt" as defined in 5.1(a) was measured. The sample used is discussed below followed by the setup of the both methods and their respective limitations.

5.1.1 The sample

Originally the sample was meant to be a single wire on the tip of a tomography needle as described in section 3.3, but due to problems with the preparation method this was put on hold. Instead the sample used was CS49a, a cross section sample of InP nanowires grown on a Si (1 1 1) substrate. The cross section was made as described in section 3.4, but with a slightly harder than usual pressure applied when the sample was glued together with the Si spacer. The resulting sample had stable stems of broken nanowires still attached to the surface.

The hard pressure induced a tilt of all nanowires, in the same direction compared to the Si substrate. Most of the tilt should occur in the interface between the substrate and the wire. That the sample had broken of wires was deemed useful in order to ease the analysis process. Since the wires were embedded in a polymer with a mechanic pressure applied during the hardening a long wire could sustain a continuous tilt along the length of the wire. This would impede especially the XRD analysis due to the large size of the XRD-probe, averaging the measurement from a very large area. See figure 5.1(b) for a side-by-side comparison of the probe sizes used.

A STEM micrograph showing the sample can be seen in figure 5.2. In HAADF STEM a changed intensity is a sign of a change in material composition. As obvious from the micrographs there are features with a similar composition as the nanowires. These are believed to be either surface growth of InP nucleated by defects on the surface, or Au nucleated wires crawling along the surface. The magnified micrograph (HRTEM, to the right) shows that there is an epitaxial relationship between the substrate and this feature. Diffractograms were calculated using a fast Fourier transform (FFT)

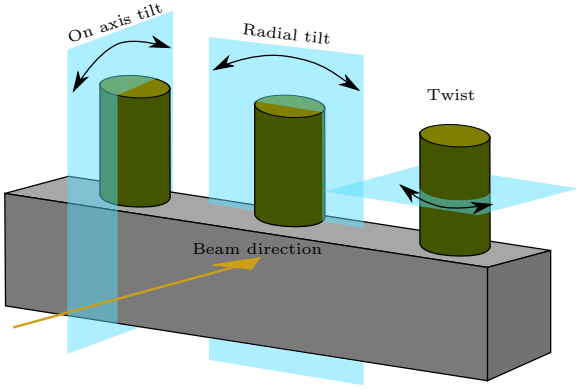

(a) Tilt directions.

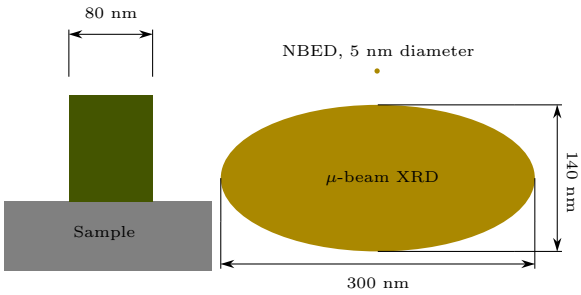

(b) Size comparison.

Figure 5.1: (a) Schematic representation of the tilts that will be discussed throughout this work. In this chapter the "on axis tilt" is the relevant one. In chapter 6 the others will be addressed. (b) Schematic representation comparing typical probe sizes with the size of the sample. Not included is the CBED-probe and the STEM diffraction probe, which are too small to be visible on this scale, and the probe of the typical home laboratory XRD setup, which is too large.

algorithm. These show the lattice spacing of this feature being larger than the lattice spacing of the Si substrate, which is consistent with this being InP.

Several nanowires on this sample were examined, both using XRD and HRTEM. For tilt measurement in TEM one wire was chosen and analysed.

5.1.2 The XRD experiment

The XRD measurement was performed at the European Synchrotron Research Facility (ESRF), Grenoble, France, at the ID01 beamline for anomalous scattering experiments. This beamline specializes on imaging and strain studies using coherent X-ray diffraction methods and on nanodiffraction. The setup after several monochromating and focusing steps give a very intense and coherent X-ray beam within an energy range of 3.2-24 keV. The energy used was 8.9 keV. The special zone plate type diffractive X-ray lenses used here developed during the works of Nöhammer [2] were capable of a focused beam size of 300×140 nm^2 but if needed the beam can also be used without these lenses giving a probe size in the order of some 100 µm. In the experiments laid out here the beam was focused as small as possible at the time, which was slightly larger than 300×140 nm^2 due to alignment issues.

The sample was placed in a custom made cradle in the centre of the goniometer in a geometry suitable for transmission measurements. A measurement of the slope of the transmission as the sample was moved in and out of the beam was used in order to align the sample with the thinnest (most focused) part of the beam. A similar transmission measurement was used in order to find the line of the transparent polymer in the center of the sample. Changing the setup to Bragg reflection measurements, it was possible to align further by finding the Si (1 1 1) Bragg reflection of the substrate. From this the theoretical angle of the InP reflections was calculated and the reciprocal space around this angle was mapped. The difference in position of the InP reflection from it's calculated position along the χ-axis as per figure 5.4 is a measure of the angle the nanowire is tilted in the radial direction. A difference in the 2θ-axis corresponds to a change in lattice parameter. A relative change along the rsy-axis would be indicative of an on axis tilt.

The mapping was done using a very sensitive, low noise CCD developed in house at ESRF (MAXIPIX, see [82]). First the whole CCD was used as a detector of the total intensity for different real space positions of the sample and later for imaging the reciprocal space diffraction pattern with every pixel element working as an individual detector. In the end of the session the size of the detector was calibrated to a known set of reflections and angles for the Si substrate. This calibration gave a measurement of degrees of tilt/reciprocal distance per pixel (channel) on the detector. Through this it is possible to convert the χ and the 2θ to tilt and reciprocal lattice spacings.

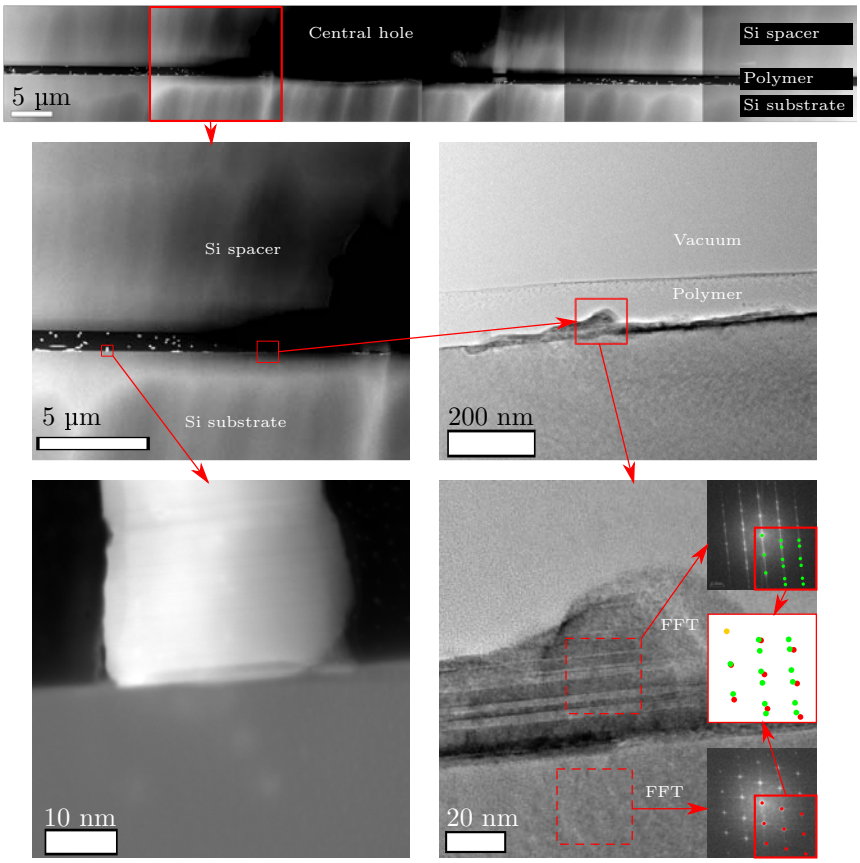

Figure 5.2: The sample CS49a was used for comparing TEM and XRD. The sample was chosen in part due to the wires being broken off in the preparation process, about 100 nm above the substrate. This ensured that most of any tilt that would be measured by the (bigger) XRD-probe would be from the region close to the interface between the wire and substrate. In the top the Si spacer can be seen, the centre is the "glue line" polymer filler, and in the bottom the Si substrate is shown with the brighter nanowires sticking up. Not all features on this sample was nanowires, as can be seen in the bottom right. Diffractograms from this BF HRTEM (insets) show that this structure is epitaxial to the substrate, but with a smaller lattice spacing. This structure has not been exposed to the same pressure as the wires and therefore has a lower amount of tilt. The FFTs show twinned and non-twinned Zb in the [1 1 0]-direction, cf. figure 2.8(e) to see the spots indexed in an equivalent diffraction pattern.

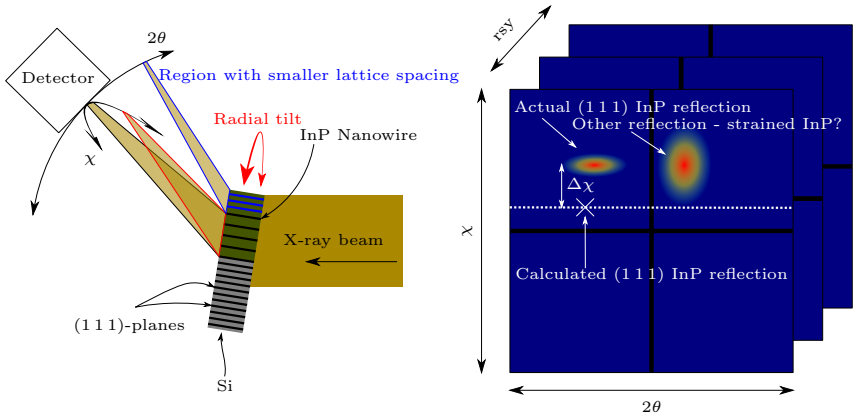

Figure 5.3: Reflections from the {1 1 1}-planes of the Si substrate was used for aligning the sample and the detector. From this the theoretical position of the (1 1 1) reflection for InP was calculated (white cross). The detector was then moved along 2θ to this theoretical position. The sample was scanned back and forth in order to obtain the sharpest reflections (rsy). In the diffraction image a change in χ (up/down) is proportional to a radial tilt of the (1 1 1)-planes as shown by the white arrow and beam in the schematic. A reflection changing position 2θ (right/left) will instead mean a change in lattice distance, exampled by the blue beam in the schematic.

From a comparison of the relative intensity of the peaks in the rsy-direction it would also be possible to get an idea of the tilt of the feature in the on-axis direction. The rsy value of the peak with the highest intensity was compared to that of the Si substrate. The difference is the on-axis tilt.

5.1.3 The TEM experiment

A probe C_S-corrected FEI Titan 80-300 was used for acquiring HAADF-STEM micrographs and STEM-mode diffraction patterns. The microscope was used at 300 kV and at an HAADF inner detector angle (IDA) of 57.0 mrad (camera length 128 mm). Diffraction patterns were acquired from five points along a line, with three points being on the nanowire, one in the substrate and one in the junction in between. The bottom part of the nanowire had been aligned to be in the [1 1 0] low-order zone-axis. The resulting diffraction patterns were analysed using simulated Kikuchi patterns from the JEMS software [83]. The tilt of the nanowire was found from the offset between the central beam and the center of the Laue zone circle, i.e. the node of the zone-axis. The distance along the (horizontal) 111 Kikuchi lines correspond to a twist as indicated in figure 5.1(a) and a distance along the perpendicular axis (the 242 Kikuchi lines) to a on-axis tilt. A radial tilt would correspond to a rotation of the diffraction pattern, as described further in section 6.1.

5.2 Results and discussion

The result from XRD on one of the measured wires can be seen in figure 5.4. By scanning the X-ray beam across a 5×5 µm large area of the sample the X-ray detector was used to acquire a micrograph of the diffracted beams. The analysis was done by locating the center of a feature in reciprocal space, i.e. the point of highest intensity in the 2θ, χ and rsy-directions. The $\Delta\chi$ was measured from the theoretical (1 1 1) Bragg spot position, as was the Δrsy. These distances are equivalent to a tilt of the sample in the radial tilt-direction and in the on-axis direction respectively.

The XRD measurement setup used here had a maximum angular view range of ca $\pm 1°$ in χ limited by the size of the CCD and the distance from the sample. While the center of the feature in the example was identifiable within $\pm 0.01°$, the accuracy was not that good. It is not limited by the experimental setup, but rather by the geometry of the wires and the position of the detector. The position of the Bragg diffraction peak was not always clear. This since the shape of the irradiated feature as well as internal structure can give rise to secondary diffraction conditions and more dispersed signals in the reciprocal space.

For two wires the measurements were especially clear. For one the radial tilt was 0.11° and for the other it was 0.09°. Other features were harder to measure accurately. The minimum radial tilt measured for any feature was -0.35° and the maximum was 0.21°. Some issues with streaking in the reciprocal space map were apparent, probably due to sample geometry.

The on-axis tilt was estimated to 0.78° since the highest intensity in the rsy direction could be found at this tilt. The angular view range for the on-axis tilt is only limited by ones patience since the data range easily could have been extended. From this session a range of 0.8° was chosen. A simple line measurement was done first in order to get to the right ballpark.

The two peaks that can be seen in the bottom left in figure 5.4 show features with different (1 1 1) lattice distance. By comparing the $\Delta\theta$ for each to the calculated InP peak position, and using the calibration measurements, the lattice distance to each was calculated. The calculated peak (Zb InP(1 1 1)) corresponds to a lattice distance of 3.388 Å, the closest peak to 3.393 Å and the one furthest away to 3.425 Å. This difference of one percent could well be due to a local strain close to the Si surface, or the signal could come from the crawlers in figure 5.2.

Figure 5.5 shows the results from the measurement that was done across one nanowire using TEM. The distance between the direct beam, marked with a blue spot, and the center of the Laue zone circle, marked with a green spot, gives the tilt angle. The stage was aligned such that the bottom of the nanowire should be straight on the [1 1 0] low order zone axis. The simulations show that the on-axis tilt away from the zone axis is -3.20° in the substrate, go through 0 and tilts 1.00° in the other direction in the nanowire.

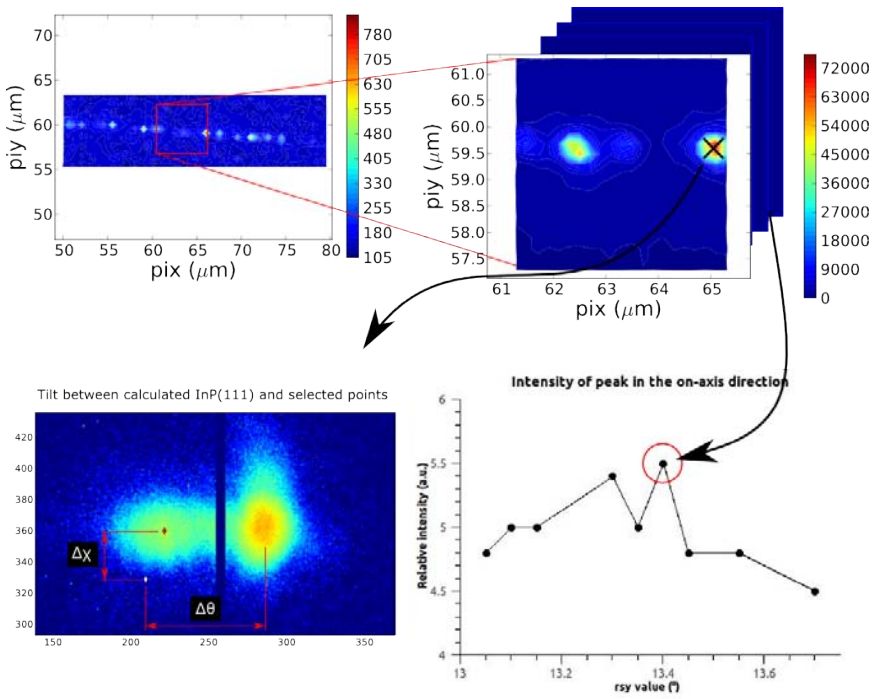

Figure 5.4: A large scan with low resolution showed where features with reflections in the area of the theoretically calculated InP (1 1 1) were. A smaller area was defined for which 15×30 points were irradiated while the CCD acquired a full frame of the reciprocal space. A plot of the total intensities of these frames (top right) shows where the features are. One example frame marked with a cross can be seen in the bottom left of the figure. The lattice distance for both peaks that can be seen here was calculated from the difference in $\Delta\theta$. The bottom right shows a graph of the relative intensity in one peak for different rsy values.

The total tilt difference is 4.2°. In the twist direction the tilt is much smaller, but still varying around 0.92°. The major part of this is in the interface. The difference between the maxumum of the wire and the substrate was 0.42°. The accuracy of these measurements were lower than those of the XRD. For this camera length a realistic estimate of the accuracy would be ca ±0.05 °, based on the possibility of accurately positioning the simulated Kikuchi pattern.

The discrepancy between the numbers for XRD and TEM measurement is large. The fact that this XRD measurement maximally measured ±0.4° tilt in the on-axis direction while the nanowire analysed using TEM showed a 4.2° tilt shows another reason to use these methods as complementary methods; Several of the nanowires that were tilted too much from the substrate will have been invisible in the reflection measurement performed using XRD.

The TEM data acquired was unfortunately not the kind needed for analysis of the local lattice distance variations, but that could be done in future experiments. It was also not possible to analyse the very small amounts of tilt in the radial tilt direction, due to the quality of the measurement.

5.3 Conclusions and future outlook

Properties of devices based on III-V nanowires are highly dependent on the exact crystallography and the epitaxial relationship between the individual components. Any change during post treatment or in the growth process may result in deviations from the sought after behaviour. In order to map such small deviations for quality control of the devices both TEM and XRD have been used. As both methods have strengths and weaknesses it's beneficial to see them as complementary techniques – ideally on the very same sample.

The work performed comparing XRD and TEM shows that there are several ways in which the methods can be used to complement each other. We have successfully measured the tilt of several features of the very same sample, showing that this sample preparation method and sample geometry work for comparative studies.

Two features were measured using XRD. These showed radial tilts of 0.09° and 0.11° respectively. Other features that were harder to measure exactly show tilts up to 0.21 and down to -0.35° from the [1 1 0] zone axis. For the on-axis tilt-direction, the feature analysed with XRD showed a 0.78° tilt.

For comparison one wire of the same sample was measured using TEM. There was a maximal twist-direction tilt difference of 0.92°, but most of this was in the interfacial area. The TEM data show a very large tilt difference of 4.2° between wire and substrate. The very local information from the TEM is of course both a blessing and a curse. The data from the different areas

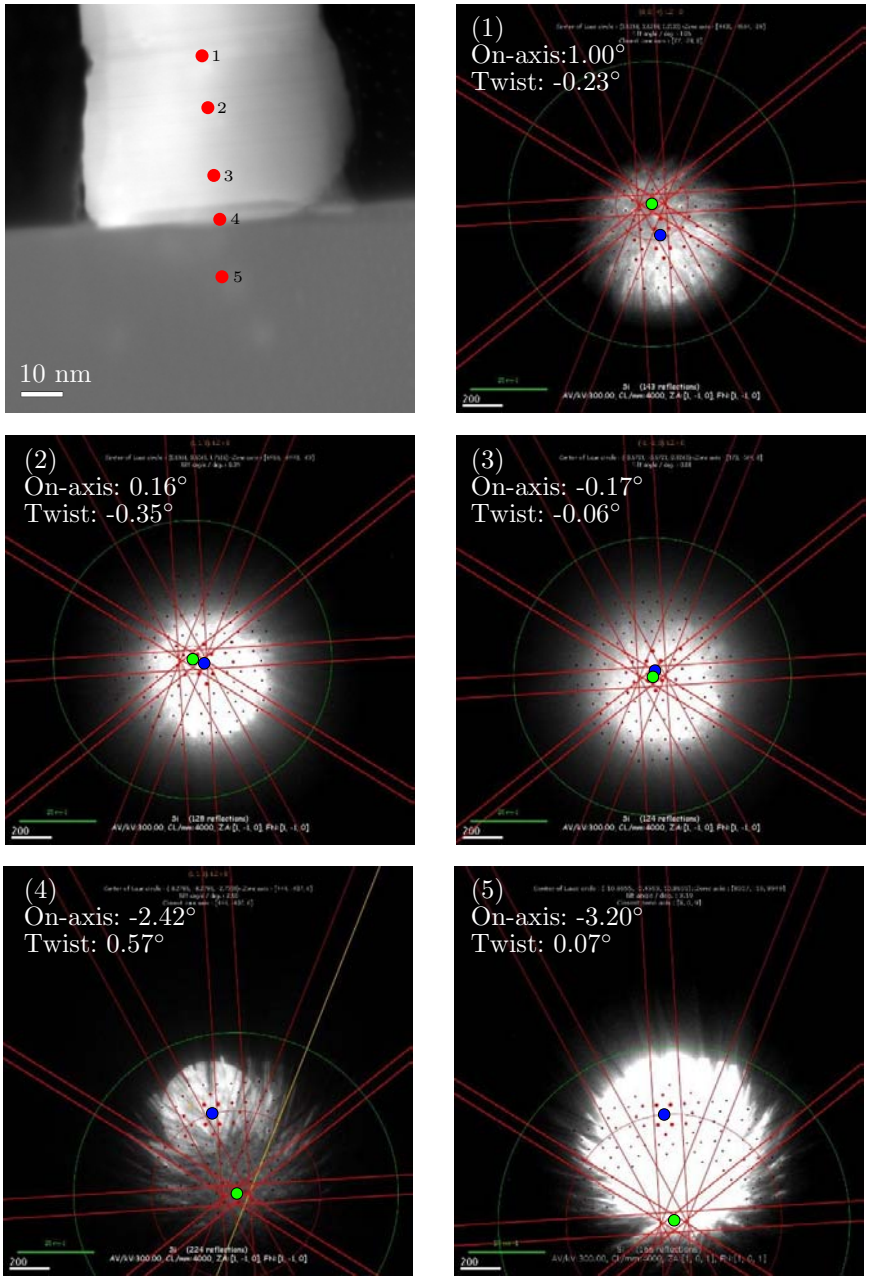

Figure 5.5: These numbered STEM-diffraction patterns were acquired from the corresponding points in the HAADF STEM image (top left). They were then used to measure the tilt of the wire with regards to the substrate. The offset of the position of the Laue zone circle from the central beam of the diffraction pattern can be translated into a tilt of the nanowire or the local lattice probed by the beam.

are very different and finding a reliable average would take a lot of work. The large probe of XRD does this instantly.

Further studies of the TEM data showed the appearance of smaller features on the sample surface that would indeed not be showing the same induced tilt as the longer wires. These features are believed to be either self-catalysed InP or gold catalysed wires growing along the surface. HRTEM proved these features and the substrate to be epitaxial to each other. Since the tilt in the on-axis direction differs so much between TEM and XRD it is possible that the XRD measurement caught one of these instead of a wire.

To the best of our knowledge this is the first report about experiments examining the exact same feature using a TEM and a nanobeam XRD setup. Other work comparing XRD and TEM have been performed on ensembles, e.g. [79] in which the size determination of monodisperse $CoPt_3$ nanoparticles using TEM and XRD was compared.

Future work should take the limited angular field of view of XRD into account when trying to find measurements from the exact same wire. Tilt was the chosen feature since it is simple to measure and analyse using both methods. Future experiments could include lattice parameter estimates, comparing nano beam electron diffraction and XRD, and estimates about the number of defects in a nanowire.

Chapter 6

Nanobeam electron diffraction probing of local crystallographic variations in nanowire systems

Crystalline matter change its properties due to local effects such as strain or local variations in the lattice. For devices made with larger structures a small variation is often less detrimental because of averaging effects. For nanometer sized structures such as nanowires the structure needs to be much more exact.

Nanowires are prone to several different property changing effects such as changes in composition, bending, skewing and twisting. These can be both local and global. For example, a heterojunction is often built into the wire in order to achieve a sought after bandstucture for certain electric properties. As in the example used here with wires going from InP to GaAs, the crystal structure changes from Wz to Zb and this change is large enough to be visible as a change in morphology in an SEM. A small change in composition where the material has a different lattice constant will give raise to a local strain changing the lattice locally.

Bending and twisting of nanowires are common results from both the growth process and from further processing – nanowires are very elastic [84, 85]. Bending at growth is most often in the form of sudden kinking where the wire bends of in a crystallographically preferred direction, however, thinner nanowires are easier tho bend to an external force. Bending can result in changed electronic properties and change the dimensions of the nanowire. This can be crucial for any device being made with nanowires.

To analyse these effects several methods are available. This work has been focused on using nanobeam electron diffraction (NBED), combining good accuracy with high spatial resolution.

6.1 Methods

Nanobeam electron diffraction (NBED) is a technique where a convergent beam of electrons are made as parallel as possible, or in other words - the convergence angle is made as small as possible. As in a selective area diffraction (SAD) pattern the position of the diffraction discs can be precisely determined. The area selected by SAD is limited by the size of the aperture and machine properties such as C_s to about 1µm [3]. In comparison the probe size of NBED has been reported to be as small as 2.7 nm [86] but would normally be around 5 nm [50]. Convergent beam electron diffraction (CBED) which will be discussed briefly in section 6.3.1 uses an even smaller probe but is harder to analyse and requires a thick sample.

All NBED experiments in this chapter were performed on a FEI Titan 80-300 Analytical, with an HAADF detector IDA of 37.4 mrad (camera length of 192 mm). The mode used was microprobe STEM and the microscope claimed a convergence angle of 0.34 mrad. The actual convergence angle was estimated from the acquired NBED patterns to be 0.9 mrad, using the known proportional relationship between the convergence angle 2α and the size of the disks, and between the distance on the screen and the Bragg angle 2θ, see 6.1(a).

The size of the probe was examined through a scan across a nanowire with a number of twin defects, see figure 6.1(b). In Zb the diffraction pattern is mirrored when going from one twin to another. The smallest scan pitch used was 5 nm. For this pitch the smallest area to clearly show two undisturbed patterns was a 10.8 nm long section. This shows that the probe was < 5.4 nm.

NBED was here used to measure three things: the distance between the atom planes, the twisting of the wire or local lattice and the bending of the wire or the local lattice. A schematic can be seen in figure 6.2.

Distances between atom planes bending is directly deducible from measuring the position of the discs in the diffraction pattern. The twisting can be measured by finding the displacement of the center of the Laue circle to the direct beam. Finding this displacement can be tricky and it is often necessary to simulate a spot diffraction pattern or a Kikuchi band pattern to ease this process. More on the formation of Kikuchi bands and NBED patterns in the background chapter, section 2.4.5.

There are several possible sources of errors for the NBED diffraction measurements. One is of course the machine dependent errors stemming from bad alignments. Internally consistent sets of measurements that fit well with data from the literature have here been regarded as accurate.

Another source of errors is the risk of inaccurate measurements of the centre of the diffraction discs. For the data presented here the worst case scenario would be a faulty centre definition of circa three pixels, giving the distance between two discs a possible maximum error of six pixels. For

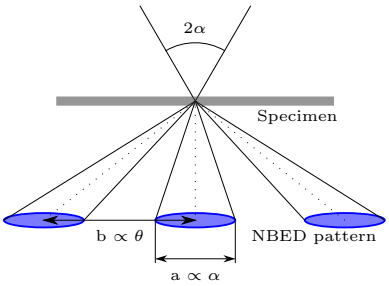

(a) Estimating the convergence angle, cf. [3, p. 83].

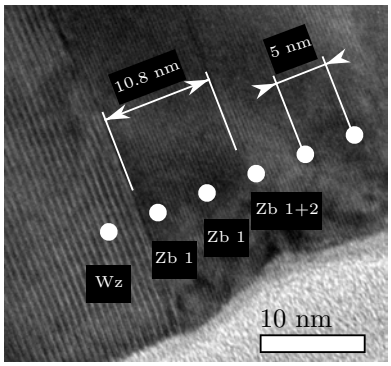

(b) Estimating the probesize.

Figure 6.1: The contact angle was calculated from its relationship to the NBED spots, $2\alpha = 2\theta_B \frac{a}{b}$.The probe size was estimated by looking at how small areas could be resolved. For two points the crystal structure was clearly one of the Zb twins (Zb 1). For the next it was a mixture of both twins (Zb 1+2). The area with the first twin was 10.8 nm long and the pitch between the measurement points was 5 nm. Due to sample drift the marked spots cannot be trusted to relay the exact position. Even so, we can conclude that the probe size should be smaller than 10.8/2=5.4 nm

increased accuracy the distance was measured over several disks and hence the error was averaged down.

All measurements were done using a commercially available software [87], where the patterns were first filtered using a Laplacian edge detection filter, followed by an approximation of each disc to a circle. The origin of these circles were recorded and from this the data was concluded. Other analysis methods have used the center of gravity of the disc, rather than the center of the disk, see e.g. [50]. There are today commercial software capable of doing this. For this work that level of accuracy was not deemed necessary.

Throughout this chapter all plots are presented in the direction of the linescan. It is generally good to be cautious concerning the exact position of last measurements points in each linescan due to sample drift and potential ranked up sample radiation damage along the way.

6.2 Results

Diffraction patterns such as those in figure 6.3 were acquired from several Au catalysed InP-GaAs nanowires using the method described above. The graphs in figure 6.4 show the measured lattice parameters extracted from

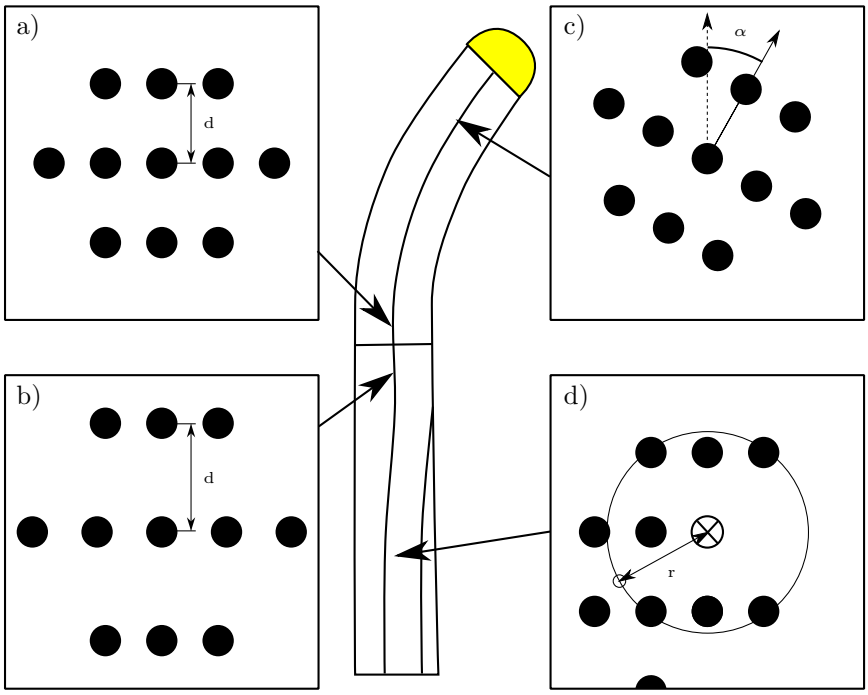

Figure 6.2: Data acquired from NBED diffraction patterns can be interpreted at both an atomic level (local) and a larger scale (global). Nanowires b) changing composition, c) bending and d) twisting all give rise to a change of the diffraction pattern as compared to a) an area which we assume to be unstrained.

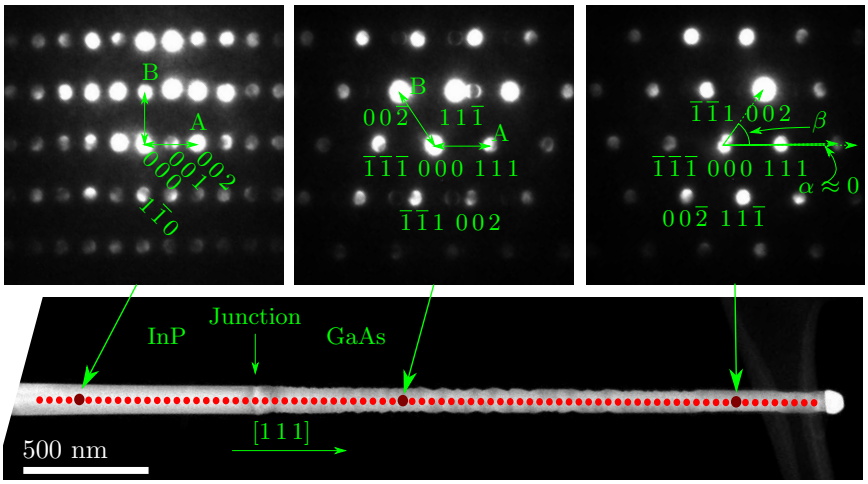

Figure 6.3: Eighty NBED patterns were acquired over the length of a wire (W65a). In the three examples above the reflections have been indexed and the relevant distances and angles have been defined. The part of the nanowire to the left is InP and has a Wz structure and the right part is GaAs showing a Zb structure. To the far right the nanowire is capped by the Au catalyst particle used for growth. The nanowire was grown in the [1 1 1]-direction. The diffraction patterns have been rotated slightly in order to be aligned with the direction of the nanowire.

the NBED patterns of nanowire W65a[1]. The top graph shows the distance between certain planes in the crystal and the lower graph shows the rotation from the growth direction [1 1 1]. This measurement extended over almost the full length of the nanowire and was limited to 80 measurement points, one every 25 nm.

The most obvious change seen is that from the Wz crystal structure in the InP to the Zb structure in GaAs. The angle β changes from a 90° angle to a 55/110° angle. The GaAs part has several stacking faults in form of twin defects which appear as a rotation of the diffraction pattern, leading to the two different measured values of β. In GaAs another interesting result can be seen for the rotation measurement. The angle β seems to first be shrinking and after this it is slowly raising along the wire. This behaviour is not yet fully understood, but seem to be an actual local change of the lattice. The α direction is not changing however, which indicates that this is a skewing of the lattice rather than a bending of the wire itself.

Since the distance between the lattice plains should be constant in a certain material any deviation is a sign of a strain or compositional change. The measurement shows a constant lattice plane distance for both the InP and the GaAs parts of the wire. The big change is a change in the junction

[1]For a description of the samples used, see section 3.1

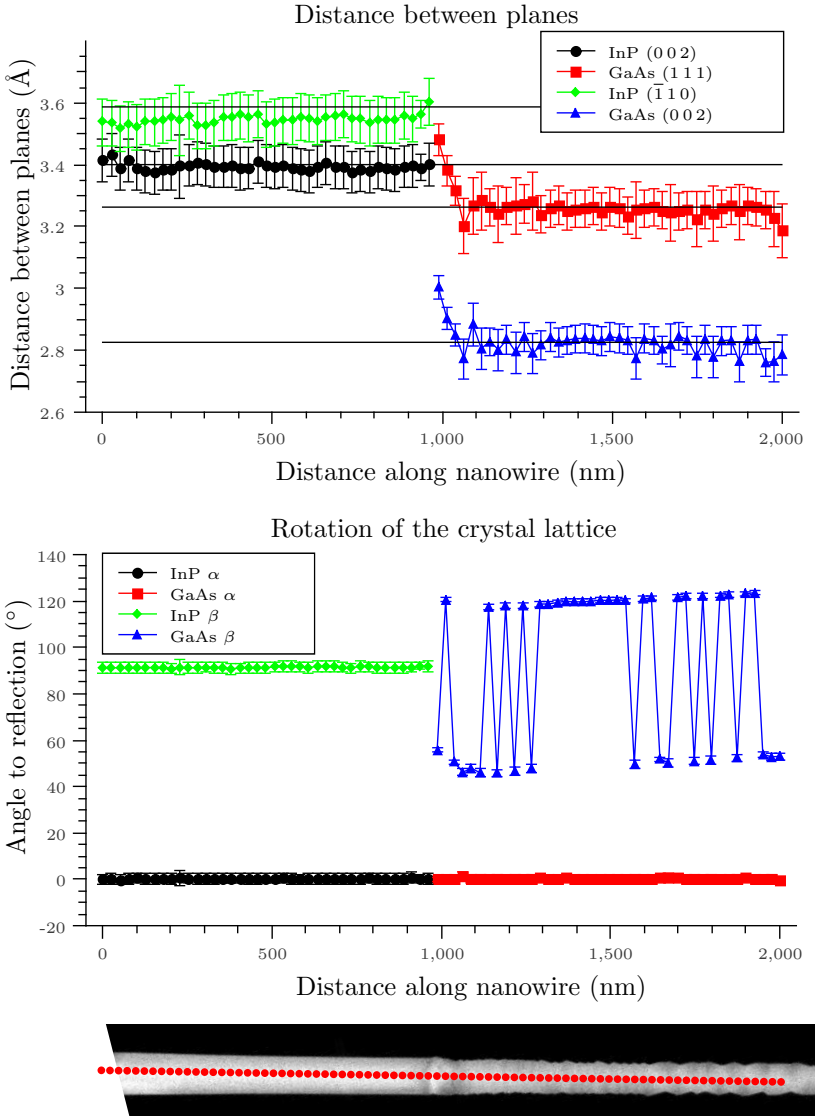

Figure 6.4: Wire W65a shows a sharp change from Wz in the InP to Zb in the GaAs as the rotation measurement change from 90° difference to 55/125°. The measurement of the distance to the reflections, translated into a distance between the planes in the lattice, show a slope between the two materials. The horizontal lines correspond to lattice distances given in the literature [24], [88]. The HAADF STEM micrograph in the bottom is scaled to the graphs, and each red dot corresponds to one of the measurement points.

between InP to GaAs. There is also a fluttering of the distance between the (0 0 2)-planes in the GaAs. This seems to correspond to the change of direction in the rotation. This indicates a slight misalignment of the microscope.

A measurement of W65a with a higher sampling frequency of sixty measurement points - one every five nm, can be seen in figure 6.5. This measurement was performed across the junction and it clearly shows the slope of the strain and the immediate change of crystal structure. Some measurement points are missing due to too dense defects making accurate measurements tricky. This measurement shows the change from one unit cell size to another to occur over ca 80 nm.

An EDX measurement of a different nanowire from the same batch, W65b, show the transition from InP to GaAs to pass through a stage of InPAs and then InGaAs before stabilizing at GaAs, figure 6.6. This is not surprising since group III elements are exchanged quickly [89], whilst group V elements tend to take longer to switch [90]. The transition in this wire is completed after ca 30 nm. The HAADF STEM contrast is brighter for this part of the wire, consistent with the difference in material composition. Since the TEM contrast in W65a is comparable in width with W65b these are likely to be similar in composition. But as pointed out previously the change in lattice parameters occur over 80 nm. The gradual slope of the lattice distance difference can hence not be fully explained with a slow change in material composition but has to come from a gradual relaxation of the lattice. This observation effectively impugn the naïve idea to use composition data to derive strain and vice versa to use the lattice distance to derive composition via Vegards law as reported by e.g. Takeguchi et al. [91] and Gerthsen et al. [92] for TEM and our article (Jacobsson et al.) [61] for XRD – at least for smaller possibly strain-relaxed volumes.

A typical example of a situation where a nanowire shows much bending is the measurement of W65c – yet another wire from the same batch. The measurement of the rotation in the diffraction pattern can be seen in figure 6.7. It is not yet clear why this is, but the crystal lattice seem to bend outwards and later bend back to the original direction, the difference being almost 5°. One possible explanation is a number of defects locally out towards the edge of the wire in order to achieve a relaxed lattice in the middle. The measurement was done at the thinner part of the wire, close to the edge. The change in α is accompanied by a change in β showing that this is indeed a turn of the lattice, as opposed to a skewing.

Another interesting thing to measure using NBED data is the local twist of the wire – a rotation radially around its axis or on the axis. The result of such a measurement can be seen in figure 6.8. Again this is from the same batch but a new wire (W65d). This wire was chosen since it shows a larger than average twisting.

The graph shows the total twist of the nanowire as seen in each point with the biggest total difference being almost 4°. The analysis was performed

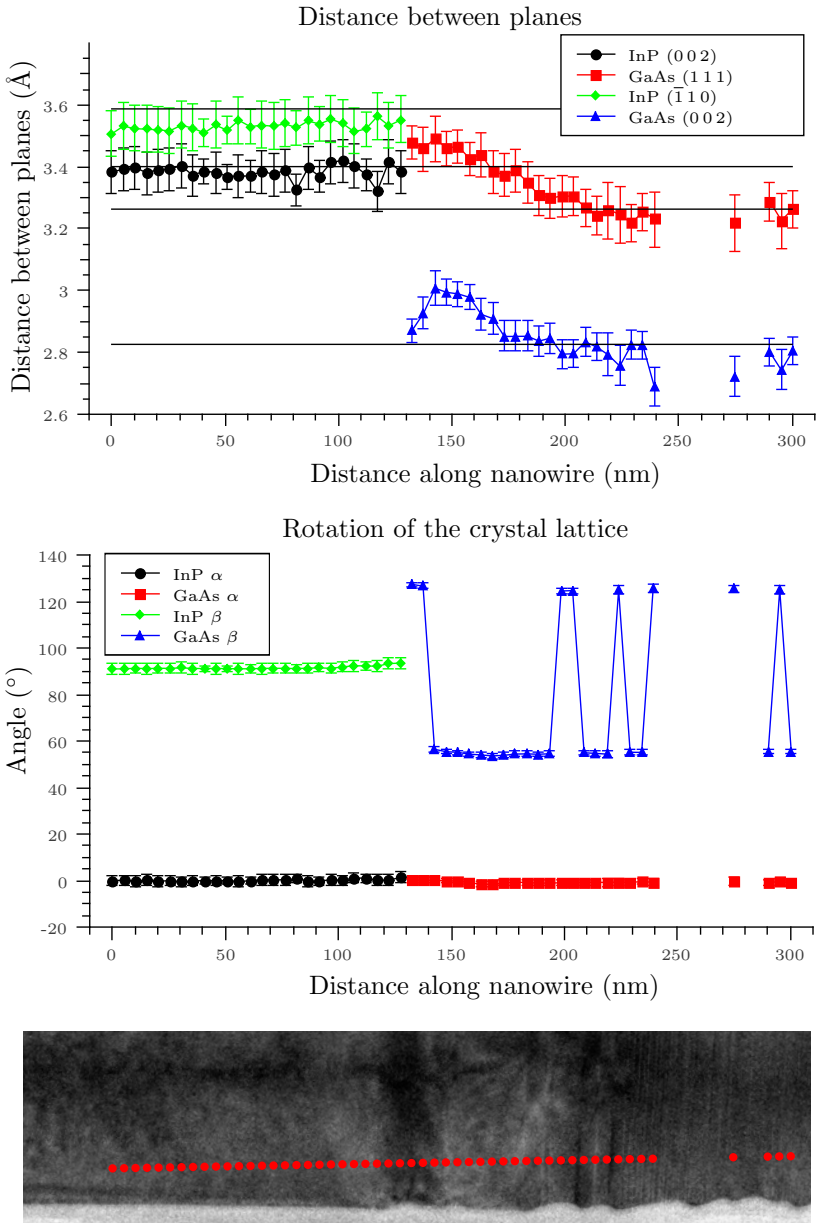

Figure 6.5: A second scan with higher density of measurement points over a shorter scan length confirms the results in figure 6.4. The length of the transition is shown here to be ca 80 nanometers. Several points of this measurement have been left out due to intense twinning making proper analysis hard. The BF TEM in the bottom is scaled to the graphs and shows the positions of the measurements.

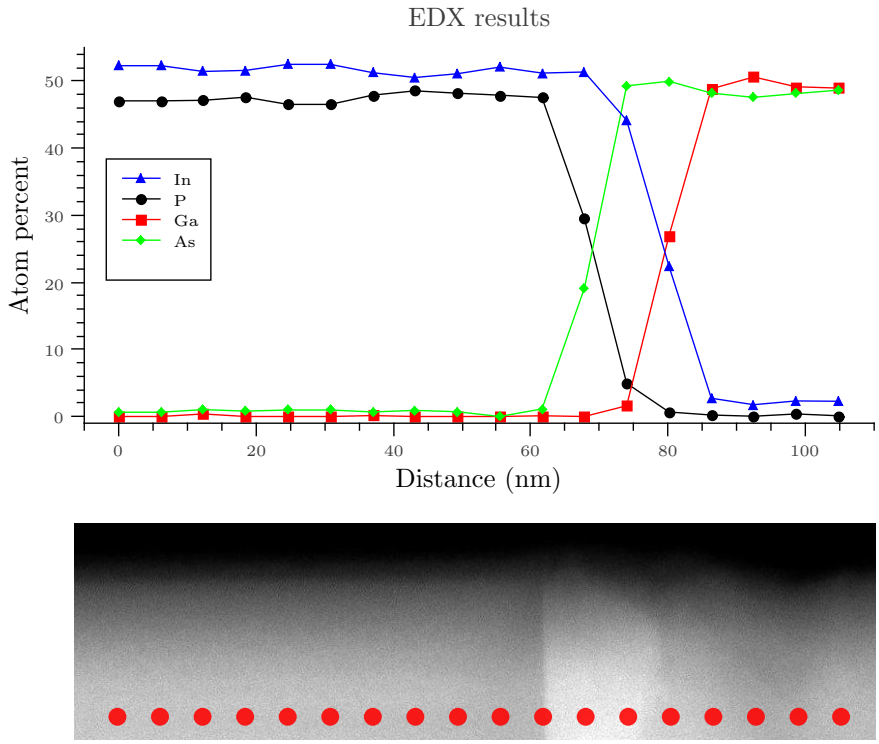

Figure 6.6: EDX over the junction of W65b, from the same production batch as W65a, shows a gradual change of composition from InP via InAsP and InGaAs to GaAs. This change occurs over 30 nm and is discernible in the ADF STEM image as a brighter area. The HAADF STEM in the bottom is scaled to the graphs.

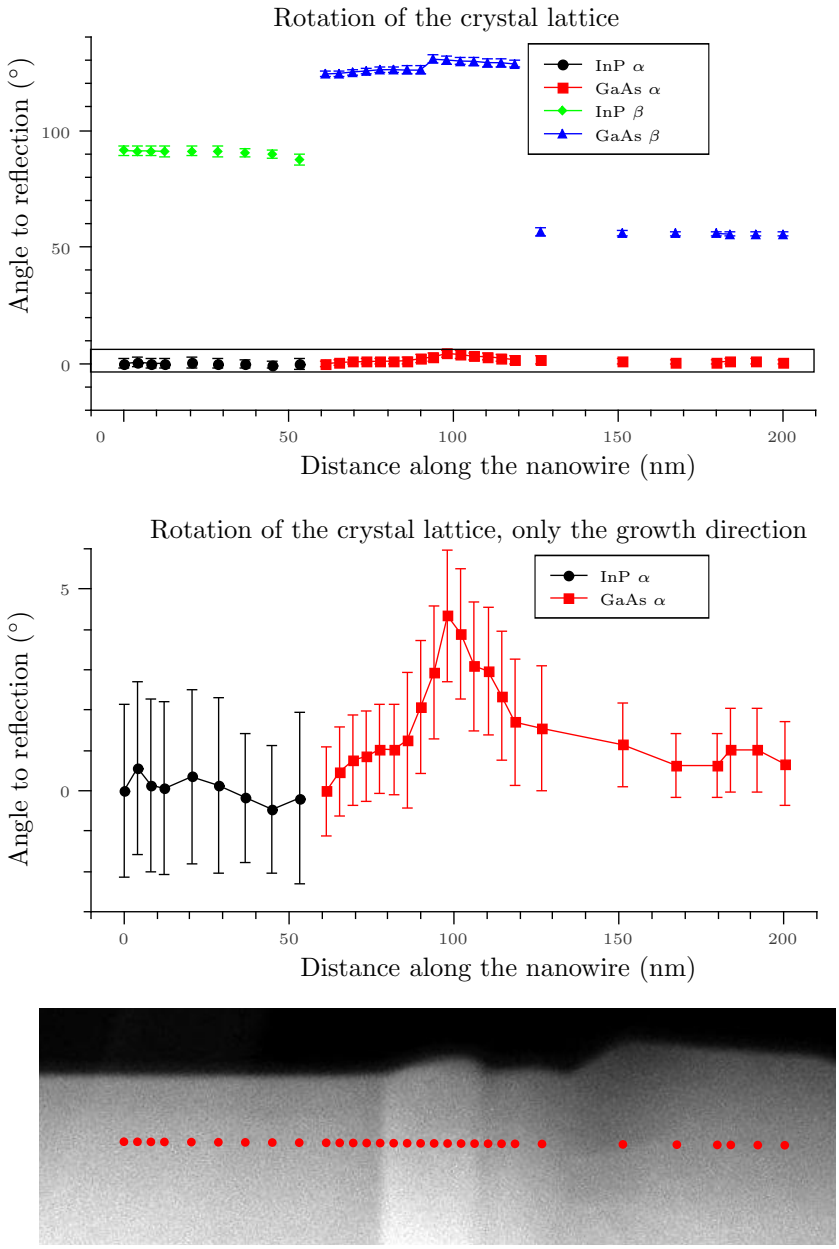

Figure 6.7: For one of the nanowires (W65c) a significant rotation of the diffraction pattern was seen. This can be interpreted as a bending of the local crystal lattice away from the center of the wire, or as a bending of the nanowire as a whole. Since the α and β angles show the same behaviour this is not an effect of a skew of the lattice. The HAADF STEM in the bottom is scaled to the graphs.

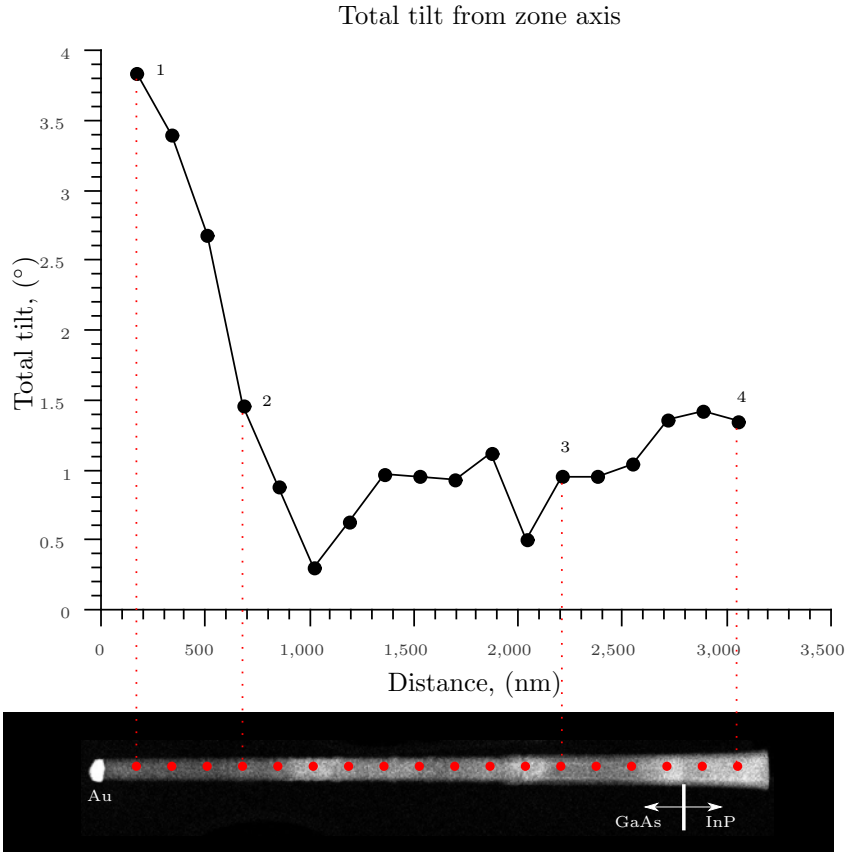

Figure 6.8: The twisting of nanowire W65d was probed with NBED in the $[1\,\bar{1}\,\bar{2}]$-direction. The resulting graph shows the total twist, i.e. the total offset of the crystal structure from a low order zone axis. The local lattice is shown to be at a maximum ca 4 degrees turned away from the $[1\,\bar{1}\,\bar{2}]$ zone axis. The HAADF STEM in the bottom is scaled to the graphs. Example diffraction patterns, from the measurements denoted with numbers 1-4 in the graph can be seen in figure 6.9. Note that this measurements was one of few done from GaAs to InP.

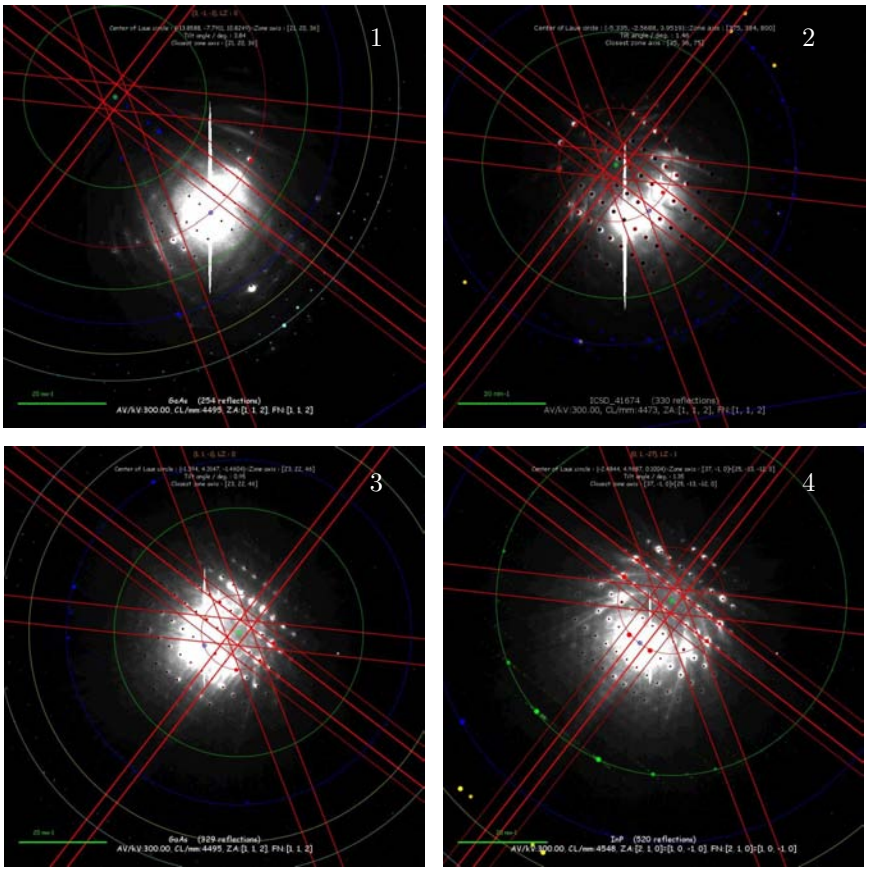

Figure 6.9: The four points marked in figure 6.8 are here presented as they were analysed. Kikuchi patterns were used in order to asses the offset of the central reflection spot of the diffraction pattern to the centre of the Laue zone circle. The distance can be translated into a tilt or twist of the crystal or the local crystal lattice structure.

as given in section 6.1. Interaction between the carbon film used as support and the nanowire might explain the twisting, however, it is not possible to rule out other reasons, such as it happening during growth.

In figure 6.9 the nature of the measurement can be seen. The patterns acquired at the four numbered points in 6.8 are here shown with overlayed simulated Kikuchi patterns. Figure 6.10 shows the tilt and twist in the two directions separately. The marked points are the same as those from figures 6.8 and 6.9. The tilt in the on-axis direction and the tilt in the radial direction do not seem to be correlated. Indeed the measurement seems to go from seeing a tilt mostly in the on-axis direction to an area with a more similar tilt in both directions.

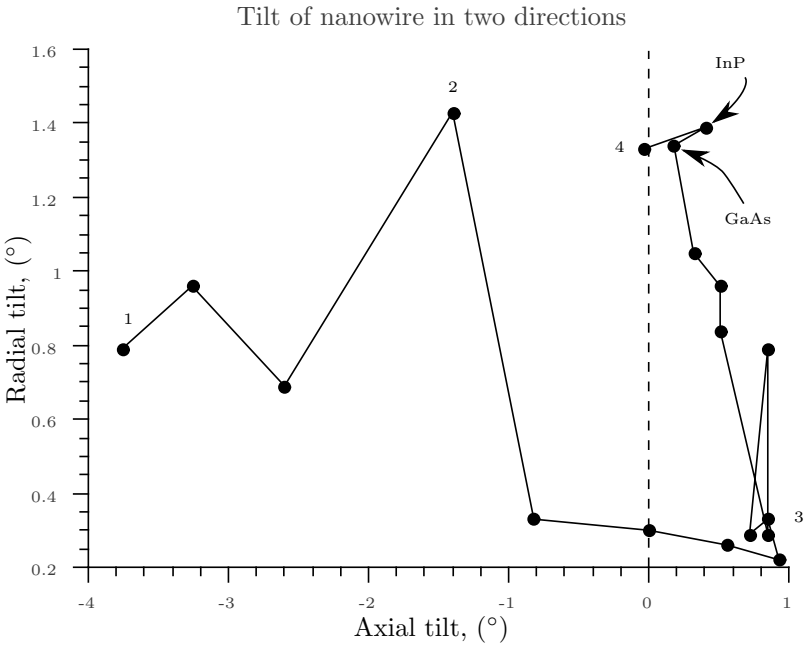

Figure 6.10: The same measurement as in figure 6.8 can also be presented showing the twisting in two directions, the radial (twisting the wire) and the on-axis (bending the wire out of the plane it is resting on). Compare with the scematic in figure 5.1(a) in chapter 5 for the different tilts. Note the difference in scale between the two axis - the maximum difference in axial tilt is much larger than the maximum difference in radial tilt. The numbered measurement points denote measurements shown in figure 6.9.

6.3 Comparison with other methods

6.3.1 CBED

Convergent beam electron diffraction (CBED) for strain analysis depends on the accurate comparison of acquired diffraction patterns to simulated ones. It is out of necessity used off-axis (since in a low order zone axis, any visible changes of the diffraction pattern due to a strained lattice would be ambiguous) and as such has a limited usability for measuring strain in certain directions. Some work have been done at finding ways of accurately comparing simulated patterns close to or in a zone axis [93] but this is neither simple nor a standard technique.

CBED normally requires a thick sample for accurate measurements. Favia et al. give the optimum specimen thickness simply as >300-400 nm [50]. If the sample is too thick however, the pattern will loose detail even when energy filtered. A convergent beam with a tiny probe is shone through the sample resulting in a diffraction pattern with large discs and much internal structure stemming from dynamic diffraction. The strain of the wire can be found from this internal structure, especially from the high order laue zone (HOLZ) lines, cf schematic in figure 6.11(a). In order to properly resolve these HOLZ lines it is necessary to do an energy filtering of the diffraction pattern. This will lead to a lower intensity in the pattern. To compensate for the lowered intensity in the pattern the exposure time has to be increased and the sample will be irradiated with a high current in a small area. This risk damaging the sample. Especially for the InP nanowires used throughout this project, electron beam induced radiation damage has been a problem.

Figure 6.11(b) show a CBED pattern from a nanowire sample used for potential strain measurement. The nanowire is too thin to give any reliable data and can be compared to CBED from the thicker substrate, figure 6.11(c). The HOLZ lines are much more pronounced. However, as can be seen in figure 6.11(d), a layer on the surface of the sample will obscure the positions of the HOLZ lines.

Even though this particular measurement failed it is still interesting to compare CBED to NBED. As pointed out by Armigliato et al. [41] the spatial resolution of CBED depends on the thickness of the sample in a simple geometric consideration. With a 200 nm thick sample the resolution would be 1×7 nm for the [3 4 0]-direction and 1×10 nm for the [2 3 0]-direction. The sensitivity of the strain measurements is 0.02%. This should be compared to NBED with a spatial resolution of ≈ 5 nm and sensitivity of 0.1% strain [49] (with a precision of 0.06% [86]). Whilst NBED is worse on paper, the straightforward analysis alone is a very good argument for using NBED. For certain samples and certain thicknesses it is also not possible to use CBED, such as in the case of the thin nanowires.

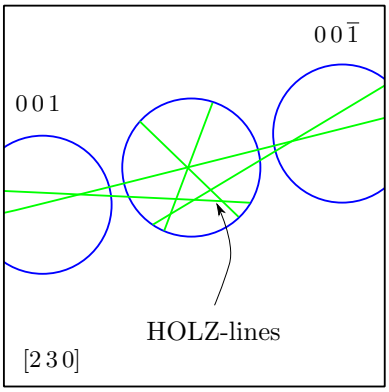

(a) CBED schematic.

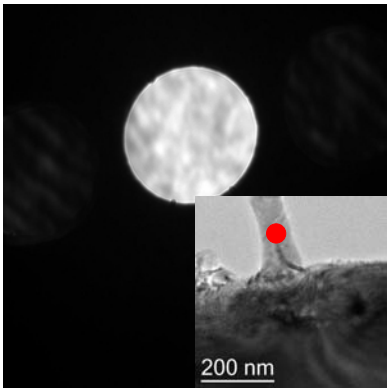

(b) CBED on a too thin nanowire embedded in polymer.

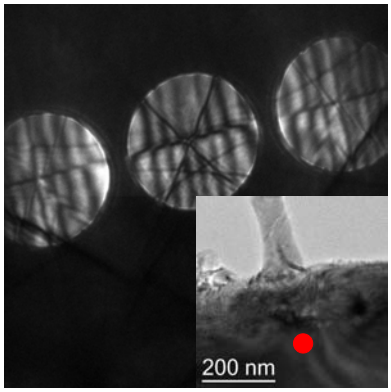

(c) CBED from a nanowire substrate.

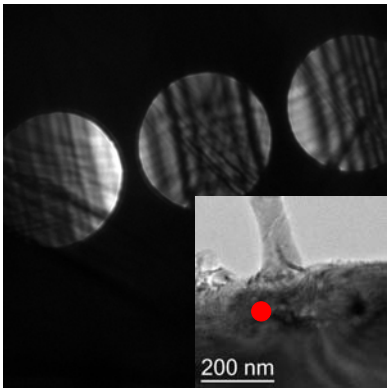

(d) CBED from substrate with a layer hindering analysis.

Figure 6.11: Strain analysis in CBED is done by comparing a simulated diffraction pattern including dynamic effects in the form of HOLZ-lines to the pattern acquired in the TEM. a) shows a simplified schematic of the expected pattern for InP [2 3 0]. The acquired pattern from different areas of the wire can be seen in b), c) and d). Neither in the wire nor in the top part of the substrate it was possible to measure the strain. The wire in b) is thin and is supported by an amorphous polymer. In d) there is a secondary layer obstructing the view of the underlaying crystal structure.

6.3.2 GPA

Geometric phase analysis (GPA) is a strain measuring method where not diffraction patterns but instead diffractograms from HRTEM micrographs are used. Figure 6.12(a) shows a schematic of the process. Diffractograms are diffraction pattern-like representations of the image data, acquired by a Fourier transform of the micrograph, projecting the frequencies found in the original image to a 2D plane. GPA is easy to use as long as you can acquire good HRTEM micrographs of a sample. The images can show no contrast reversal occurring – i.e. atoms columns are always dark and vacuum always bright or vice versa. One area of the image is chosen as the unstrained area and the diffractogram from this area will be compared to that of all other areas. The result is often presented as a colourful map of relative strain in different areas of the sample. This method can only gain information about the strain in the plane that the HRTEM image is acquired, and only in low order zone axes. Figure 6.12(b) show an example of an HRTEM GPA measurement from a thick nanowire sample.

Getting good HRTEM images is the biggest issue for the GPA method. The sample need to be of a suitable and homogeneous thickness and be accurately aligned to a low order zone axis. HRTEM-GPA of nanowires have been done by several groups, see for example [43] and [44]. These have been restricted to very thin wires. Favia et al. [50] cite the spatial resolution of HRTEM-GPA as 2-3 nm and the sensitivity of the strain measurement as 0.1%.

6.4 Conclusions and future outlook

NBED has been used successfully for local lattice analysis of nanowires. Due to this method's local nature it is possible to make the measurement with a high spatial resolution. In this chapter the local lattice distance and the rotation of the lattice were explored, as well as the measurement of a local tilt of the wire.

While there are other methods offering a higher accuracy the NBED method is more applicable for the type of samples analysed here. The measurement is also easy to perform and the analysis is almost trivial and could be automated. The thickness range that NBED is applicable for is large and compared to CBED and GPA it is more suitable for the sizes of the nanowires used in this project. A small probe results in a high flux of electrons and can lead to radiation damage in the radiated area. Since NBED exposure times can be made short it is to some extent possible to avoid this damage. A long exposure time would also increase drift of the sample during acquisition.

The nanowires examined show a number of interesting features. The size of an InP-GaAs hetero-junction, from the unstrained state of the InP to

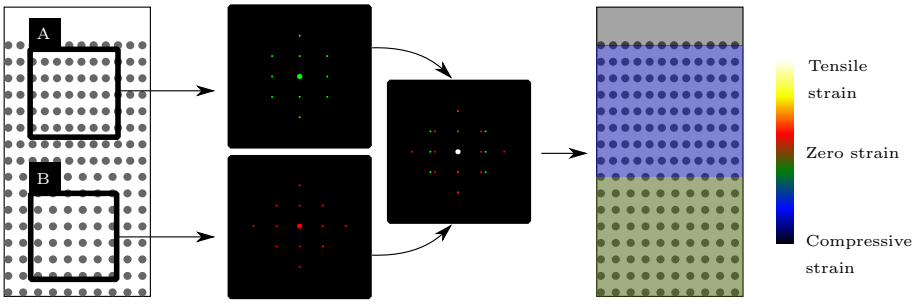

(a) GPA schematic.

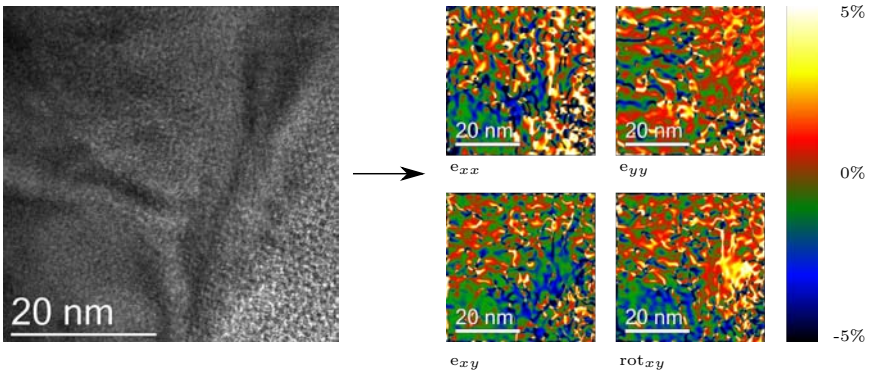

(b) GPA of a too thick nanowire

Figure 6.12: In GPA an HRTEM image is transformed into strain maps by comparing the fourier transforms of the image. In b) it was performed in the bottom of a nanowire, ca 80nm thick, with clearly visible strain contrast in the TEM image. This should yield a clear strain measurement but alas, the resulting map is noisy and not very useful. The biggest constraint is the thickness of the sample, but also the unevenness of the thickness.

the point when the GaAs lattice distance was acquired, was shown to be ca 80 nm. When comparing this to an EDX linescan of a very similar wire from the same sample, the chemical composition shows intermediate steps of InPAs and InGaAs, but this graduate change cannot explain the change in lattice parameter since the full transition from one InP to GaAs was only ca 30 nm. This shows that the naïve idea of using the lattice parameter to calculate the chemical composition is not necessarily useful.

In another wire the twist along the wire was high and a maximal difference was calculated to about 4°. Nanowires are very bendable [84, 85] and often exhibit large twists and turns which can be good to take into account, for example when a device processing step is planned.

A third wire sported an interesting local rotation of the lattice planes. The rotation was almost 4 degrees over a 20 nm stretch and then over another 20 nm the lattice planes rotated back. This skew changes the unit cell and would potentially allow many defects and release stress that build up in the junction.

All of these effects could potentially be very important for the characteristics of any device made using nanowires. Even small deviations introduced during growth or during post processing can lead to changes in band gap or transport characteristics of the wire. This is especially true near interfaces. More work should be done on making NBED into a standard method for analysing nanostructures. Automation of acquisition and analysis will help this. The software for acquisition needs to be updated to accommodate for the method. The ones used during these experiments could not access neither the EDX detector nor the ADF STEM detector at the same time as doing the NBED.

Chapter 7

Conclusions and future outlook

This thesis has been partially about nanowires as potential candidates for photovoltaics, especially for solar cells, and partially about the electron microscopy of such nanowires. Characterization is of course important when working with novel materials, both to show what is working and what is not. None of the methods used here are novel, however they have been used in novel ways or on novel materials. The process leading up to being able to use these methods is hopefully shorter for the next person who will continue this research.

After two introductory chapters, chapter 3 discussed the different sample preparation approaches involved in this work. Besides the straightforward mechanical transferring of nanowires from the specimen substrate to a sample grid suitable for TEM work, methods using the FIB and tripod polishing were also discussed. The goal of both of these approaches was to be able to look at the nanowires as they were, still connected to the substrate they were grown on.

There are many examples in the literature of when this is a necessary approach. For example it has been used for strain measurements using GPA [43], for counting layers of graphene between the substrate and the nanowires using HRTEM [94] and for making nanowires based samples ready for large rotation tomography [65].

In this work it has been used for two things. In section 4.3 a 150 nm thick layer was noticed on top of the substrate of a nanowires specimen. From EDX and HRTEM of the sample it was assumed that this layer was the result of an overgrowth of the nanowires material onto the sample. Similar overgrowth is an oft reported phenomena (cf. [75, 95]), but has to the best of my knowledge never been presented in a cross sectional HRTEM view previously.

The second thing this was used for was for direct comparison of XRD

and TEM of the very same nanowire, as in chapter 5. Several approaches were tested before finding a few that would work. During this process it was found that the InP nanowires were affected by an ion beam even a fair bit away. A mini experiment concluded that unprotected nanowires as far as 50µm away from the ion beam were bending away from the beam. This was true even for the lowest dose possible at both 15kV and 30kV beam energy. Unfortunately this was neither tested with other material nanowires nor with lower energies and alternative machine setups. The question of why this happens and how to cope with it is still an open question.

The second approach that was used was trying to do the same thing, but protecting the nanowires with a polymer layer, something that turned out to be a bad idea. The wires were again bending away from the beam, whether in this case from the ion beam directly or due to movements in the polymer (melting and re-hardening) could not be satisfyingly determined.

A third promising approach was to do in-situ lift outs of tiny loose pieces of the specimen laying on a polished Si wafer. This would minimize the time and thereby the dose of ion beam radiation needed for the process. The tiny pieces would be produced by cleaving the specimen. Though the method was tested and shown to be possible to use, unfortunately no XRD or TEM analysis was to date made with one of these samples.

The last approach to the XRD/TEM comparison was the same method used for producing the cross-section sample described above for the over-growth contamination layer. The specimen was sandwiched between silicon wafers using a thin vacuum-safe and partially conducting polymer as glue. This sandwich was then polished using tripod-polishing and finally thinned using ion milling [96]. The resulting sample is a very thin wedge of material in the center of a TEM compatible sample grid. This sample was successfully employed in the XRD/TEM analysis.

In chapter 4 three interesting features of the samples examined were uncovered. Time and resources did not allow for proper analysis of these phenomena but since the literature is very sparse on mentions of these, it was deemed important to present them. The first example was of an apparent gold protrusion in the radial center of the nanowire, leading down into the nanowire material from the gold catalyst particle. This was found in both InP-GaAs heterostructures and in GaP nanowires. Whilst not being the most common type of wire in these batches a good part of the wires would exhibit this. For the InP-GaAs wires tomography was used to figure out the actual position of the gold droplet - in the center, and not hanging on the side. EDX was used to analysed the composition of different areas around the gold, showing that the surrounding material differed from that of the nanowire.

The second example was twin-defects, stacking faults, but in a different direction than normally encountered. These twin-defects would be double twins in the diagonal along the wires, in a (-111) direction. These defects

seem to have been encountered before in the literature. It can clearly be seen in figures in [43] and in [76] it is seen in a small area and is acknowledged as a twin defect in one of the figures, but is not discussed in the text. A partial explanation might be found in [75] where the phenomenon of nonvertically grown nanowires is discussed. Here the authors pondered over how nonvertical wires can grow by epitaxial growth, and also in different well defined directions. The answer, the authors claim, is multiple twinning leading to a number of alternate possible directions for the growth. In the case with these vertical wires with twin defects, the case might be that the twin is immediately followed by another in the opposite direction leading to a straight wire, but a stacking fault in the (-111) direction.

The third example in chapter 4 was already discussed above the contamination layer on the substrate as grown.

Chapter 5 describes our efforts in designing an experiment to compare XRD and TEM of the exact same nanometer sized structure. Whilst this was only a partial success the method seems to work, which in itself is a good result. Previous efforts in comparing XRD and TEM has, to the best of my knowledge, always been on generally similar structures, never on the exact same. Examples of such are comparison of measurements on Polymer-Layered Silicate Nanocomposites using TEM and XRD [78] and of TEM and XRD of $CoPt_3$ particles [79]. The advent of new, better and more stable focusing optics for XRD makes it possible to really find and focus on a single nanometer sized structure (cf. [57]). XRD is thereby going from being a tool for ensemble measurements to being a more general tool for analysis on the nanoscale. In this process me and my colleagues believe that there are advantages to getting a confirmation of the consistency of the XRD and the TEM methods.

In Chapter 6 the NBED method for analyzing crystal structures is applied to nanowires. This might be the first time this has been done, but the technique is well researched for semiconductors in general [41,45,50,97]. The nanowires were harvested using mechanical transferring onto a lacey carbon film Cu grid. This approach has the upside that it is very quick but since thin wires are elastic [85] it might explain some of the issues seen with bending along the wires.

NBED patterns were acquired along the wires and the positions of the diffraction discs were analysed. It was shown that the NBED method not only can measure strain, but also give an estimate of the size of a transition from one material to another in a hetero junction. If this distance, as in the case with the wire analysed here, is not the same as measured with EDX, the result is a material with a much changed lattice parameter. Since a changed lattice parameter will lead to a difference in bandstructure [98,99] this might result in unexpected behaviours.

NBED was also used to give fairly precise measurements of the tilt of the nanowire, and this in both the radial and the axial direction. Combined

with cross section nanowire samples as described above, this could become a tool to analyse the quality of the growth and post-growth processing.

Finally NBED is breafly compared to the CBED and GPA methods of strain analysis. CBED requires more skill of the microscopist in tilting the wire to the correct of axis direction where the HOLZ line offset become apparent. It is also more demanding to analyse once the data is acquired. GPA is quick and easy, but requires good HRTEM images of very thin samples.

There are many things that could and should be studied further in this work. All of the three peculiarities in chapter 4 show how much there still is to figure out about the III-V nanowire growth process. Comparing XRD and TEM to each other to ensure that the measurements are comparable would in the best of worlds lead to better decisions being taken by scientists when choosing what technique to use. And NBED is a technique with much potential especially in the area of strain analysis. Anyone taking up the torch from where I leave it, will hopefully have a better set of tools for sample preparation and analysis but many stones are still left unturned. A truly non-destructive technique for preparing one wire on a substrate on top of a tomography needle would be one place to start. Optimizing the NBED process might be another. In any case I wish my successors all the best of luck.

Part III

Endmatter

Bibliography

[1] J. Kupec, R. L. Stoop, and B. Witzigmann, "Light absorption and emission in nanowire array solar cells," *Optics Express*, vol. 18, no. 26, pp. 27589–27605, 2010.

[2] B. Nöhammer, *Diffractive and refractive lenses for hard x-rays with ultra-high efficiencies*. PhD thesis, Université de Neuchâtel, Institut de Microtechnique, 2004.

[3] D. B. Williams and C. B. Carter, *Transmission Electron Microscopy: A Textbook for Materials Science*. Springer, 2nd ed., 2009.

[4] L. Freund and H. Johnson, "Influence of strain on functional characteristics of nanoelectronic devices," *Journal of the Mechanics and Physics of Solids*, vol. 49, pp. 1925–1935, 2001.

[5] D. R. Askeland, *The Science and Engineering of Materials*. Nelson Thornes Ltd, 3rd S.I. Edition ed., 1998.

[6] C. P. Kuo, S. K. Vong, R. M. Cohen, and G. B. Stringfellow, "Effect of mismatch strain on band gap in III-V semiconductors," *Journal of Applied Physics*, vol. 57, no. 12, pp. 5428–5432, 1985.

[7] J. Nelson, *The physics of solar cells*. London: Imperial College Press, 1st ed., 2004.

[8] M. A. Green, K. Emery, Y. Hishikawa, W. Warta, and E. D. Dunlop, "Solar cell efficiency tables (version 39)," *Progress in Photovoltaics: Research and Applications*, vol. 20, no. 1, pp. 12–20, 2012.

[9] S. M. Sze, *Semiconductor Devices: Physics and Technology*. Wiley, 2nd ed., 2001.

[10] L. Solymar and D. Walsh, *Electrical Properties of Materials*. Oxford University Press, USA, 8th ed., 2009.

[11] R. B. Laughlin, "Optical absorption edge of SiO_2," *Physical Review B*, vol. 22, pp. 3021–3029, 1980.

[12] J. H. Davies, *The Physics of Low-Dimensional semiconductors*. Cambridge University Press, 1998.

[13] NREL, "Reference Solar Spectral Irradiance: Air Mass 1.5." http://rredc.nrel.gov/solar/spectra/am1.5/, retreived: aug 2012.

[14] A. Brown, M. Green, and R. Corkish, "Limiting efficiency for a multi-band solar cell containing three and four bands," *Physica e-low-dimensional systems & nanostructures*, vol. 14, no. 1-2, pp. 121–125, 2002. 1st International Workshop on Nanostructures in Photovoltaics, Max Planck Inst Phys Kompleser Syst, Dresden, Germany, Jul 28-Aug 04, 2001.

[15] D. Kimberly A., "A review of nanowire growth promoted by alloys and non-alloying elements with emphasis on au-assisted III-V nanowires," *Progress in Crystal Growth and Characterization of Materials*, vol. 54, no. 34, pp. 138–173, 2008.

[16] R. S. Wagner and W. C. Ellis, "Vapor-Liquid-Solid mechanism of single crystal growth," *Applied Physics Letters*, vol. 4, no. 5, p. 89, 1964.

[17] E. Givargizov and N. Sheftal', "Morphology of silicon whiskers grown by the VLS-technique," *Journal of Crystal Growth*, vol. 9, no. 0, pp. 326 – 329, 1971.

[18] M. Yazawa, M. Koguchi, and K. Hiruma, "Heteroepitaxial ultrafine wire-like growth of InAs on GaAs substrates," *Applied Physics Letters*, vol. 58, no. 10, pp. 1080–1082, 1991.

[19] J. Appenzeller, J. Knoch, M. Björk, H. Riel, H. Schmid, and W. Riess, "Toward Nanowire Electronics," *Electron Devices, IEEE Transactions on*, vol. 55, no. 11, pp. 2827 –2845, 2008.

[20] P. J. Pauzauskie and P. Yang, "Nanowire photonics," *Materials Today*, vol. 9, no. 10, pp. 36 – 45, 2006.

[21] F. Patolsky, B. P. Timko, G. Zheng, and C. M. Lieber, "Nanowire-Based Nanoelectronic Devices in the Life Sciences," *MRS Bulletin*, vol. 32, pp. 142–149, 2007.

[22] A. R. West, *Basic solid state chemistry*. Johan Wiley & Sons Ltd., 2nd ed., 1999.

[23] H. S. Kim, Y. Myung, Y. J. Cho, D. M. Jang, C. S. Jung, J. Park, and J.-P. Ahn, "Three-Dimensional Structure of Twinned and Zigzagged One-Dimensional Nanostructures Using Electron Tomography," *Nano letters*, vol. 10, no. 5, pp. 1682–1691, 2010.

[24] D. Kriegner, E. Wintersberger, K. Kawaguchi, J. Wallentin, M. T. Borgström, and J. Stangl, "Unit cell parameters of wurtzite InP nanowires determined by X-ray diffraction," *Nanotechnology*, vol. 22, no. 42, p. 425704, 2011.

[25] M. Messing, K. Dick, L. Wallenberg, and K. Deppert, "Generation of size-selected gold nanoparticles by spark discharge – for growth of epitaxial nanowires," *Gold Bulletin*, vol. 42, no. 1, pp. 20–26, 2009.

[26] A. I. Persson, M. W. Larsson, S. Stenstrom, B. J. Ohlsson, L. Samuelson, and L. R. Wallenberg, "Solid-phase diffusion mechanism for GaAs nanowire growth," *Nature Materials*, vol. 3, no. 10, pp. 677–681, 2004.

[27] K. Sun, A. Kargar, N. Park, K. Madsen, P. Naughton, T. Bright, Y. Jing, and D. Wang, "Compound Semiconductor Nanowire Solar Cells," *Selected Topics in Quantum Electronics, IEEE Journal of*, vol. 17, no. 4, pp. 1033–1049, 2011.

[28] Y. Dong, B. Tian, T. J. Kempa, and C. M. Lieber, "Coaxial Group III-Nitride Nanowire Photovoltaics," *Nano Letters*, vol. 9, no. 5, pp. 2183–2187, 2009.

[29] J. A. Czaban, D. A. Thompson, and R. R. LaPierre, "GaAs Core-Shell Nanowires for Photovoltaic Applications," *Nano Letters*, vol. 9, no. 1, pp. 148–154, 2009.

[30] C. Colombo, M. Heibeta, M. Gratzel, and A. F. i Morral, "Gallium arsenide p-i-n radial structures for photovoltaic applications," *Applied Physics Letters*, vol. 94, no. 17, p. 173108, 2009.

[31] S. Yu, F. Roemer, and B. Witzigmann, "Analysis of surface recombination in nanowire array solar cells," *Journal of Photonics for Energy*, vol. 2, no. 1, pp. 028002–1 – 028002–9, 2012.

[32] J. Kupec and B. Witzigmann, "Dispersion, Wave Propagation and Efficiency Analysis of Nanowire Solar Cells," *Optics Express*, vol. 17, no. 12, pp. 10399–10410, 2009.

[33] P. M. Wu, N. Anttu, H. Q. Xu, L. Samuelson, and M.-E. Pistol, "Colorful InAs Nanowire Arrays: From Strong to Weak Absorption with Geometrical Tuning," *Nano Letters*, vol. 12, no. 4, pp. 1990–1995, 2012.

[34] T. Mårtensson, C. P. T. Svensson, B. A. Wacaser, M. W. Larsson, W. Seifert, K. Deppert, A. Gustafsson, L. R. Wallenberg, and L. Samuelson, "Epitaxial III-V Nanowires on Silicon," *Nano Letters*, vol. 4, no. 10, pp. 1987–1990, 2004.

[35] Z. Wu, J. B. Neaton, and J. C. Grossman, "Charge Separation via Strain in Silicon Nanowires," *Nano Letters*, vol. 9, no. 6, pp. 2418–2422, 2009.

[36] H. Goto, K. Nosaki, K. Tomioka, S. Hara, K. Hiruma, J. Motohisa, and T. Fukui, "Growth of Core–Shell InP Nanowires for Photovoltaic Application by Selective-Area Metal Organic Vapor Phase Epitaxy," *Applied Physics Express*, vol. 2, no. 3, p. 035004, 2009.

[37] P. Fuß-Kailuweit. Fraunhofer ISE CalLab. Private communication, and not yet published article, aug 2012.

[38] R. R. LaPierre, "Theoretical conversion efficiency of a two-junction III-V nanowire on Si solar cell," *Journal of Applied Physics*, vol. 110, no. 1, p. 014310, 2011.

[39] G. Armstrong and C. K. Maiti, "Strained-Si channel heterojunction p-MOSFETs," *Solid-State Electronics*, vol. 42, no. 4, pp. 487 – 498, 1998.

[40] J. Oh, K. Jeon, S.-H. Lee, J. Huang, P. Hung, I. Ok, B. Sassman, D.-H. Ko, P. Kirsch, and R. Jammy, "High mobility CMOS transistors on Si/SiGe heterostructure channels," *Microelectronic Engineering*, vol. 97, no. 0, pp. 26 – 28, 2012.

[41] A. Armigliato, R. Balboni, and S. Frabboni, "Improving spatial resolution of convergent beam electron diffraction strain mapping in silicon microstructures," *Applied Physics Letters*, vol. 86, no. 6, p. 063508, 2005.

[42] S. Krämer, J. Mayer, C. Witt, A. Weickenmeier, and M. Rühle, "Analysis of local strain in aluminium interconnects by energy filtered CBED," *Ultramicroscopy*, vol. 81, pp. 245 – 262, 2000.

[43] J. Taraci, M. Hÿtch, T. Clement, P. Peralta, M. McCartney, J. Drucker, and S. Picraux, "Strain mapping in nanowires," *Nanotechnology*, vol. 16, no. 10, pp. 2365–2371, 2005.

[44] M. Larsson, J. Wagner, M. Wallin, P. Hakansson, L. Fröberg, L. Samuelson, and L. Wallenberg, "Strain mapping in free-standing heterostructured wurtzite InAs/InP nanowires," *Nanotechnology*, vol. 18, no. 1, p. 15504, 2007.

[45] D. Cooper, A. Béché, J. M. Hartmann, V. Carron, and J.-L. Rouvière, "Strain mapping for the semiconductor industry by dark-field electron holography and nanobeam electron diffraction with nm resolution," *Semiconductor Science and Technology*, vol. 25, no. 9, p. 095012, 2010.

[46] R. Bierwolf, M. Hohenstein, F. Phillipp, O. Brandt, G. Crook, and K. Ploog, "Direct measurement of local lattice distortions in strained layer structures by HREM," *Ultramicroscopy*, vol. 49, pp. 273 – 285, 1993.

[47] K. Du and F. Phiilipp, "On the accuracy of lattice-distortion analysis directly from high-resolution transmission electron micrographs," *Journal of Microscopy*, vol. 221, pp. 63–71, 2006.

[48] K. Usuda, T. Numata, and S. Takagi, "Strain evaluation of strained-Si layers on SiGe by the nano-beam electron diffraction (NBD) method," *Materials Science in Semiconductor Processing*, vol. 8, pp. 155–159, 2005.

[49] A. Armigliato, S. Frabboni, and G. C. Gazzadi, "Electron diffraction with ten nanometer beam size for strain analysis of nanodevices," *Applied Physics Letters*, vol. 93, no. 16, p. 161906, 2008.

[50] P. Favia, M. B. Gonzales, E. Simoen, P. Verheyen, D. Klenov, and H. Bender, "Nanobeam Diffraction: Technique Evaluation and Strain Measurement on Complementary Metal Oxide Semiconductor Devices," *Journal of The Electrochemical Society*, vol. 158, no. 4, pp. H438–H446, 2011.

[51] S. O. Hruszkewycz, M. V. Holt, C. E. Murray, J. Bruley, J. Holt, A. Tripathi, O. G. Shpyrko, I. McNulty, M. J. Highland, and P. H. Fuoss, "Quantitative Nanoscale Imaging of Lattice Distortions in Epitaxial Semiconductor Heterostructures Using Nanofocused X-ray Bragg Projection Ptychography," *Nano Letters*, vol. 12, no. 10, pp. 5148–5154, 2012.

[52] M. Haider, H. Rose, S. Uhlemann, E. Schwan, B. Kabius, and K. Urban, "A spherical-aberration-corrected 200kV transmission electron microscope," *Ultramicroscopy*, vol. 75, no. 1, pp. 53–60, 1998.

[53] A. J. D'Alfonso, B. Freitag, D. Klenov, and L. J. Allen, "Atomic-resolution chemical mapping using energy-dispersive x-ray spectroscopy," *Physical Review B*, vol. 81, p. 100101, 2010.

[54] L. J. Allen, A. J. DAlfonso, B. Freitag, and D. O. Klenov, "Chemical mapping at atomic resolution using energy-dispersive x-ray spectroscopy," *MRS Bulletin*, vol. 37, pp. 47–52, 2012.

[55] P. W. Hawkes and J. C. H. Spence, eds., *Science of Microscopy*. Springer Science, 2007.

[56] J. Stangl, C. Mocuta, A. Diaz, T. H. Metzger, and G. Bauer, "X-ray diffraction as a local probe tool," *ChemPhysChem*, vol. 10, no. 17, pp. 2923–2930, 2009.

[57] G. E. Ice, B. John D, and J. W. Pang, "The race to x-ray microbeam and nanobeam science," *Science*, vol. 334, pp. 1234–1239, 2011.

[58] J. Wallentin, M. E. Messing, E. Trygg, L. Samuelson, K. Deppert, and M. T. Borgström, "Growth of doped $InAs_yP_{1-y}$ nanowires with InP shells," *Journal of Crystal Growth*, vol. 331, no. 1, pp. 8 – 14, 2011.

[59] M. Borgström, J. Wallentin, J. Trägårdh, P. Ramvall, M. Ek, L. Wallenberg, L. Samuelson, and K. Deppert, "In situ etching for total control over axial and radial nanowire growth," *Nano Research*, vol. 3, pp. 264–270, 2010.

[60] J. Wallentin, J. M. Persson, J. B. Wagner, L. Samuelson, K. Deppert, and M. T. Borgström, "High-Performance Single Nanowire Tunnel Diodes," *Nano Letters*, vol. 10, no. 3, pp. 974–979, 2010.

[61] D. Jacobsson, J. M. Persson, D. Kriegner, T. Etzelstorfer, J. Wallentin, J. B. Wagner, J. Stangl, L. Samuelson, K. Deppert, and M. T. Borgström, "Particle-assisted $Ga_xIn_{1-x}P$ nanowire growth for designed bandgap structures," *Nanotechnology*, vol. 23, no. 24, p. 245601, 2012.

[62] A. Gustafsson, L. R. Wallenberg, and J. B. Wagner, "Electron microscopy based studies of catalytically grown semiconductor nanowires," in *Beam Injection Based Nanocharacterization of Advanced Materials*, pp. 1–35, Kerala, India: Research Signpost, 1st ed., 2008.

[63] Z. Rahman, S. Shukla, H. Cho, and S. Seal, "Tutorial: In-Situ Site-Selective FIB for High Resolution TEM Sample Preparation," *Microscopy and Analysis*, vol. 113, pp. 8–12, 2006.

[64] Aremco Products Inc., "Technical Bulletin A9, Washaway Mounting Adhesives and Accessories," tech. rep., apr 2012.

[65] P. D. Cherns, F. Lorut, C. Dupr, K. Tachi, D. Cooper, A. Chabli, and T. Ernst, "Electron tomography of gate-all-around nanowire transistors," *Journal of Physics: Conference Series*, vol. 209, no. 1, p. 012046, 2010.

[66] L. A. Giannuzzi and F. A. Stevie, eds., *Introduction to Focused Ion Beams – Instrumentation, Theory, Techniques and Practice*. Springer US, 2005.

[67] J. McCaffrey and J. Hulse, "Transmitted color and interference fringes for TEM sample preparation of silicon," *Micron*, vol. 29, no. 23, pp. 139–144, 1998.

[68] B. A. Wacaser, K. A. Dick, J. Johansson, M. T. Borgström, K. Deppert, and L. Samuelson, "Preferential Interface Nucleation: An Expansion of the VLS Growth Mechanism for Nanowires," *Advanced Materials*, vol. 21, no. 2, pp. 153–165, 2009.

[69] J. Wallentin, M. Ek, L. R. Wallenberg, L. Samuelson, K. Deppert, and M. T. Borgström, "Changes in Contact Angle of Seed Particle Correlated with Increased Zincblende Formation in Doped InP Nanowires," *Nano Letters*, vol. 10, no. 12, pp. 4807–4812, 2010.

[70] P. A. Lin, D. Liang, S. Reeves, X. P. Gao, and R. M. Sankaran, "Shape-Controlled Au Particles for InAs Nanowire Growth," *Nano Letters*, vol. 12, no. 1, pp. 315–320, 2012.

[71] J. M. Persson, "Nanowire gold droplet tomography movie clip." http://www.microscopy.cen.dtu.dk/~johmp/thesis/tomo.mpg, jul 2012.

[72] H. J. Joyce, J. Wong-Leung, Q. Gao, H. H. Tan, and C. Jagadish, "Phase Perfection in Zinc Blende and Wurtzite III-V Nanowires Using Basic Growth Parameters," *Nano Letters*, vol. 10, no. 3, pp. 908–915, 2010.

[73] R. E. Algra, M. A. Verheijen, L.-F. Feiner, G. G. W. Immink, W. J. P. v. Enckevort, E. Vlieg, and E. P. A. M. Bakkers, "The Role of Surface Energies and Chemical Potential during Nanowire Growth," *Nano Letters*, vol. 11, no. 3, pp. 1259–1264, 2011.

[74] J. Johansson, L. S. Karlsson, C. P. T. Svensson, T. Mårtensson, B. A. Wacaser, K. Deppert, L. Samuelson, and W. Seifert, "Structural properties of ⟨1 1 1⟩B oriented III-V nanowires," *Nature Materials*, vol. 5, no. 7, pp. 574–580, 2006.

[75] E. Uccelli, J. Arbiol, C. Magen, P. Krogstrup, E. Russo-Averchi, M. Heiss, G. Mugny, F. Morier-Genoud, J. Nygård, J. R. Morante, and A. Fontcuberta i Morral, "Three-Dimensional Multiple-Order Twinning of Self-Catalyzed GaAs Nanowires on Si Substrates," *Nano Letters*, vol. 11, no. 9, pp. 3827–3832, 2011.

[76] S. A. Dayeh, W. Tang, F. Boioli, K. L. Kavanagh, H. Zheng, J. Wang, N. H. Mack, G. Swadener, J. Y. Huang, L. Miglio, K.-N. Tu, and S. T. Picraux, "Direct Measurement of Coherency Limits for Strain Relaxation in Heteroepitaxial Core/Shell Nanowires," *Nano Letters (Article ASAP)*, On Web: Oct 3rd 2012.

[77] J. P. Boulanger and R. R. LaPierre, "Patterned gold-assisted growth of GaP nanowires on Si," *Semiconductor Science and Technology*, vol. 27, pp. 035002–035007, 2012.

[78] A. B. Morgan and J. W. Gilman, "Characterization of polymer-layered silicate (clay) nanocomposites by transmission electron microscopy and x-ray diffraction: A comparative study," *Journal of Applied Polymer Science*, vol. 87, no. 8, pp. 1329–1338, 2003.

[79] H. Borchert, E. V. Shevchenko, A. Robert, I. Mekis, A. Kornowski, G. Grübel, and H. Weller, "Determination of Nanocrystal Sizes: A Comparison of TEM, SAXS, and XRD Studies of Highly Monodisperse $CoPt_3$ Particles," *Langmuir*, vol. 21, no. 5, pp. 1931–1936, 2005.

[80] Institute of Semiconductor and Solid State Physics, Johannes Kepler Universität, Linz. http://www.hlphys.jku.at/.

[81] ID01 ESRF. http://www.esrf.eu/UsersAndScience/Experiments/-StructMaterials/ID01/.

[82] ESRF/ISDD, "MAXIPIX technical data." http://www.esrf.eu/-Instrumentation/DetectorsAndElectronics/maxipix/techdata, aug 2011.

[83] Stadelmann, P. JEMS, Java Electron Microscopy Software, ver 3.6322U2011. CIME-EPFL:Laussane, Switzerland.

[84] M. Lexholm, I. Karlsson, F. Boxberg, and D. Hessman, "Optical determination of Young's modulus of InAs nanowires," *Applied Physics Letters*, vol. 95, no. 11, p. 113103, 2009.

[85] H. Liang, M. Upmanyu, and H. Huang, "Size-dependent elasticity of nanowires: Nonlinear effects," *Physical Review B*, vol. 71, p. 241403, 2005.

[86] A. Béché, J. L. Rouvière, L. Clement, and J. M. Hartmann, "Improved precision in strain measurement using nanobeam electron diffraction," *Applied Physics Letters*, vol. 95, no. 12, p. 123114, 2009.

[87] Gatan Inc. Pleasanton, California. DigitalMicrograph™, ver. 1.85.1535.

[88] A. W. Stevenson, "Thermal vibrations and bonding in GaAs: an extended-face crystal study," *Acta Crystallographica Section A*, vol. 50, no. 5, pp. 621–632, 1994.

[89] K. A. Dick, J. Bolinsson, B. M. Borg, and J. Johansson, "Controlling the Abruptness of Axial Heterojunctions in III-V Nanowires: Beyond the Reservoir Effect," *Nano Letters*, vol. 12, no. 6, pp. 3200–3206, 2012.

[90] M. A. Verheijen, G. Immink, T. de Smet, M. T. Borgström, and E. P. A. M. Bakkers, "Growth Kinetics of Heterostructured GaP-GaAs Nanowires," *Journal of the American Chemical Society*, vol. 128, no. 4, pp. 1353–1359, 2006.

[91] M. Takeguchi, M. McCartney, and D. Smith, "Mapping In concentration, strain, and internal electric field in InGaN/GaN quantum well structure," *Applied Physics Letters*, vol. 84, no. 12, pp. 2103–2105, 2004.

[92] D. Gerthsen, E. Hahn, B. Neubauer, A. Rosenauer, O. Schön, M. Heuken, and A. Rizzi, "Composition Fluctuations in InGaN Analyzed by Transmission Electron Microscopy," *physica status solidi (a)*, vol. 177, no. 1, pp. 145–155, 2000.

[93] J. M. Zuo, "Quantitative Convergent Beam Electron Diffraction," in *Electron Crystallography - Novel Approaches for Structure Determination of Nanosized Materials* (T. E. Weirich, J. L. Lábár, and X. Zou, eds.), vol. 211 of *NATO Science Series*, proceedings B.6, pp. 143–168, Springer, 2004.

[94] A. M. Munshi, D. L. Dheeraj, V. T. Fauske, D.-C. Kim, A. T. J. van Helvoort, B.-O. Fimland, and H. Weman, "Vertically Aligned GaAs Nanowires on Graphite and Few-Layer Graphene: Generic Model and Epitaxial Growth," *Nano Letters*, vol. 12, no. 9, pp. 4570–4576, 2012.

[95] M. Heiss, B. Ketterer, E. Uccelli, J. R. Morante, J. Arbiol, and A. F. i Morral, "In(Ga)As quantum dot formation on group-III assisted catalyst-free InGaAs nanowires ," *Nanotechnology*, vol. 22, no. 19, p. 195601, 2011.

[96] J. Ayache, L. Beaunier, J. Boumendil, G. Ehret, and D. Laub, *Sample Preparation Handbook for Transmission Electron Microscopy*. Springer New York, 2010.

[97] A. Béché, C. Bougerol, D. Cooper, B. Daudin, and J. L. Rouvière, "Measuring two dimensional strain state of AlN quantum dots in GaN nanowires by nanobeam electron diffraction," *Journal of Physics: Conference Series*, vol. 326, no. 1, p. 012047, 2011.

[98] M. Cardona, N. E. Christensen, and G. Fasol, "Relativistic band structure and spin-orbit splitting of zinc-blende-type semiconductors," *Physical Review B*, vol. 38, pp. 1806–1827, 1988.

[99] L. D. Bell and W. J. Kaiser, "Observation of Interface Band Structure by Ballistic-Electron-Emission Microscopy," *Physical Review Letters*, vol. 61, pp. 2368–2371, 1988.